MEAN SEA SURFACE MODELLING FROM MULTI–SATELLITE ALTIMETRY UTILISING FREQUENCY DOMAIN TECHNIQUES

ROBERT ANTHONY CULLEN

Doctor of Philosophy

THE UNIVERSITY OF ASTON IN BIRMINGHAM

March 1998

THE UNIVERSITY OF ASTON IN BIRMINGHAM

MEAN SEA SURFACE MODELLING FROM MULTI-SATELLITE ALTIMETRY UTILISING FREQUENCY DOMAIN TECHNIQUES

ROBERT ANTHONY CULLEN

Doctor of Philosophy

Summary

A technique is presented for the development of a high precision and resolution Mean Sea Surface (MSS) model. The model utilises Radar altimetric sea surface heights extracted from the geodetic phase of the ESA ERS-1 mission. The methodology uses a modified *Le Traon* et al. (1995) cubic–spline fit of dual ERS-1 and TOPEX/Poseidon crossovers for the minimisation of radial orbit error. The procedure then uses Fourier domain processing techniques for spectral optimal interpolation of the mean sea surface in order to reduce residual errors within the model.

Additionally, a multi–satellite mean sea surface integration technique is investigated to supplement the first model with additional enhanced data from the GEOSAT geodetic mission.

The methodology employs a novel technique that combines the *Stokes'* and *Vening–Meinsz'* transformations, again in the spectral domain. This allows the presentation of a new enhanced GEOSAT gravity anomaly field.

Key phrases:

- Fast Fourier Transform,
- Marine Geodesy,
- Mean Sea Surface,
- Radar Altimetry.

ACKNOWLEDGEMENTS

I am indebted to Phil Moore for supervision throughout the period of research and subsequent compilation of this thesis. I am also very grateful to the Natural Environment Research Council (NERC) for the financial assistance required to undertake the work.

I would like to thank a number of colleagues who provided both interest and, of course, much needed criticism namely; Ruaraidh Mackenzie, Chris Murphy, Stuart Carnochan, Henno Boomkamp, Matthew Reynolds and Russell Walmsley.

Additionally I thank my parents for their continued support, Juliet Gray for thesis therapy and Victoria Scholes for removing pollutants from my mean sea surface.

Finally, I would like to convey my utmost appreciation to Philippa for her endurance during this period. It is to her that I dedicate this work.

Contents

List of Figures

List of Tables

Chapter 1

Introduction

The continuous global observation of oceans has become increasingly important not only as part of simple forecasting but in order to develop better working knowledge of complex scenarios, such as the El Niño phenomena and the little understood ocean–atmosphere coupling system, for input into climate modelling/observation programmes. Additionally, continuous global ocean measurements are required if improvements in gravity field modelling are to be achieved.

Progress in these Earth sciences would not have been made by now if it was not for a conference held in 1970 at Williamstown in the USA (described in *Kaula*, 1970). Here the proposal for the testing of a prototype Spaceborne Radar Altimeter (SRA[1]) on–board the SKYLAB platform was approved. This initiative taken by NASA proved successful and instigated the beginning of a programme of altimeter missions. After 25 years of on–going analysis and re–analysis of acquired data we are still making vast improvements in our understanding of global Earth sciences, in particular ocean circulation and gravity field recovery, in addition to the various data product derivatives required by industry, scientists and the public.

The radar altimeter (RA) itself took rather a long time to come to fruition. Following the conception of radar in the early part of the 20th Century the possibility of measuring an aircraft's altitude via the timing of radar pulses incident vertically to the underlying surface, was made following the Second World war. It was not until 1957 when *Moore* and *Williams* described analytically the structure of return radar waveforms over terrain and considered the various design parameters that the instrument received greater interest. Airborne testing took place over semi–flat ocean surfaces which allowed more reliable results and specular reflections could be modelled more easily.

[1]A list of acronyms is provided in Appendix A.

In fact it could be said that the instrument's availability during the 1960s was timely. By the mid 1960s the studies of gravity field and global ocean circulation modelling were facing uncertain futures, since gravimetry and global sea–surface height data could only be collected either from instruments placed on–board ships, which proved expensive, or from moored instruments that had little use on their own. The difficulty facing those requiring sea surface information can be summed up with a direct quote from *Heiskanen* and *Moritz* (*Heiskanen* and *Moritz*, 1967, pp. 254) stating:

> As a matter of fact, we can only estimate the covariance function [of the gravity field] from samples distributed over the whole Earth. But even this is not quite possible at present, because of the imperfect or completely missing gravity data over the oceans.

As an example of this Figure 1.1 shows what 20 years of shipboard gravimetry measurements have produced and it can be seen that vast regions of the south Pacific, Atlantic and Indian oceans are devoid of data. In comparison, in just 10 days of spaceborne altimetry (see Fig. 1.2), an almost complete global coverage of the Earths oceans can be achieved, which if repeated can allow long term spatial and temporal sampling for ocean circulation studies. Alternatively, if the satellite is allowed to drift, or placed into an orbit with a long repeat period for a sufficient amount of time, a high spatial resolution data set of sea-surface heights can be used for valuable input into geodetic studies. It was essentially on these criteria that the radar altimeter received the go–ahead for testing in an Earth orbit. Naturally it could be argued that if SRA missions had never been given an opportunity then more emphasis may have been placed on collecting data from the southern oceans. However the spatial and temporal sampling required would still remain unfeasible given the cost of such operations.

Data gathered from the three missions of the 1970s (SKYLAB, GEOS-3 and SEASAT) can now largely be discounted, although follow–up analysis of their data reinforced the need for altimeters and also provide a host of new applications (*McGoogan*, 1975, for example). In 1985 we saw the launch of the U.S. Navy's GEOSAT mission, primarily placed in a drifting orbit for almost 18 months in order to generate a high resolution gravity field for use by submarine navigational instruments. This classified data began a programme of de–classification in 1991 following the end of the cold–war. Geodesists, amongst others, argued that these data would have better use in the public domain than in limited military usage. The secondary task of GEOSAT was its Exact Repeat Mission (ERM) with the placing of

Figure 1.1: Shipboard gravimetry measurement locations from the GEODAS(v.3.3) database available from the U.S. National Geophysical Data Center. Here data has been collected between 1953 and the end of 1996.

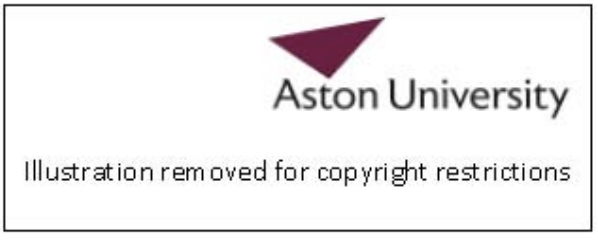

Figure 1.2: Ground–track for a single TOPEX/Poseidon 10 day cycle (66) containing 479188 observations. Graphs are generated using Generic Mapping Tools (GMT), see *Wessel* and *Smith* (1991) and *Wessel* and *Smith* (1996).

the platform into a 17 day repeat orbit. This allowed public domain access of continuously sampled global ocean data for 3 years before its failure in 1990 (*Cheney* et al., 1991). However, GEOSAT data was limited due to poor orbit determination, altimeter mispointing due to its gravity–gradient stabilisation and the lack of on–board microwave radiometer which led to insufficient ability to account for atmospheric effect on radar. Also, data degradation as a result of the approach of solar maximum at the end of the 1980s affected both the modelling of ionospheric slowing of pulses and solar drag. This resulted in even poorer orbit determination. It was not until the launch of the European Space Agencies (ESA) first Earth Resources Satellite (ERS-1) in July 1991 that useful data has become available for continuous ($\sim$4 year mission) observations of the sea, land and ice–surfaces over a range of orbit designs that have catered for the relevant science. Even the failure of one of the tracking mechanisms (described briefly in chapter 4) at the very beginning of the mission has proved to be of little or no consequence since the U.S./French TOPEX/Poseidon (referred to as T/P) satellite was launched in August 1992. This mission, which contains two altimeters (the U.S. NRA and French SSALT), has superior tracking and ionospheric correction capability. T/P was placed into an orbit that satisfies the observation of major tidal constituents, but which is of little use to the geodesist, although it may be used to enhance the orbit of ERS-1 which, as we shall see, has great use.

To date the radar altimeter has proved invaluable and its future is guaranteed for ocean circulation and digital elevation model (DEM) refinement. Geodesists, however, now require a dedicated gravity mission for their purposes whilst for the study of the ice surfaces will see the use of a spaceborne laser altimeter planned for the first decade of the next century.

Evidence of climate change has accumulated since the industrial revolution began, and now there have been innumerable hypotheses regarding our future climate. Scenarios have been conceived showing sea–level rise as a result of stronger radiative forcings. These are due to the accumulation of anthropogenic greenhouse gases within the troposphere, increased photochemical ozone destruction within the stratosphere which results from higher releases of chlorofluorocarbons. Ultimately, such conjectures are impossible to validate without complete observation of, amongst other aspects of the system, the final output — that is global sea surface temperatures and heights. Scientific working groups have fuelled media attention, provoking public opinion. This in turn has led governments, and other international organisations, to pay attention to the treatment of the Earth by setting up a number of scientific bodies such as the International Panel on

Climate Change (IPCC). Programmes have been promoted, such as World Climate Research Program (WCRP), Earth Observing System—Mission to Planet Earth (EOS—MTPE), World Ocean Circulation Experiment (WOCE) and Tropical Ocean and Global Ocean program (TOGA.) It is with the data requirements of such programmes that several missions have been planned for the immediate future; commencing with the GEOSAT follow–on[2] and the ESA ENVISAT–1 mission in 1999 and a TOPEX follow–on (JASON-1) in 2000.

Of interest to oceanographers and geodesists for almost diametrically opposite reasons is the globally mapped precise Mean Sea Surface (MSS). For the oceanographer, and as valuable input for the above mentioned programmes, the MSS is a surface from which variability and dynamic topography may be monitored. In order for this to take place the geoid (the surface of equi–potential gravity closely approximating to the MSS to within a couple of meters) must be removed. Here, errors within geoidal modelling are considered a form of noise within the required data products. Nevertheless, the MSS does provide a quick method of assessing variability although more complex methods may be used (see chapter 6).

Ironically, the geodesist requires, for example, the determination of the high resolution and precision geoid for the observation and reconstruction of *paleo*–tectonic history. Any ocean signatures in the measureable marine geoid are required to be filtered out as here they are considered unwelcome. With this understood, the marine geoid (with our requirements in mind) can currently only be determined from satellite altimetry, hence the inclusion of oceanic signals. It can be seen why geodesists insist on a gravity mission such as ESA's ARISTOTLES that was unfortunately shelved (*Mattok*, 1991), or a long term (> 10 years) altimetry geodetic mission.

As we shall see in the next chapter there are currently a number of philosophies used for MSS generation. However they all follow a set of general rules, namely:

1. Data from long period geodetic phases are required so a high spatial resolution can be obtained, for example, GEOSAT and ERS-1 Geodetic Phases.

2. Repeat mission data is required to allow the *stacking* of profiles to minimise the effect of variability.

3. The inclusion of the more accurate T/P data if the use of the MSS is predominantly for use with T/P data.

[2]The GEOSAT Follow–on platform was launched in February 1998.

4. A suitable method of interpolating to the grid.

5. A suitable method of integrating data sets from different satellites.

The methods of MSS generation proposed within this thesis address the above rules through the adoption of Fourier domain optimal processing techniques. These techniques, whilst having a background in gravity field processing, have had little or no use in MSS determination (although an attempt was made by *Jolly* (1995)). Such methods have been shown to speed up the process of traditional optimal interpolation.

In brief, raw altimetry from the ERS-1 geodetic phase is corrected for a range of errors such as radial orbit, tides, environmental and surface effects, as described in chapter 4. Data is then gridded, fast Fourier transformed (FFT) and optimally interpolated within the spectral domain before inverse fast Fourier transforming (IFFT) to the spatial domain. This is described in detail in chapters 5 and 6.

This method solves the problem of lengthy matrix inversion, conventionally used only over portions of the earth, via the simple multiplication at each frequency of our original surface with a correcting factor over the entire globe.

In addition this thesis explores the possibility of integrating two separate MSS models from the ERS-1 MSS and GEOSAT with poorly determined orbits. This method is approached in two chapters (7 and 8). In the first of these the global gravity anomaly field is developed using the *McAdoo* and *Marks* (1992) method. This involves removing orbit error via taking along–track slopes, generation of deflection of the vertical and transformation to the gravity anomaly in the spectral domain. This is presented in a separate chapter as essentially it uses the newly released enhanced GEOSAT data sets (*Cheney*, 1997b) and thus is a new version of a gravity anomaly map.

Secondly chapter 8 describes the option to incorporate shipboard/terrestrial gravity data with the global gravity anomaly at a later date. The gridded field is spectrally transformed and formed into a MSS with removal of orbit error. The two mean sea surfaces are then amalgamated to produce a joint solution.

In essence this study aims to thoroughly describe oceanographical/geodetic theory, the instrument from which we derive our data product and how errors aliased into sea–heights may be removed effectively. It ends with a critical view on the methods developed within this thesis and the others available. The case is argued for future MSS generation with attention paid to the increasing amount of data available, despite the numerous limitations arising with that data.

Chapter 2

The Structure of the Mean Sea Surface

2.1 Introduction

In order to fully appreciate the modelling of the mean sea surface from radar altimetry, it is necessary to define a number of parameters linked to its determination. This is approached here in two ways, reflecting their separate scientific interests. In the first case the structure of the Earth is explained. Here, by modelling its structure we can infer aspects of its gravity field and vice–versa with its inverse problem.

Secondly, the main features of the oceans are described allowing a more explicit definition of the MSS to be given than that put forward in chapter 1. After a short discussion on the data available, a description of existing MSS models is given and an outline of the methods of contributive research carried out within the rest of this thesis.

2.2 The Earth's Gravity Field

The overall inner structure of the Earth is almost entirely provided from seismic information with additional data from magnetic and gravity studies, core drilling and analysis of material in the vicinity of volcanos used to derive mainly surface properties.

The structure can be narrowed down to roughly 4 regions; 1. The crust, a silica rich layer of surface rock ~35 km thick beneath the continents and ~7 km thick for the oceans; 2. The mantle from which the crust is essentially formed (see *Fowler*,

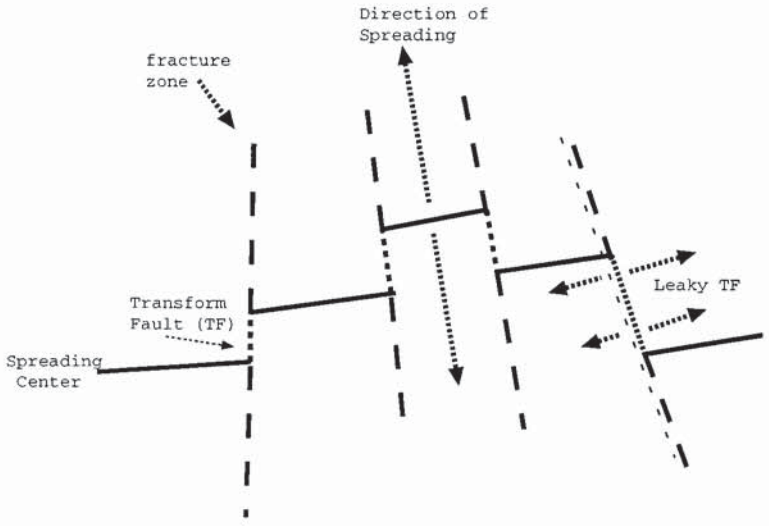

Figure 2.1: Schematic example of Plate tectonics.

1990) and the 3. inner and 4. outer core. It is also important to specify a number of other relevant terms namely;

1. Lithosphere, the mechanically strong outer layer roughly 100 km in thickness containing the crust and outermost mantle.

2. The Asthenosphere whose higher temperature and lower viscosity allow the lithospheric to essentially *float* on top over geological time scales as evidenced by hot–spot swells formed by mantle plumes. Hot spot trails may be seen by examining the many volcanic island ridges in the central pacific (i.e., the Hawaiian Ridge or Emperor Island Chain) and provides a method of determining the relative motion of the lithosphere.

3. Another term is the Mohorovičić (or *Moho*) discontinuity depth at which the crust meets the mantle. Estimating this depth is possible via the use of gravity field information along with flexure models (see *Levitt* and *Sandwell*, 1995, for example).

2.2.1 Plate Tectonics

The concept that the Earth's Lithosphere consists of a number of separate rigid plates was first considered and accepted in the 1960/70s, although some still find the theory too simplistic. However it is currently the best description of the lithospheric characteristics and essentially 5 assumptions exist regarding the tectonic structure (*Fowler*, 1990). These are:

1. New lithospheric material is produced along accreting mid–ocean ridges (spreading centers) hence plates appear to move apart. There are fast (100 – 160 mm/yr) and slow (15 – 30 mm/yr) spreading ridges such as the Pacific–Nazca and Africa–South America mid–ocean ridges respectively.

2. This new oceanic lithospheric forms part of a plate that may contain continental lithosphere.

3. Sea–floor spreading at mid–ocean ridges results in the destruction of plates at ocean trenches where material is forced into the Mantle and melted, these regions are more commonly known as subduction zones and are characterised by gravity minimums and the existence of volcanic activity just beyond the zones.

4. Regions exist at boundaries where plates move past each other and tectonic material is neither created nor destroyed. At spreading centers sudden offsets occur (see Fig. 2.1) known as *transform faults*. Active *transform faults* give an indication of the current direction of spreading. Beyond these lie inactive regions known as *fracture zones* that trace out past plate spreading. *Leaky Transform faults* occur at faults where a small element of divergence exists. An example of this phenomena occurs Africa–Eurasian plate boundary near the Azores.

5. Continental lithosphere is neither created nor destroyed at convergent or divergent boundaries. Before this assumption was incorporated the theory was effectively undermined since subduction regions exist, such as the Himalayas, where land mass is not being lost.

The existence and ability to age tectonic plates was originally achieved via the measurement of the magnetic polarity of rocks about spreading centers. Unfortunately surveys are limited to small accessible areas. However, with ship/airborne magnetic surveys and the advent of high density altimetry, visual observation of sea–floor topography in great detail has been achieved. Recent studies, such as *Cazenave* et al. (1995), have examined the wavelengths of geodetic features resulting in some attempt at aging the ocean floor by independent means.

There are several major tectonic plates as shown in Fig. 2.2 that we will identify in great detail from gravity and sea surface information in chapters 6, 7 and 8.

The reason why we are able to identify such short wavelength features (i.e., their width) can by described by the concept that the large scale gravity signal is generated by the combined mass of the core and mantle with characteristics arising due

Figure 2.2: Plate tectonic boundaries of the Earth.

to large time scale density and thermal changes. Sea floor topography consisting of less mass and shorter wavelength features result in gravity signals which, due to upward gravity continuation through the ocean, emanate as fluctuations in sea surface height. Thus if a precise global knowledge of the gravity field exists at all scales, it will allow most tectonic features to be resolved.

2.2.2 The Gravity Field

Let the Earth's centre of mass be the origin of an x, y, z right handed axis coordinate system with the x–axis in the plane of the Greenwich Meridian, z–axis being the axis of rotation and y–axis normal to the xz plane. The gravitational potential $V(x, y, z)$ associated with the Earth at a point on or outside its surface, P, follows Newton's gravitational law (see *Heiskanen* and *Moritz*, 1967) such that

$$V(P) = G\iiint_{Earth} \frac{\rho(Q)}{l} dV_Q \tag{2.1}$$

where, G is the gravitational constant (6.672×10^{-11} $\mathrm{m^3 s^{-2} kg^{-1}}$), $\rho(Q)$, the internal mass density at a unit volume element, dV_Q of centre Q and l is the distance between the two locations, P and Q. The gravity potential, W may now be defined as the addition of gravitational potential, V and rotational potential V_R of the Earth with

angular rotation, ω, such that

$$W(x,y,z) = V(x,y,z) + V_R(x,y,z) = V(x,y,z) + \frac{1}{2}\omega^2(x^2+y^2). \tag{2.2}$$

The gravity potential, or geopotential, may also be expressed (see Fig. 2.3) by the normal potential, $U(x,y,z)$ of a rotating ellipsoid and a disturbing or anomalous potential, $T(x,y,z)$ so that at a point, p

$$W_p = U_p + T_p \tag{2.3}$$

The surfaces of constant W are known as equi–potential surfaces. The equi–potential surface that best approximates the mean sea surface is known as the *geoid* and its height above the reference ellipsoid is known as the *geoidal height.* As an example the equi–potential value for the 1991 geoid is $W = W_0 = 62636856.5 \pm 3 \quad \mathrm{m^2 s^{-2}}$ (quoted from *Grafarend*, 1994).

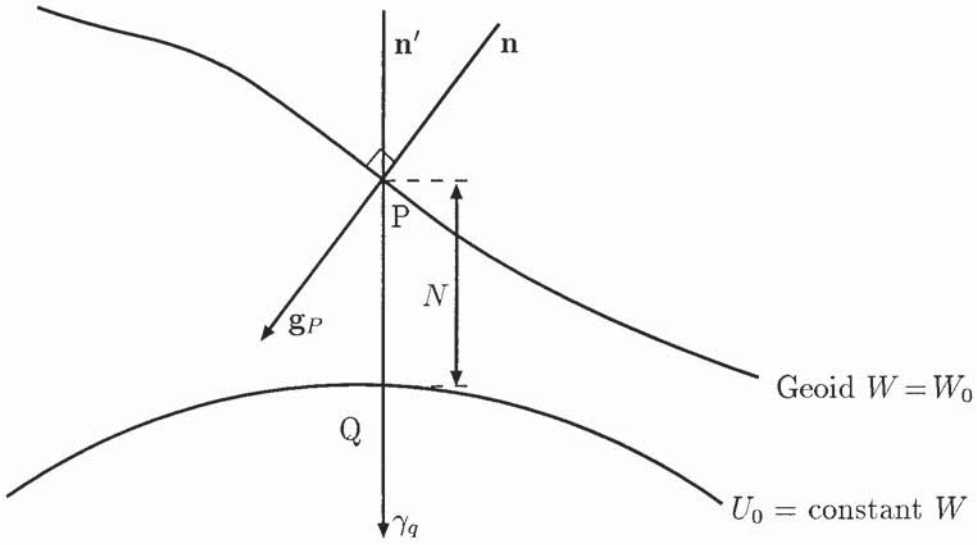

Figure 2.3: Schematic of normal ellipsoid potential, U, anomalous potential, T and their associated equi-potential, W_0 and geoid height, N. $\mathbf{n}'$, $\mathbf{n}$ are the normal unit vectors to the ellipsoid at point Q and geoid at point P with γ_q and $\mathbf{g}_P$ being their respective values of gravity.

Although there are several conventions used to describe the dimensions of the reference ellipsoid, the convention adopted within this thesis is that used for TOPEX/-Poseidon (*AVISO*, 1996) that is the Earth has a flattening, $f = 1/298.257$ and a semi-major axis $a = 6378136.3$ meters from which all other ellipsoidal characteristics

are derivable (see *Heiskanen* and *Moritz*, 1967, for example).

In addition the gravity vector $\mathbf{g}$ may be obtained from W such that

$$\mathbf{g} = -\nabla W \tag{2.4}$$

The measurable value of gravity is simply obtained from the magnitude $|\mathbf{g}|$. Its direction may also be obtained leading to the deflection of the vertical.

2.2.3 Modelling the Gravity Field

It is possible to represent the global gravitational potential through the use of an infinite spherical harmonic expansion. In such an expansion (see *Heiskanen* and *Moritz*, 1967, p.32), V is generally described for degree n and order m via the use of normalised associated Legendre polynomials, P_{nm}, and the Stokes' fully normalised associated potential coefficients $\bar{C}_{nm}$ and $\bar{S}_{nm}$.

$$V(\theta,\lambda) = \frac{GM}{r}\left[1 + \sum_{n=2}^{n_{max}}\left(\frac{R_e}{r}\right)^n \sum_{m=0}^{n}(\bar{C}_{nm}\cos m\lambda + \bar{S}_{nm}\sin m\lambda)P_{nm}(\cos\theta)\right] \tag{2.5}$$

Where, r, θ and λ are the geocentric radial distance from the Earth's centre, latitude and longitude respectively and R_e is mean radius of the Earth. Also the above expansion is truncated to a maximum degree $n = n_{max}$ as an infinite expansion is impossible due to the non-continuous global data availability.

The anomalous potential may also be modelled such that

$$T(\theta,\lambda) = \frac{GM}{r}\sum_{n=2}^{n_{max}}\left(\frac{R_e}{r}\right)^n \sum_{m=0}^{n}[\hat{C}_{nm}\cos m\lambda + \hat{S}_{nm}\sin m\lambda]P_{nm}(\cos\theta) \tag{2.6}$$

where, $\hat{C}_{nm}$ and $\hat{S}_{nm}$, are the differences between harmonics of the actual Earth and those of an equi-potential ellipsoid. It is also possible to represent the gravity field via an ellipsoidal harmonic series expansion as shown in *Heiskanen* and *Moritz* (1967).

It can be seen that the anomalous gravity field may be determined from just the $\hat{C}_{nm}$ and $\hat{S}_{nm}$ coefficients and the constant, GM/R_e. A range of gravity field models of varying degree are shown in Table 2.1 developed over almost the past 40 years.

Also of historical interest from the models are the J coefficients, namely un-

normalised zonal ($\bar{C}_{nm}$) harmonics defined by

$$J_n = -\bar{C}_{n0}\sqrt{2n+1} \tag{2.7}$$

Of particular importance is J_2 i.e., the un-normalised $\bar{C}_{20}$ which for EGM96 is 1.0826×10^{-3} and is an order 10^3 higher than any other zonal harmonic and is referred to as the oblateness of the Earth.

Model	Year	Maximum Degree	Commission error (cm)	Omission error (cm)	Source
EGM96	1996	360	±36.0	18	*Lemoine* et al. (1996)
JGM-3	1994	70	±18	91.4	*Tapley* et al. (1996)
OSU91A	1991	360	±48.7	18	*Rapp* et al. (1991)
OSU89B	1989	360	±53.6	18	*Rapp* and *Pavlis* (1990)
GEM-T2	1990	36	±130.1	177	*Marsh* (1990)
Kaula	1963	4	—	1600	*Kaula* (1966)
Izsak	1961	2	—	3200	*Rapp* (1991)

Table 2.1: A selection of Earth Gravity Models since 1961.

In order to examine the signal and error characteristics of the gravity model at each degree it is necessary to calculate the potential and error *degree variances.* The potential degree variance, D_n^2 are obtained directly from the $\bar{C}_{nm}$ and $\bar{S}_{nm}$ coefficients such that

$$D_n^2 = \sum_{m=0}^{n} \left[\bar{C}_{nm}^2 + \bar{S}_{nm}^2\right] \tag{2.8}$$

This relationship gives a direct idea of the power per degree within the potential signal as shown in Fig. 2.4(a) with the high gravity power within the long wavelengths (low degree) of the signal. *Kaula* (1966) approximated the above relationship via the model potential field.

$$D^2 = \left[\frac{10^{-5}}{n^2}\right]^2 \tag{2.9}$$

which as can be seen from Fig. 2.4(a) provides a reasonable fit though improvements exist.

In order to assess the validity of the model its error needs to be inferred. This is

achieved with error degree variances, σ_n^2 given by

$$\sigma_n^2 = \sum_{m=0}^{n} \left[\sigma_{\bar{C}_{nm}}^2 + \sigma_{\bar{S}_{nm}}^2\right] \tag{2.10}$$

Here the standard deviations $\sigma_{\bar{C}_{nm}}$ and $\sigma_{\bar{S}_{nm}}$ are either obtained as part of the model distribution or may be calculated from the error covariance matrix. σ_n^2 characteristics are shown in Fig. 2.4(b) for two models. Two parameters used to assess the error within a model are the commission and omission (or truncation) errors. The former of these is simply the sum of all error degree variances to the maximum degree. Whilst the latter is an estimate of the error due to the truncation of the series, i.e., error due to the missing signal. *Rapp* (1993) gives the omission error, O_e to degree n as

$$O_e = \frac{64}{n} \text{ meters} \tag{2.11}$$

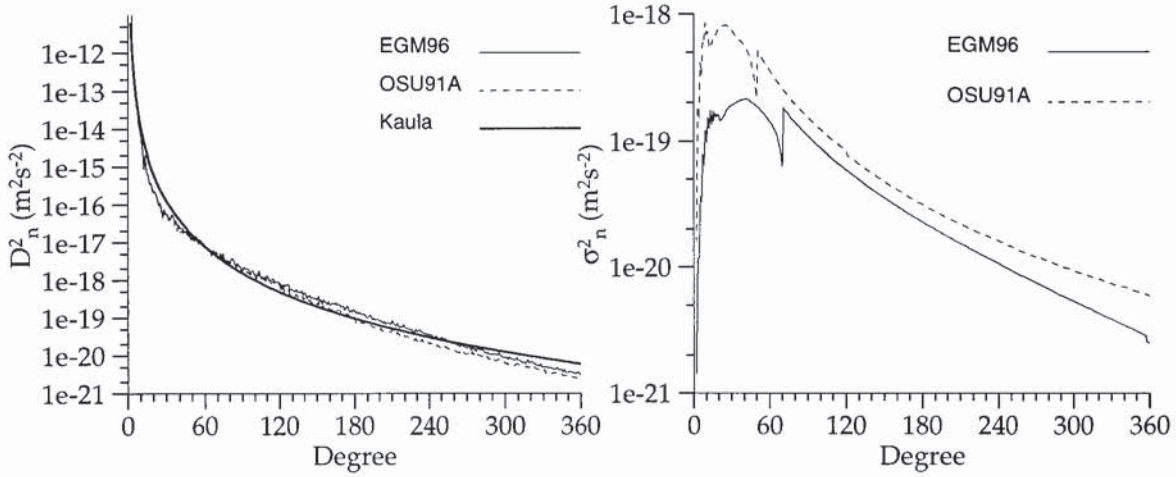

Figure 2.4: (a) Potential degree variances calculated from equation 2.8, and (b) Potential error degree variances from equation 2.10 both for OSU91A and EGM96 gravity field models and Kaula Rule.

In order to generate such models it is necessary to obtain the base observations. These can be in the form of *in situ* data collected from gravimeters or, in the last decade or so, via the use of altimetry and satellite tracking data, that may be combined for a joint solution. Each of the parameters are then solved for in

the least–squares sense to obtain the C and S coefficients yielding the normal equations.

The main problem, however, that limits the resolution and accuracy is the lack of altimetry over land and at high latitudes. Also gravimetry data is scarce over both environmentally and/or politically inhospitable regions. Hence, existing models are generally good over the oceans and locations such as North America and Europe but poor over certain parts of Asia, South America and the Poles.

The maximum resolution, θ_r of a gravity field model may be calculated (see *Rapp* and *Pavlis*, 1990) by

$$\theta_r{}^\circ = \frac{180}{n} \tag{2.12}$$

and the spatial resolution R_{max} may be approximated to

$$R_{max} = \frac{2\pi R_e}{2n} \approx \frac{20000}{n} \text{ km.} \tag{2.13}$$

Thus a 360 × 360 model will achieve a spatial equatorial resolution of 100 km or 0.5° (30′). This maximum resolution (at the time of writing) has its use for general purposes models. However, if more detailed studies are required then other techniques are required. These techniques may be split into two categories where harmonic decomposition is limited, these are,

1. Ocean: Here high density altimetry may be incorporated improving resolution to a maximum of 4 km at the equator (see chapter 3). This may be further improved if only regional mapping is required as the resolution increases with the cosine of the latitude.

2. Land/Ice: Regional gravity anomaly data collection programmes can allow resolution improvements dependent on the spacing of measurements.

The most recent model to make significant impact is the EGM96. The model is a joint solution using JGM3 to degree 70 and developed to degree 450 truncated at $n = 360$. Here, large amounts of gravimetry data were released by the U.S. National Imagery and Mapping Agency (NIMA), NASA, Kort Matrikelstyrelsen and the University of Leeds. In addition to satellite tracking and altimetry the data has allowed vast improvements on previous high degree models, i.e., OSU91A. The EGM96 plays a major role in MSS models developed later.

2.2.4 Gravity Field Parameters

There are three gravity field parameters that are heavily used for studies carried out within this thesis. These are the *geoid*, *deflection of the vertical* and *gravity anomaly*.

The geoid may be described via the use of *Brun's* formula describing geoidal height, N, in meters above a reference best fitting ellipsoid, by the anomalous potential, T, and the normal gravity, γ, via

$$N = \frac{T}{\gamma}. \tag{2.14}$$

The geoid deviates between -105 and 85 meters from the reference ellipsoid and may also be expanded via spherical harmonics. Here the substitution of equation 2.14 into equation 2.6 gives

$$N(\theta, \lambda) = \frac{GM}{\gamma R_e} \sum_{n=2}^{n_{max}} \sum_{m=0}^{n} [\hat{C}_{nm} \cos m\lambda + \hat{S}_{nm} \sin m\lambda] P_{nm}(\cos\theta). \tag{2.15}$$

Typically, the geoid undulation accuracy, reported by *Rapp* (1994), for the OSU91A are ± 10, ± 25 and 50 cm over ocean, land and land devoid of gravity data coverage; the commission errors for two models are given in Fig. 2.5

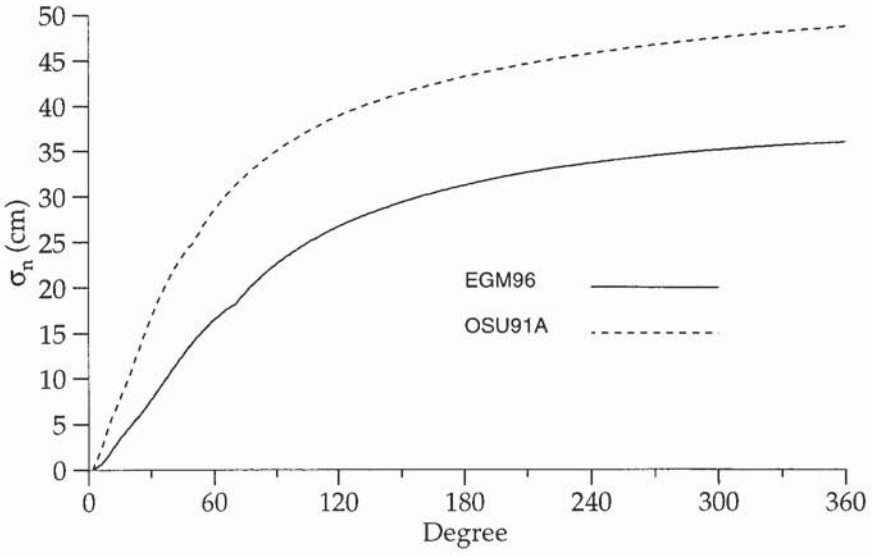

Figure 2.5: Cumulative geoid undulation errors calculated for OSU91A and EGM96 gravity field models giving commission errors of 48.7 and 36.0 cm respectively.

The *Deflection of the Vertical* (DOV) is a term traditionally used to explain

the angle a plumb line is deflected from the vertical (perpendicular to the normal ellipsoid) when moved near a large mass such as a mountain. They are measured in micro–radians (μrad) and are generally between ± 500 μrad. DOV's are expressed as a vector quantity, $\mathbf{d}$, i.e.,

$$\mathbf{d} = \eta\hat{\mathbf{i}} + \xi\hat{\mathbf{j}} \tag{2.16}$$

where, η and ξ are the north and east DOV components respectively. η and ξ may be determined from the anomalous potential, i.e., from equation 2.6

$$\eta = -\frac{1}{\gamma}\frac{\partial T}{\partial x} \tag{2.17}$$

and

$$\xi = -\frac{1}{\gamma}\frac{\partial T}{\partial y}. \tag{2.18}$$

Ultimately the DOV components can be calculated simply from sea surface heights as we shall see in chapter 5.

The gravity anomaly, Δg, is an important geophysical parameter being directly measureable via the use of a gravimeter and ultimately may be converted to geoidal information or used to validate other methods of derived gravity anomaly fields. It is described as the difference between the actual value of gravity signal and the normal ellipsoidal gravity, γ

$$\Delta g = g|_{geoid} - \gamma|_{ellipsoid} \tag{2.19}$$

and may also be determined from the anomalous potential such that

$$\Delta g = \frac{\partial T}{\partial r} - \frac{2T}{r}. \tag{2.20}$$

The gravity anomaly is measured in milli–Gals (1 mGal = 10^{-5}ms^{-2}) and varies approximately between ± 500 mGal. Gravity anomalies also have the advantage of being in–phase with the gravity field and may be collected easily via the gravimeter. Maps of this parameter, as we shall see in chapter 8 contain high frequency information ideal for the locating of small–scale tectonic features and sea-mounts.

2.2.5 Description of Boundary Value Problems

There are a number of classical boundary value problems tackled in chapter 5 that allow the determination of small scale details regarding the gravity field.

To begin with, inside the Earth's boundary Poisson's equation holds, i.e

$$\nabla^2 T = -4\pi G\rho \tag{2.21}$$

Where, the ∇ operator is given by

$$\nabla = \frac{\partial^2}{\partial x^2} + \frac{\partial^2}{\partial y^2} + \frac{\partial^2}{\partial z^2} \tag{2.22}$$

On the surface or outside the Earth Laplace's equation holds, namely,

$$\nabla^2 T = 0 \tag{2.23}$$

It is in the solution of these two equations, either spherically or by a flat Earth approximation, from which we are able to determine, in the small scale, detail about the Earth's gravity field. However the inverse problem allowing the measurement of such properties as the density structure are highly complex.

There are two theoretical models adapted within this thesis that allow the transformation of geoidal data to gravity anomalies and DOV's and vice–versa. The first of these is the *Stokes'* transform *Stokes* (1849) that enables gravity anomaly information to transform into geoidal height and vice–versa with the inverse transformation. Secondly, an adapted use of the *Stoke's* transform allows a direct transformation of gravity anomalies into DOV's (and vice–versa): this is the *Vening–Meinesz'* transform as described in *Heiskanen* and *Moritz* (1967).

It is a combination of the above transforms that provides the basis in chapter 8 for integrating altimetry data sets. Additionally, for descriptive purposes only, if the physical surface of the Earth is to be determined over land we encounter *Molodensky's* problem; here the geoid does not coincide with the physical surface and gravity anomalies cannot simply be incorporated into *Stoke's* transform. Additional theory is required to correct for the effect of topographic masses resident outside the geoid (see *Schwarz* et al. (1990) and *Moritz* (1980)) in these cases.

2.2.6 Practical use of the Geoid and Gravity Anomaly

Some uses of the gravity field have already been mentioned, for example, the aging of the sea–floor and *Paleo*–Tectonic reconstruction. In fact the applications are

numerous and steadily growing.

The biggest benefit will undoubtedly be gained by the oil and mineral prospecting industry, who incidentally are financing this type of research. With our knowledge of the gravity field and with the use of aeromagnetic surveys revealing localised magnetic fields certain inferences may be made of the location of sedimentary basins removing the need for the possibly erroneous and expensive method of lowering gravimeters to to sea–floor (*Hayling*, 1994).

A long–term objective is to gain a better knowledge of the lithospheric structure including the *Moho* depth and tectonic stress and strain fields. Unfortunately, inferring such information is complex since we have to rely on the gravity field measured from outside the Earth's surface. However with the use of isostatic compensation models such as those of Pratt and Airy (see *Cazenave*, 1994) it is possible to make reasonable guesses at these properties. Our knowledge of the sea–floor topography is still limited although high resolution gravity anomaly fields have revealed new features of the sea–floor, including sea–mounts. Secondly, with such features pinpointed it is then possible to use shipboard multi–beam sonar to map such regions improving the resolution down to meters which, as we will see in chapter 3, is a vast improvement. Finally, refinement of the gravity field will improve navigational systems on–board aircraft and submarines.

2.3 Oceanographical Characteristics

The oceans provide several processes vitally important to the function of the Earth's ecosystem. These are broadly

1. The heat capacity providing the storage of energy allowing the *damping* of short term fluctuations in temperature.

2. The heating mechanism of the oceans mainly provided by its coupling to the atmosphere. Heating occurs in the equatorial tropics with cooling at higher latitudes.

3. The storage of nutrients important to the fishing industry and dissolved gases significant for the climate.

Ultimately, it is the formation of currents by density, salinity and temperature gradients that provide the large–scale transportation of water. All require high resolution sampling for global energy balance studies. Measurement of one of the

end products, the surface height, is therefore critical in understanding the general ocean circulation and the coupling effect with the rest of the climate system.

2.3.1 Ocean Dynamics

The sea surface consists of two structural components. The main component is the marine geoid with the second being the result of forces acting on this surface causing its deformation. If none of these forces existed the sea surface would conform with the marine geoid. However this is not the case and the forces are caused by tidal attraction and pressure gradients due to the formation of the current systems which, reiterating, are due to changes in density, salinity and temperature. The forces caused by pressure gradients are approximately geostrophically balanced by the action of the Coriolis force, an effect caused by the movement of currents on a rotating Earth. In addition, frictional forces are due to wind stress and internal forces in the upper ocean (*Pond* and *Pickard*, 1983).

The overall effect of these forces gives rise to an anti–clockwise circulation around low pressure systems in the Northern Hemisphere as opposed to clockwise circulation in the Southern Hemisphere. Expanding these terms analytically gives

$$\frac{\mathrm{d}\mathbf{v}}{\mathrm{d}t} = -\frac{1}{\rho}\nabla P + f\mathbf{v} \times \mathbf{k} + \mathbf{F} \tag{2.24}$$

where,

- $\mathbf{v}$, is the velocity vector;
- ρ, is the density;
- P, the pressure;
- f, the so called Coriolis parameter;
- F, the friction forces and
- $\mathbf{k}$, the $z-$ direction unit vector.

In equation 2.24 the first term on the RHS is the pressure gradient force, the second is the Coriolis force and the third friction. Expanding the Coriolis force gives

$$f\mathbf{v} \times \mathbf{k} = 2\Omega \sin\phi(\mathbf{v} \times \mathbf{k}) \tag{2.25}$$

where, Ω is the rotation of the Earth ($2\pi/24\text{hrs} = 7.2722^{-5}$ rads^{-1}). Thus it can be seen that at high latitudes where $\phi \longrightarrow 90°$ the force diminishes. Also $\mathbf{v} \times \mathbf{k}$ is

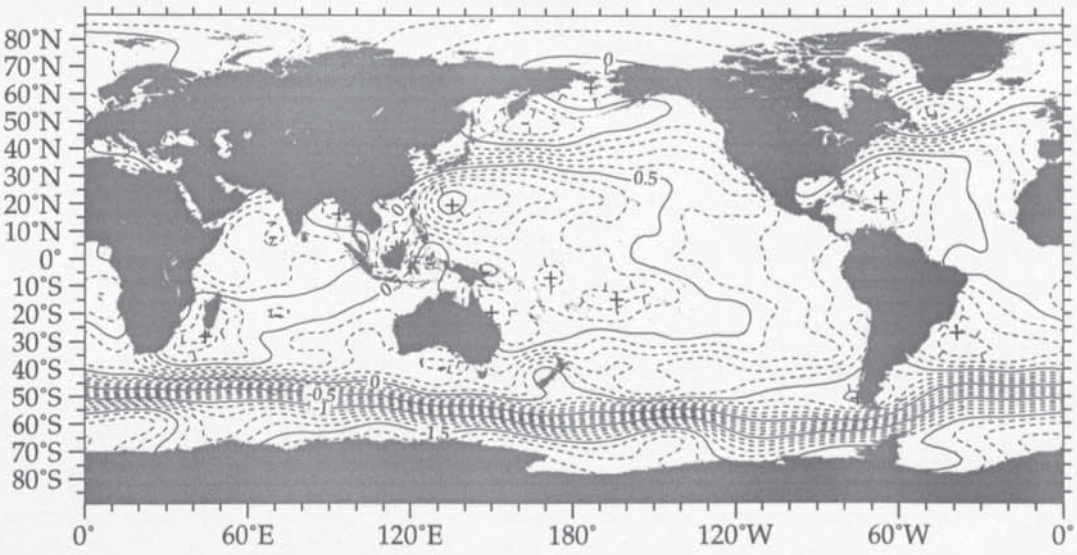

Figure 2.6: EGM96 Quasi–stationary Sea Surface Topography contour map to degree and order $n = 20$. Dashed contours are at every 0.1 m whilst annotated solid line contours are spaced at 0.5 m. The model is determined using a semi–major axis, $a = 6378136.3$ and flattening, $f = 1/298.257$.

the direction of the Coriolis force directed away from the low pressure system.

Ultimately, from altimetry it is feasible to measure the general circulation from which surface slopes may be determined. Velocity fields can be computed from these slopes thus improving the knowledge of the ocean–atmospheric coupling system. Also, since the oceans are stratified it is possible to calculate velocities at depth.

2.3.2 Quasi–stationary Sea Surface Topography (QSST)

The topography that exists due to the dynamic movement of water, i.e., the general mean circulation is known as the QSST. Following *Nerem* et al. (1990) the dynamic topography, ζ may be calculated from the expansion

$$\zeta(\theta,\lambda) = \sum_{n=1}^{n_{max}} \sum_{m=1}^{n} \left[\bar{C}_{nm} \cos m\lambda + \bar{S}_{nm} \sin m\lambda\right] \bar{P}_{nm}(\sin\theta) \tag{2.26}$$

Here parameters are the same as those specified for Eq. 2.5. The SST model provided with the EGM96 release is shown in Fig. 2.6.

2.3.3 Sea Surface Variability (SSV)

The sea surface height deviates from the marine geoid plus the QSST due to the thermal expansion of the oceans, with other variations occuring in frictional stresses and fluctuations of density, salinity and temperature all on a wide range of scales.

Any one of these complex changes can result in the diversion of currents and can explain how we may *observe* El Niño events – essentially the semi–periodic flow of warm water across the central Pacific from east to west resulting in measurable sea height changes and the well documented ecological after effects.

On the other hand there are seasonal variabilities that may simply be explained as, for example, the seasonal thermal expansion of the oceans providing a 180° phase difference in level in the two hemispheres.

2.3.4 Planetary and Gravity Wave Disturbance

In addition to the oceanic phenomena described above it has been possible in recent years to observe the propagation of features at wavelengths corresponding to planetary and gravity wave disturbances. Such phenomena are western propagating Rossby[1] and equatorial eastern propagating Kelvin waves respectively (see *Pond* and *Pickard* (1983) and *Houghton* (1991)).

2.4 MSS Definition and Review of Current Models

The mean sea surface, $M(\phi, \lambda)$ above a reference ellipsoid, can be defined as the instantaneous sea surface heights, $h_i(\phi, \lambda)$ at locations over the oceans time averaged over a suitable period (1–2 years). So over n observations using geodetic latitude and longitude coordinates, ϕ, λ

$$M(\phi, \lambda) = \frac{1}{n} \sum_{i=1}^{n} h_i(\phi, \lambda) \tag{2.27}$$

[1] *Parke* et al. (1998) notes the problems with the aliasing of TOPEX/Poseidon data with respect to its repeat period causing the appearance of Rossby waves.

where, i is the observation index. Equation 2.27 may be analytically approximated by 4 components given by

$$M(\phi,\lambda) = \frac{1}{n}\sum_{i=1}^{n}\left[N_i(\phi,\lambda) + \zeta_i(\phi,\lambda) + \nu_i(\phi,\lambda,t) + \kappa_i(\phi,\lambda,t)\right]. \tag{2.28}$$

In equation 2.28, N, the geoid is assumed to remain constant over such time–scales, ζ is the quasi–stable sea surface topography, ν is the sea surface variability (SSV) and κ a collective function containing errors in all other components.

The data most suited to provide us with a MSS is satellite altimetry. Its raw data contains a range of errors that need removing to allow the MSS to be precise. These errors are broadly categorised at satellite orbit error, tidal effects, environmental and sea surface effects and are dealt with in detail in chapter 4.

The choice of altimetry data we use is determined by the satellites ground–track spacing. This is defined from orbit design (see *Parke* et al., 1987) and there are a number of ground–tracks available, see Fig. 2.7. For our purposes we require the highest density ground–tracks whilst retaining accuracy. Thus we require ERS-1 and GEOSAT Geodetic phase data, though as we shall see, GEOSAT is comparatively inaccurate. Additionally however, the ERS-1 35 and T/P 10 day repeat orbits allow the *stacking* of data, that is, the averaging of data over repeat passes at the same location, thus allowing the advantageous reduction of noise within the signal and minimisation of variability. Also, as mentioned in chapter 1, TOPEX/-Poseidon provides the most precise measurements. Its inclusion would allow very accurate MSS models but only over its ground–track. Again referring to Fig. 2.7 this leaves large areas poorly modelled. Thus its inclusion only serves to provide a datum for reference by T/P data. However, it does provide a useful source of validation.

Modern, that is post T/P launch, MSS models use a range of data sets, namely a year or two worth of stacked repeat data to minimise variability and a high density data set, such as ERS-1 geodetic phase. The methods of MSS computation vary from an attempt at spectral optimal interpolation by *Jolly* (1995), the fitting of surface splines (*Kim* et al., 1994) to the optimal interpolation of the integrated data sets for example, *Cazenave* et al. (1996) and *Yi* (1995). With regard to the above it is necessary to address a few points in view of possible improvements that are investigated here.

1. The fact that the ERS-1 geodetic phase contains no repeat data means the existence of variability information that results in the appearance of cross–track

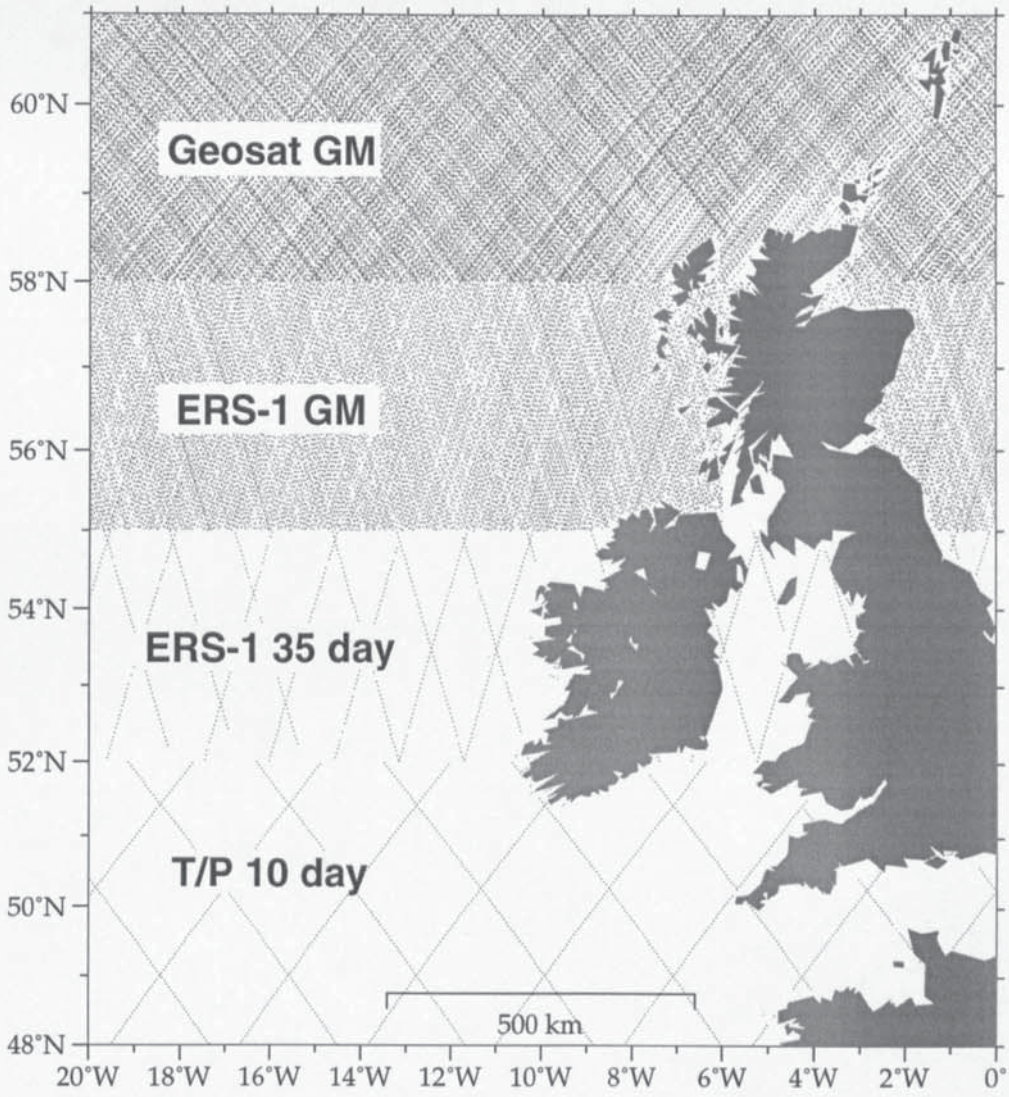

Figure 2.7: Selection of Ground–track patterns for (beginning at the bottom of the figure) T/P, ERS-1 35 repeat, ERS-1 Geodetic Phase and top GEOSAT GM.

gradients in regions of high variability (i.e. The Gulf stream and Kuroshio Currents). It has been suggested by *Rapp* and *Nerem* (1995) and *Yi* (1995) that a correction is calculated from cross–track gradients to account for this. However, since there are now methods available to generate variability, data could this be used to remove variability from non-repeat data thus solving the problem of a correction?

2. In the case where optimal interpolation is used, it is required, as will be shown in chapter 5, that a covariance knowledge of the errors within the pre–interpolation altimetry surface is generated. In the above mean sea surfaces, the covariance is generated from separate covariance models of each of the

major contributive errors. The question is asked here whether this may be generated directly from the data itself?

3. Optimal Interpolation of a global high resolution surface in the spatial domain requires the time consuming inversion of a large matrix. In this study we adopt the use of Fourier domain techniques that have been shown to reduce processing time despite the need to fast Fourier transform (FFT) several parameters. The FFT allows the effective multiplication of parameters at each individual frequency by the optimal interpolation least–squares estimator. A complete theoretical treatment of these techniques is provided in chapter 5 that will also show the transform's inherent shortfalls.

4. Validation is made for published models against T/P sea surface heights. However since the above models all contain at least a years worth of T/P data then this validation is non–independent and arguably invalid. Hence, it is necessary to test a model against independent data and so the MSS generated within this thesis does not employ T/P data: this permits free validation.

5. A great deal of processing is required to generate MSS models and new models require the complete re–processing of all data. The case of integrating new data into an upgraded MSS is investigated with the specific case of integrating GEOSAT GM data with poor orbit determination with one generated from the ERS-1 GM. The case suggested is unique though it does draw on a combination of techniques utilising both inverse Vening–Meinesz' and forward Stokes' transforms within the Fourier domain. The technique allows the generation of a gravity anomaly field providing the possible inclusion of alternative gravity data to improve the algorithm

2.5 Conclusion

A global high resolution MSS is derivable using a range of altimetry data. The method proposed here is a spectral optimal interpolation technique to reduce processing time and enable additional filtering if required. In addition, the integration of MSS models is investigated. In order to achieve the above we need to examine the operation of the altimeter to assess the instrument resolutions and accuracies attainable (Chapter 3) and outline the range of corrections required to reduce errors within the measurement (chapter 4).

The necessary theory to perform spectral optimal interpolation and the spectral Stokes' and Vening–Meinesz' transforms is dealt with in chapter 5 leaving results and methodology to commence in chapter 6.

Chapter 3

Geophysical Parameter Estimation From Radar Altimetry

3.1 Introduction

In this chapter the function of the radar altimeter and the information it receives is explained. Altimeter design requires a high level of precision and innovation, since, a large number of parameters are beyond the designers control. Others, however, have only marginal adjustability.

Original radar altimeter design methodology as demonstrated by *Moore* and *Williams* in 1957 was based on near vertical reflections of microwave pulses over terrain utilising two differing propagation geometries. The realisation that the airborne altimeter had uses for measurements over the ocean surfaces was subsequently followed with the transition to space in 1973 (*McGoogan* et al., 1974). This commenced with the experimental S-193 instrument on–board the orbiting SKYLAB platform resulting in the much needed breakthrough in sea surface observation. Furthermore, analysis of received waveforms have not only revealed information concerning sea–surface height (SSH) but also allowed for the extraction of various geophysical parameters. In particular, Significant Wave Height (SWH or $H_{1/3}$) and backscatter coefficient (σ^0) that gives wind speed information on global scale. Such parameters have proved invaluable for todays scientific needs.

With the move to spaceborne instrumentation, a host of new problems emerged, including the need for precise satellite orbit determination and models to account for atmospheric propagation and surface scattering effects (see chapter 4.) Additionally, the need for higher transmit power, due to increased propagation distances, brought concern for greater system mass. Once the possibilities of global altime-

try became apparent ever more precise measurements within certain error margins have been demanded. Scientific effort has made this possible with error removal becoming more efficient as more data becomes available and models improve.

Hardware improvements have been those reflecting the need to upgrade the instrument in terms of speed and signal tracking capability. More recently, an innovative idea to solve for ionospheric path delay problems has been incorporated into the design of TOPEX (see section 4.4.2). All of these advances incorporate state–of–the–art space qualifiable technology.

By analysing the instantaneous area the radar radiates on the Earth's surface it is possible to define the highest resolution attainable for MSS and gravity anomaly models. An orbit can be designed to cater for such resolutions. As we shall see, at the highest frequencies, errors are aliased into our end product since large variations in footprint size exceed the ground–track spacing of the altimeter.

Finally, in section 3.3 we look at any probable, or even desirable, design upgrades that are likely to occur in the forseable future.

3.2 Functional Design of the Radar Altimeter

In its simplest form the single frequency radar altimeter is an instrument positioned in such a way that pulses transmitted from an antenna will, after some time, reach a scattering surface at near–normal incidence. Scattered pulse energy is received back at the same antenna at time t_d after transmission. If the altimeter is fixed in a vacuum, the vertical distance, h, above the surface is given as a function of the two–way pulse travel time, t_d in seconds by

$$h = c\frac{\Delta t}{2} \tag{3.1}$$

where, c is the speed of light in a vacuum (3×10^8 ms^{-1}) and h in meters.

The dual frequency radar altimeter works on the same principle (*Marth* et al., 1993), although after several pulses at one carrier frequency a pulse at a different carrier frequency is transmitted. This, as we shall see in section 4.4.2, allows a more accurate ionospheric correction.

In order to test a simple radar system it is required to quantify a number of initial parameters namely:

1. The carrier frequency chosen for a practical antenna size and to minimise frequency dependent atmospheric attenuation whilst residing within the internationally allocated bandwidth.

2. The power requirement enabling the transmission of pulses over large distances (>1400 km two–way path length) that may be received and resolved from noise floor.

3. Maintain a high vertical range resolution.

These parameters, see table 3.1, should be chosen to optimise the received Signal–to–Noise Ratio (SNR).

Absorption characteristics throughout the microwave region of the electromagnetic spectrum show low absorption at frequencies less than 15 GHz and at ~ 37 GHz. The first band is chosen for low atmospheric absorption whereas higher frequencies (shorter wavelengths) suit a higher antenna gain, G in decibels (dB), given by

$$G(\mathrm{db}) = 10 \log \frac{4\pi A_e}{\lambda} \tag{3.2}$$

where, λ is the wavelength and A_e is the effective, rather than physical, antenna area in m^2.

The trade off between antenna gain, frequency bandwidth availability and absorption allows a choice within the frequency range 13–14 GHz and additionally, for dual frequency altimeters, between 3–5 GHz (see section 4.4.2.)

The parabolic antenna is traditionally chosen almost entirely due to its high gain (typically 41 dB) for a relatively small dish size (1.2m). All numerical examples are based on the ERS-1/2.

The main criterion over which all else prevails is the need to measure range very precisely. For this to take place the altimeter is required to transmit a large number of very short duration pulses with high Pulse Repetition Frequency (PRF). However, as the energy contained within each pulse is reduced, the narrower pulse yields too low an energy to maintain appropriate SNR. Also, the Nyquist sampling theorem imposes a further limit since space qualifiable technology is not available to maintain such high sampling rates.

As a result the conceptual altimeter described above fails the requirement of high range resolution. Pulse compression is used to overcome this shortfall.

3.2.1 Full–Deramp Pulse Compression

The method used to compress transmitted pulses is termed full–deramp processing (*Chelton* et al., 1989) and is shown schematically in Figure 3.1. The process

allows the transmission of long uncompressed pulses with high PRF containing the required amount of signal power, whilst maintaining high range resolution and reducing signal noise.

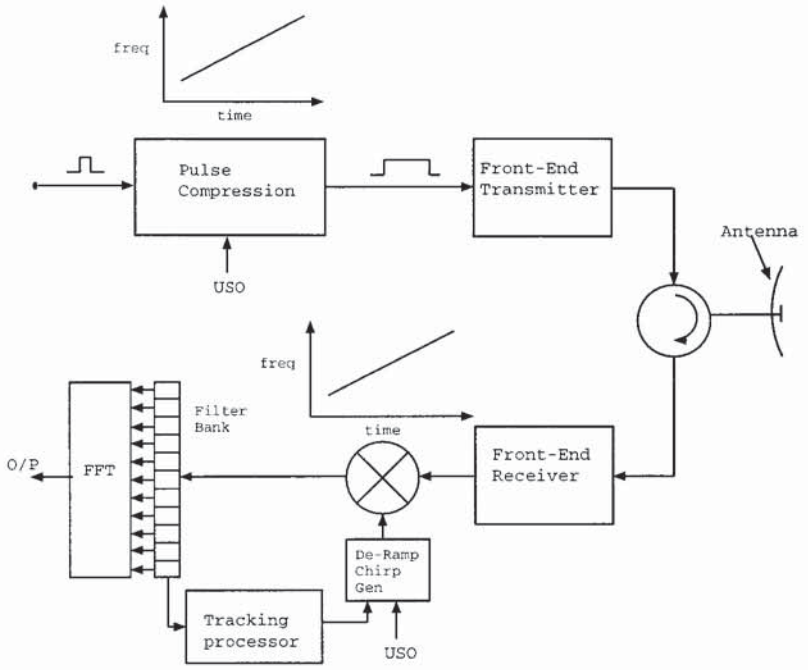

Figure 3.1: Diagram showing the operation of a single–frequency radar altimeter. Following triggering, a pulse is compressed, amplified and directed to the antenna via the three port circulator. Received waveforms are directed to a cooled receiver, mixed with a de–ramping chirp, filtered into 64 filter banks and processed via the FFT for conversion to range.

This is achieved by mixing each pulse with a linear Frequency Modulated (linear FM) chirp. A chirp is a signal whose frequency increases, or decreases, linearly with time. Such a signal, $u(t)$, is represented by the expression

$$u(t) = A \exp\{\imath \pi k t^2\} \tag{3.3}$$

where, A, represents pulse amplitude, k, a constant multiplier and the imaginary operator $\imath = \sqrt{-1}$. The phase of the signal is contained within the curly brackets $(\imath \pi k t^2)$. Thus instantaneous frequency may be found via differentiating the phase term with respect to time yielding a linear relationship (hence linear FM).

The chirp dimensions are determined by its frequency sweep, ΔF, over the pulse length, Δt (see Fig. 3.2a.) The chirp rate, ΔC is simply

$$\Delta C = \frac{\Delta F}{\Delta t}. \tag{3.4}$$

The compressed pulse length, τ, is now determined purely from the chirp sweep frequency (bandwidth), ΔF. Hence,

$$\tau = \frac{1}{\Delta F}. \tag{3.5}$$

Typical values would give a chirp bandwidth, $\Delta F = 330$ MHz, for an uncompressed pulse length, $\Delta t = 20\mu$S at a PRF of 1020 Hz. Therefore a compressed pulse of length, τ= 3.03 nS is achieved. This eventually caters for a good signal–to–noise ratio and range resolution.

The surface range is finally determined by mixing received pulses with a local oscillator at the same chirp rate, ΔC (see Fig. 3.2b.) This is known as the de–ramping chirp and is triggered at the precise moment to remove the linear–FM signal. The sea surface at varying ranges, δr, is translated to variations in frequency, δf (see Fig. 3.2c), given by

$$\delta f = \frac{\Delta F}{\Delta t}.\frac{2\delta r}{c}. \tag{3.6}$$

Full waveforms are extracted by spectrally analysing analogue–to–digitally converted received signals via the use of the fast Fourier transform (FFT).

3.2.2 The Range Window

The frequency domain waveforms are filtered using a bank of 64 filters[1], each of which have a total bandwidth, B_T equal to the reciprocal of the uncompressed transmitted pulse, Δt. Each filter of bandwidth, $B_i (i = 1, \ldots, 64)$, represents a spatial region, Δr, known as a range bin which can be determined via the modification of equation 3.6 giving

$$\Delta r = \frac{cB_i}{2\Delta F/\Delta t} = \frac{c}{2\Delta F} = \frac{c\tau}{2}. \tag{3.7}$$

For the ERS-1 in ocean mode, each filter, Δr, covers a total bin range of 0.45 meters. Therefore the 64 filters can cover a total window range of 29 meters. Loss–of–track will occur if the signal appears outside this limit and so constant monitoring is required to adjust for the changes in sea–level. An adaptive tracking system is used (described more comprehensively in section 3.2.6) to track the half

[1]Missions such as TOPEX and ENVISAT–1 are now employing 128 range bins.

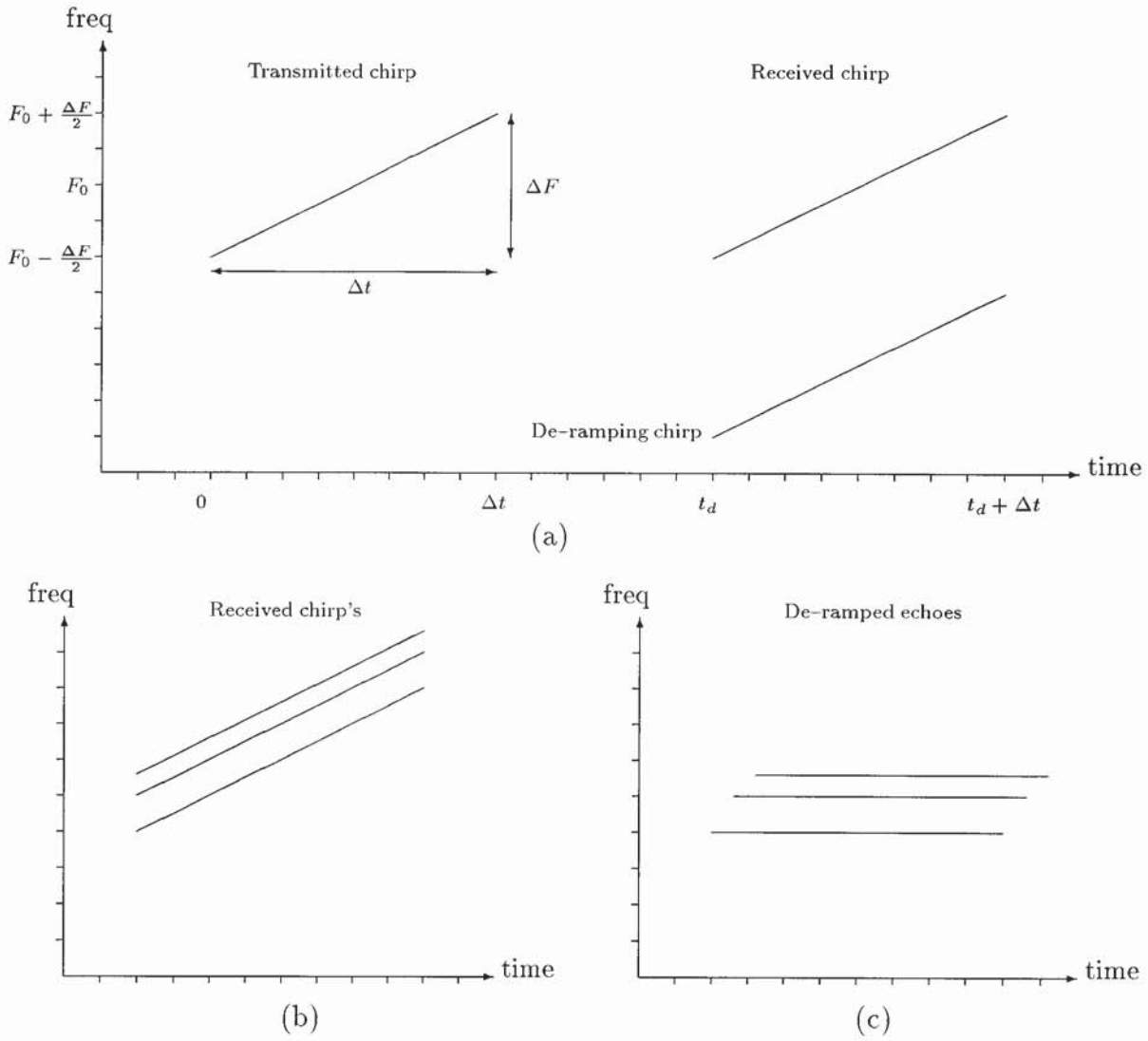

Figure 3.2: Schematic pulse compression waveforms. (a) A linear FM chirp is transmitted at a carrier frequency F_0 with a bandwidth ΔF. The pulse is transmitted over a time period equal to Δt. An echo is received after a total transmission delay, t_d, at which time a de-ramping chirp is precisely triggered by a local oscillator. (b) Received echoes over a topographic surface result in variations in their frequencies. (c) De-ramped echo frequencies requiring spectral processing correspond to variations in surface range.

power point to a particular tracking gate within the range window (see Figure 3.3).

It is also possible to determine SWH, the pointing angle of the antenna from off-boresight loss and Automatic Gain Control (AGC) from the waveform. The determination of these parameters from the characteristic waveform shape is given in section 3.2.5. The final range resolution is then achieved by the means of an effective expansion of the tracking gate into a number of smaller gates. An interpolation scheme over the sampled waveform points is then used to determine precise range. Antenna pointing may additionally be monitored by measuring power within the

last few range bins.

3.2.3 Pulse and Beam Limited Altimetry

With current technology it is necessary to choose a combined method of pulse compression and frequency processing to allow useful range resolution capability. In addition we also require determination of the horizontal resolution and information regarding the variable ocean surface.

There are two geometrical methodologies discussed here. The one used for the space borne radar altimeter is known as the Pulse–limited Altimeter (PLA) operation. In order to explain the PLA function a simpler method, known as the Beam Limited Altimeter, is first described.

From simple pulse and antenna theory (*Kingsley* and *Quegan*, 1992), the simple Bragg diffraction theory yields the relationship governing the main beam–width, θ_b, of an antenna, to its aperture diameter, d, in meters, operated at a wavelength, λ, i.e.,

$$\theta_b \sim \frac{\lambda}{d} \text{ rad.} \tag{3.8}$$

The antenna radiates energy and illuminates a circular area, known as the footprint (see Fig. 3.4a and b), on the Earth's surface h meters away. The footprint diameter, D_{BLF}, is therefore

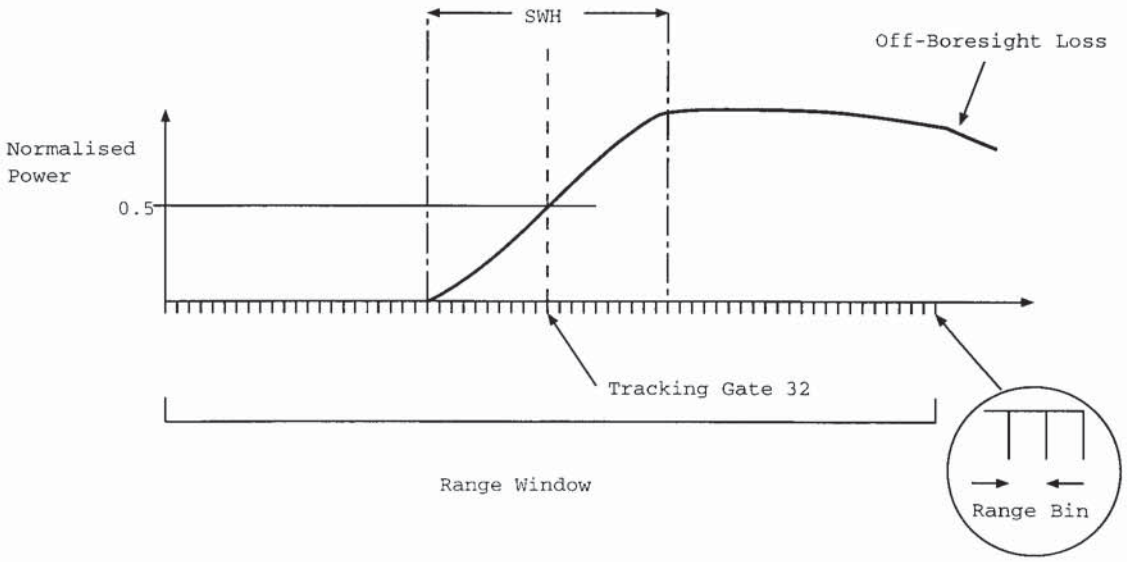

Figure 3.3: Schematic for mean received power waveform showing individual range bins and various parameters that may be subsequently determined.

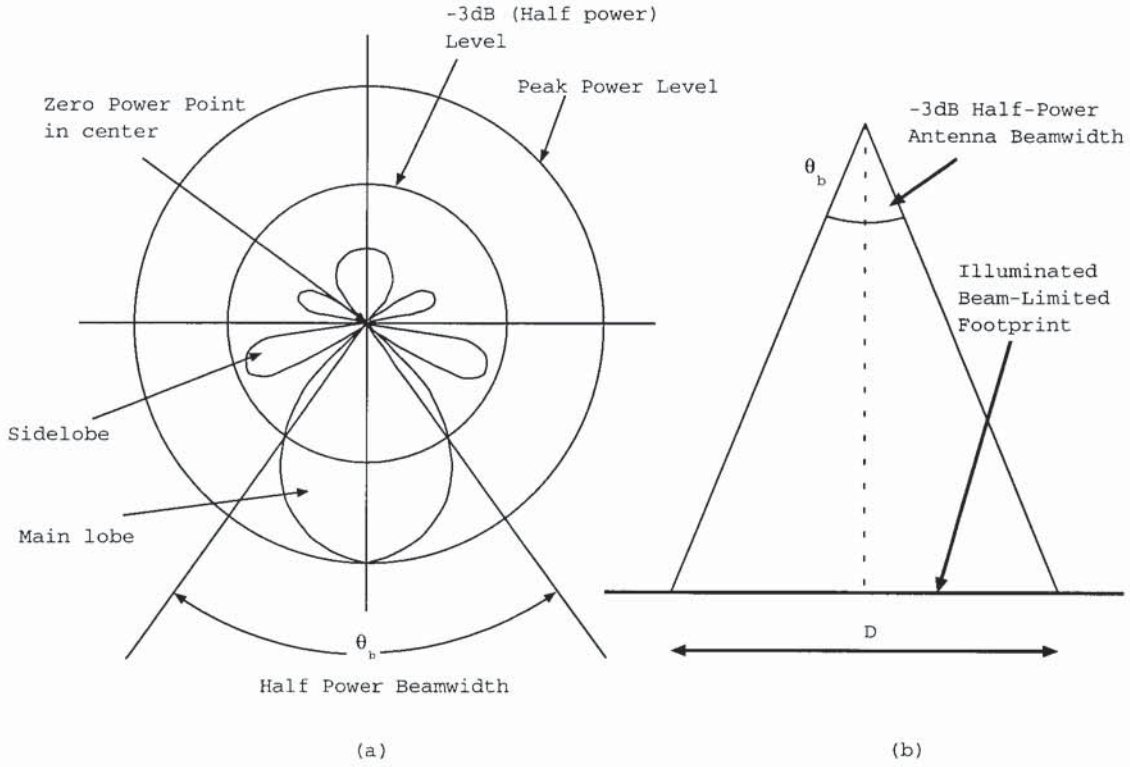

Figure 3.4: (a) Schematic parabolic antenna pattern displaying high main–beam gain with low side–lobe gain and (b) Beam–limited footprint determined from 3 dB beamwidth.

$$D_{BLF} = \frac{h\lambda}{d}. \tag{3.9}$$

Hence, for a typical altimeter antenna of aperture diameter 1 meter, operating at a carrier frequency of 13.8 GHz ($\lambda \sim 2.2$ cm) at a height of 800 km, the footprint size would be 15 km. However, if the frequency and altimeter height are retained and a reduction in footprint to a 1 km diameter is desired, the antenna diameter would now be an unfeasible 27.6 meters. Thus, for observing the ocean surface another approach is required leaving beam–limited altimeters for land/ice topography studies (see *Elachi*, 1988). An approach that counters the need for large antenna size whilst retaining (via only minimal design modification) hardware design is the PLA. In the pulse–limited operation a short pulse is radiated from the antenna, as shown in Figure 3.5a, and reaches, for reasons of description only, a diffuse surface such as a calm ocean. At time, $t = 0$, the spherical shell of radiation illuminates a surface area that increases linearly with time until the falling edge of the pulse intersects the surface at $t = \tau$.

The radius of the pulse–limited footprint can be derived by considering the ge-

ometry in Figure 3.5b. From Pythagoras' theorem the radius of the footprint, r_{pla}

$$r_{pla} = \sqrt{hc\tau} \tag{3.10}$$

Following this time, the area illuminated resembles an expanding annulus which fades as the annulus reaches the edges of the main beam–limited area. The inner radius of the n^{th} annulus is given by

$$r_n = \sqrt{nhc\tau} \tag{3.11}$$

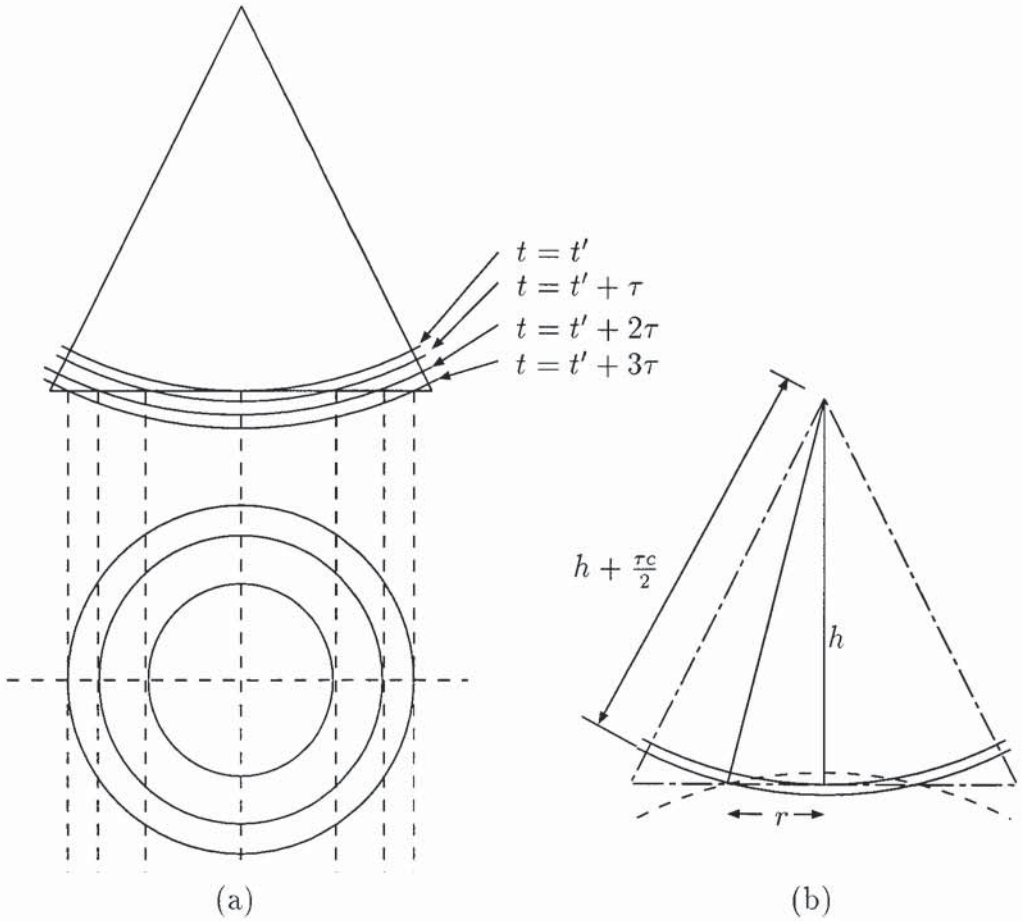

Figure 3.5: (a) Pulse–limited altimeter operation displaying how the reduced footprint is generated and the subsequent annular rings. t' represents the one way travel time of a pulse's leading edge radiating from an antenna to it reaching the *flat* surface at nadir. (b) Geometry for a single pulse of length τ.

and the area of the n^{th} annular ring may now be determined

$$\begin{aligned} A_{annulus} &= \pi r_{n+1}^2 - \pi r_n^2 \\ &= \pi(n+1)hc\tau - \pi nc\tau \\ &= \pi hc\tau \end{aligned} \tag{3.12}$$

The single pulse area of the footprint is also given as.

$$A_s = \pi hc\tau \tag{3.13}$$

Equation 3.13 specifies the flat Earth approximation for the sea surface footprint. *Chelton* et al. (1989) derives the relationship, A_{se}, for a spherical Earth of radius, R_e, giving

$$A_{se} = \frac{\pi hc\tau}{1 + h/R_e} \tag{3.14}$$

The real ocean surface is in fact far more complex than the diffuse smooth surface geometry. The footprint area actually varies as a function of wave state, shown schematically in Figure 3.6. The earliest signal returns emanate from wave crests of closer range than the hypothetical flat surface; reflections deeper within the wave then contribute and finally the reflecting facets within the troughs of the waves. The effect is a footprint that approximates to that of a smooth surface for calm sea conditions but increases with sea–state. As a theoretical tool, a measure of wave conditions is defined as the significant wave height (SWH) or $H_{1/3}$. $H_{1/3}$ corresponds to the wave crest to trough measure of one third the largest waves within the footprint – an important global parameter that can only be approximated. The area, A'_{se}, that includes the contribution of $H_{1/3}$ is again given by *Chelton* et al. (1989) as,

$$A'_{se} = \frac{\pi h(c\tau + 2H_{1/3})}{1 + h/R_e} \tag{3.15}$$

As shown in Fig. 3.6a, the effect of $H_{1/3}$ on the mean return echo is a high leading edge gradient for low sea–state in contrast to that of a low gradient for high sea–state (Fig. 3.6b).

Ultimately, the footprint size effects MSS or gravity anomaly model. At the

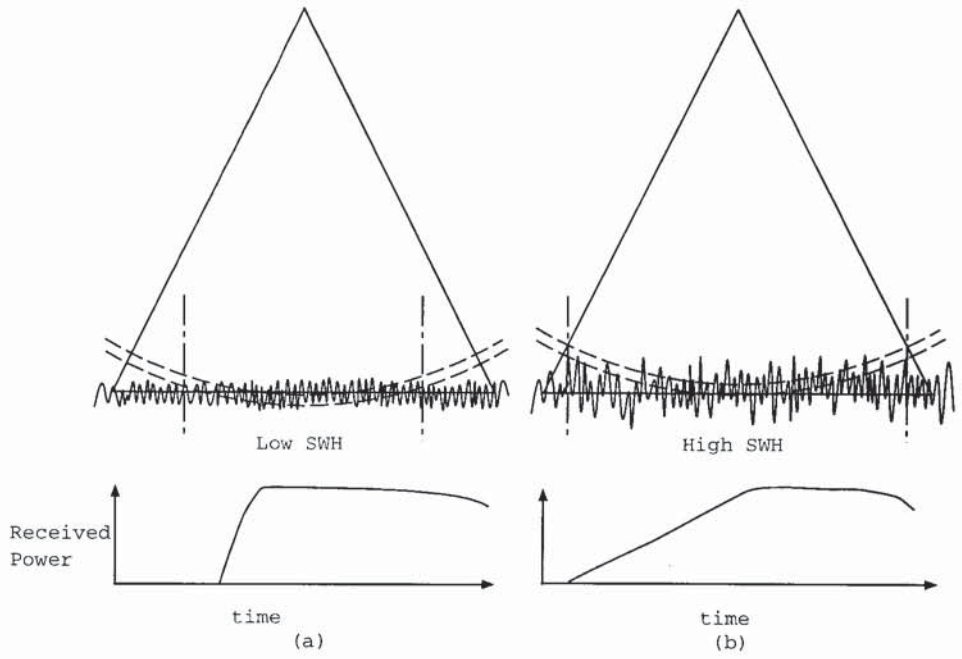

Figure 3.6: Effect on footprint and received waveform for differing surface roughness, (a) a high leading edge gradient for low SWH and (b) low leading edge gradient for high SWH.

highest resolution[2] of 8 km we can see the footprint will exceed this resolution for a great deal of the time. Hence, at the highest frequencies, errors, small as they may be, will exist. In the case of ERS-1 MSS and gravity anomalies presented here, a resolution of ~16 km is obtained. This derives from the ERS-1 geodetic phase equatorial ground–track spacing of ~8 km. At this resolution footprint diameters rarely exceed the limit when errors are aliased.

3.2.4 The Pulse Limited Radar Equation over a Non–Specular Surface

One of the most important aspects governing the design of any radar system is the signal-to-noise ratio (SNR). For the spacebourne radar altimeter the SNR is a function of instrumental noise, antenna gain, frequency, propagation losses and most importantly the radar cross–section (RCS[3]), σ is given by

$$\sigma = \sigma^0 A_s \tag{3.16}$$

[2]Calculated for the GEOSAT geodetic mission ground–track spacing of ~4 km at the equator using the Nyquist sampling theorem

[3]The RCS is a measure of the incident power intercepted by the surface and radiated back to the radar.

where, σ^0, is known the backscatter coefficient and A_s, the physical area illuminated as in equation 3.13 for the pulse limited altimeter. Hence, for differing propagation geometries and surfaces we would expect entirely different values of SNR.

The basic radar altimeter equation for a single pulse, as developed in appendix B.2 for differing geometries and surfaces, is given by

$$\left(\frac{S}{N}\right) = \frac{P_r}{P_n} = \frac{P_t G^2 \sigma \lambda^2 L_p}{64\pi^3 h^4 P_n} \tag{3.17}$$

where,

S/N,	is the signal–to–noise ratio,
P_r,	the received power (watts),
P_n,	is noise power (see appendix B.2),
h,	the height above the surface (m) and
L_p,	is two–way propagation loss.

Propagation loss at microwave frequencies is approximately unity, though this is not the case in the presence of dense clouds or heavy rainfall (*Chelton* et al., 1989). Substituting for σ in equation 3.17 and using the simple area case, $A_s = \pi h c \tau$, the SNR for pulse–limited altimetry is,

$$\left(\frac{S}{N}\right)_{pla} = \frac{P_t G^2 \sigma^0 \lambda^2 c \tau L_p}{64\pi^2 h^3 P_n} \tag{3.18}$$

Substituting typical values for the ERS-1 gives a single pulse SNR of 13.7 dB.

For completeness the radar equation for the beam–limited altimeter is (see appendix B.2 for proof)

$$\left(\frac{S}{N}\right)_{bla} = \frac{P_t G \sigma^0 \lambda^2 L_p}{256 h^2 P_n} \tag{3.19}$$

Also, in the case of a quasi–specular surface such as calm water or newly frozen sea ice the SNR is

$$\left(\frac{S}{N}\right)_{qs} = \frac{P_t G^2 \lambda^2 R_n L_p}{64\pi^2 h^2 P_n} \tag{3.20}$$

Here, R_n is known as a reflection coefficient dependent on the type of ice (first year or multi year) and would have a typical value of -20 dB for first year ice. Hence a typical single pulse SNR would be 53 dB.

Comparing equations 3.18, 3.19 and 3.20 we see that the PLA has an inverse cube law for altimeter height and the antenna gain comes in twice. This compares with the BLA that has an inverse square for height although antenna gain comes in just the once. Over quasi–specular surfaces the height is an inverse square law whilst antenna gain is a square. Hence very high SNR dependent on the type of quasi–specular surface and thus R_n.

It is important to add that within each return waveform there will be a number of random fluctuations due to specular reflections within the ocean surface. This specular noise is reduced by averaging a number of waveforms over a period of time thus improving SNR.

3.2.5 The Brown Model

The mean received echo power modelled by *Moore* and *Williams* (1957) was analysed and brought to a closed form by *Brown* in 1977 and since its publication it has become the standard theoretical model. The paper's central thesis is based on the mean radar echo from a diffuse scattering surface being a threefold convolution namely

$$P_r(t) = S_r(t) * P_{FS}(t) * q(t) \tag{3.21}$$

where,

$P_r(t)$, is the mean received echo, as a function of two–way propagation delay,
$S_r(t)$, is the transmitted pulse shape, and
$q(t)$, is the specular point probability density function describing surface roughness characteristics.

For a flat surface $q(t)$ is a δ–function, otherwise it is adequate to describe a surface comprising of a large number of random scattering elements by a Gaussian function. $P_{FS}(t)$, the average flat surface impulse response, is dependent upon the backscatter coefficient, antenna gain and range to the surface and is given by *Brown* (1977) as,

$$P_{FS}(t) = \frac{\lambda^2}{(4\pi)^3} \iint \frac{\delta(t - \frac{2h}{c}) G^2(\theta) \sigma^0(\Psi)}{h^4} dA \tag{3.22}$$

where, λ is the carrier wavelength, $\delta(t - 2r/c)$ transmitted delta function and the scattering element dA.

The average impulse response may also be determined from the convolution be-

tween $P_{FS}(t)$ and $q(t)$ such that

$$P_s(t) = P_{FS}(t) * q(t) \tag{3.23}$$

Essentially, the Brown model allows the quick analysis of the sea–surface mean return echo and presents a starting point for signal analysis over non–ocean surfaces.

3.2.6 Signal Acquisition, Tracking and Parameter Estimation

In certain circumstances, such as the period following altimeter *switch-on*, it is necessary to

1. locate return waveforms within the range window (signal acquisition).
2. Precisely position the waveform half power point at the assigned tracking gate and maintain this for subsequent return echoes (tracking).
3. Estimate a range of geophysical parameters, not only to validate the signal but also to gather valuable sea surface information.

Each of these properties are now discussed.

Signal acquisition is a procedure required on occasions such as at altimeter switch on and after loss of lock (for example, the altimeter goes over an island and loses track of the signal). When this mode is triggered the altimeter transmits unmodulated pulses with a course height estimate and the tracker estimate is successively reduced until a surface is located. This sequence is intended to be typically achieved within 5 seconds (*Marth* et al., 1993) in the case of TOPEX.

The most important task undertaken by the altimeter is to position the half power point at the tracking gate. This process requires the very precise triggering of the deramping chirp in order to coincide with the receiving of the return signal. Tracking the half power point is achieved by a set of control loops that take information from received waveforms and process subsequent waveforms.

The first of these is known as the Automatic Gain Control (AGC) loop whose primary task is to provide continuous normalisation of received waveforms so analysis can be achieved within the linear response region of the system. Additionally, this value is used as a part of the tracking sub–system itself and also contains information regarding surface backscatter (σ^0) and wind speed. Tracking gate width

is determined by a loop that monitors the leading edge slope (SWH) and lengthens or shortens the width for high and low sea–state respectively allowing range resolution to be maintained.

The system used for determining the error in tracking the half–power point and hence triggering the next de-ramp chirp on–board the ERS altimeters is a highly efficient though complex method of tracking and is known as the Sub–Optimal Maximum Likelihood Estimation (SMLE) tracker. The tracker incorporated in altimeters on–board SEASAT, GEOSAT and TOPEX, although they do vary, is described here for purposes of simplicity and is known as the split–gate tracker.

The triggering time error, Δt_{err} (hence ground processable height error) is determined by computing the difference between the power at the tracking gate, P_{tk}, and the half–power point, P_{agc}

$$P_d = P_{agc} - P_{tk} \tag{3.24}$$

Here, P_{agc} is measured as an average of power over the whole range window, as in the case of SEASAT, or over a large number of range bins, N_{agc}, centered on the tracking gate, m as for TOPEX and GEOSAT. Here,

$$P_{agc} = \frac{1}{N_g} \sum_{n=m-N_{agc}/2}^{m+N_{agc}/2} P_n \tag{3.25}$$

where, P_n represents the power in the n^{th} bin and N_g is a normalisation factor.

In order to minimise Raleigh induced noise, P_{tk} is determined as an average power over a small number of gates, k, so

$$P_{tk} = \frac{1}{2k+1} \sum_{n=m-k}^{m+k} P_n \tag{3.26}$$

where, k, is used to determine the width of the tracking gate. Δt_{err} is finally calculated (*Chelton* et al., 1989) as a function of chirp bandwidth, ΔC, compressed pulse length, τ, power difference, P_d, antenna mispointing, a and b proportional to $H_{1/3}$. This is given by,

$$\Delta t_{err} = \frac{a + bP_d}{\Delta C} \tag{3.27}$$

and height error, ΔH_{err} is simply

$$\Delta H_{err} = c\Delta t_{err} \tag{3.28}$$

Estimates of de–ramp chirp triggering errors, Δt_{err}, are required to be noise free both for split–gate trackers and even more so for SMLE trackers. Otherwise, aliasing of errors are translated into sea height observations. Reducing noise may be accomplished using a smoothing procedure such as the second–order α–β filter (*Kingsley* and *Quegan*, 1992).

As a final point is should be noted that for high inclination altimeters, such as the ERS satellites, valuable data may be lost over the high latitudes due to the existence of newly formed thin pancake or grease sea–ice. These types of ice have been shown to still reflect marine geoidal information but tend to cause a loss of track of up to several meters. It is possible to employ a re–tracking algorithm (described by *Laxon* (1994)) from individual waveforms in order to correct the height and reduce data loss.

3.2.7 Other Design Considerations

1. There will be always be some radial velocity in the satellite, $\mathbf{v_r}$ that can be as large as 30 ms^{-1} generating a Doppler shift in transmitted pulses. This effect manifests itself as errors in the frequency domain that results in a height error, Δh_{dopp}. This can be corrected during ground processing (See section 4.6). This error is given by *Chelton* et al. (1989) as a function of $\mathbf{v_r}$, frequency, f and chirp rate, ΔC, i.e.,

$$\Delta h_{dopp} = \frac{f\mathbf{v_r}}{\Delta C} \tag{3.29}$$

2. In early spacebourne radar altimeter designs the transmit power was large ($\sim$ 2kW) for use within noisy Travelling Wave Tube (TWT) amplifiers. It was shown that such high powers limited the lifetime of the amplifiers to a few thousand hours; in fact SEASAT failed exactly for this reason (*Chelton* et al., 1989). The Power was subsequently reduced to $\sim$ 20W and with the introduction of the Solid State amplifier signal powers of $\sim$ 2W can be achieved. Longer altimeter lifetimes are now becoming common.

3. The various spacecraft electronic subsystems are subject to thermal fluctuations. One of the long–term effects of this has been to generate a drift within

the ultra stable oscillator which can be corrected during ground processing.

4. Finally, after altimeter switch on bias jumps occur. This effect is attributed to instrument temperature change during periods of altimeter switch off. These again may be removed at a processing stage.

3.2.8 Summary of Measureable Parameters

In summary, the parameter that may be inferred from the return signal are as follows.

1. σ^0, the backscatter coefficient derived from the AGC gives a measure of specular power returned from the surface. Over ocean this is linked to surface roughness and is therefore linked to sea–surface wind. Over land σ^0 may give a measure of the type of vegetation, whilst over sea ice the type of ice, i.e., first year grease ice or multi–year ice may be determined.

2. $H_{1/3}$, the Significant Wave Height determined from the slope of the echo waveform tells us a great deal about global wave heights characteristics.

3.3 Future Developments in Radar Altimetry

The SRA has remained remarkably similar in design over the past 25 years with hardware upgrade reflecting technological trends. Thus higher sampling rates and better processing techniques are resulting in a range of improvements such as range resolution and the sophistication of on–board tracking.

The incorporation of the Solid State amplifier into the instrument has provided the advantages of low power/mass and giving good SNR with longer term stability. Currently only one prototype instrument exists (Poseidon) although they will probably become the norm within the next decade.

As will be shown in section 4.4.2, the dual frequency altimeter allows for a vastly improved ionospheric correction. However, one argument against the use of this system is based on the need for extra power and mass requirement. The use of Solid State technology effectively undermines this argument.

Finally we require the generation of a high spatial resolution mean sea surface that is ultimately limited due to the PLA footprint size (section 3.2.3). A method described by *Elachi* (1988) and investigated theoretically by *Griffiths* (1988) attempts a solution to this problem via treating the altimeter echoes in a similar method to the Synthetic Aperture Radar (SAR), i.e., taking pulse time and phase

history in order to develop a pseudo–antenna length of such a size that the footprint size decreases. Such a method would give an along–track footprint size of, d, of

$$d = (h\lambda)^{1/2} \tag{3.30}$$

So for the ERS this would give a footprint size of 130 meters. Unfortunately cross–track resolution is left unaffected and as *Elachi* explains, a scanning technology would be required to allow cross-track resolution improvement.

Parameter	S-193 USA	GEOS-3 USA	SEASAT USA	GEOSAT USA	ERS-1(2) ESA	TOPEX USA	Poseidon FRANCE	GFO USA	ENVISAT ESA
Primary Source	1	2	3	4	5	6	7	8	9
Year of mission	1973	1975	1978	1985	1991(5)	1992	1992	1997	1999
Mission lifetime (yrs)	10mnth	$3\frac{1}{2}$	3mnth	$4\frac{3}{4}$	$4\frac{1}{2}(3)$	5	5	3	5
Repeat cycle (days)	—	∞	3/17	$\sim$23/17	3/35/168(35)	10	10	17	35
Inclination (°)	50	65.1	108	108	98.5	66	66	108	98.55
Mean orbit height (km)	435	840	800	800	790	1334	1334	800	799.8
Range precision (cm)	< 100	50	10	10	10	2.5	< 10	3.5	< 4.5
Carrier Frequency (GHz)	13.9	13.9	13.5	13.5	13.8	13.6/5.3	13.65	13.5	13.575/3.2
Uncompressed pulsewidth (μS)	—	—	3.2	3.2	20	102	100	—	20
Compressed pulsewidth (nS)	100	12.5	3.125	3.125	3.03	3.125	3.03	—	2.0
PRF (Hz)	—	100	1020	1020	1020	4272/1012	1700	—	1795/449
Bandwidth (MHz)	10	80	320	320	330	320	330	—	320
Antenna diameter (m)	—	—	—	—	1.2	1.5	1.5	—	1.2
3–dB Beam–width (°)	1.5	2.6	1.6	2.1	1.3	1.1/2.7	1.46	—	1.3
Transmit Power (W)	2000	2000	2000	20	55	20/20	2	121	161
Amplifier	TWT	TWT	TWT	TWT	TWT	TWT	SS	TWT	TWT/SS

Table 3.1: Spaceborne RA characteristics for a sample of past and future missions (Other missions include JASON-1, GFO-2). Information collected from primary sources: 1. *McGoogan* et al. (1974), 2. *McGoogan* (1975), 3. and 4. *Davis* (1992), 5. *Vass* and *Battrick* (1992), 6. *Marth* et al. (1993), 7. *Griffifths* (1994), 8. *Finkelstein* (1997), 9. *ESA* (1997).

Chapter 4

Radar Altimetry Correction Schemes

4.1 Introduction

Our main requirement is the accurate measurement of instantaneous sea-surface height, $h_s(\phi, \lambda, t)$, above a best fitting reference ellipsoid, $h_{ref}(\phi, \lambda)$, from the observed altimeter height, $h_{alt}(\phi, \lambda, t)$. Thus h_s is given by

$$h_s = h_{alt} - h_{ref}. \tag{4.1}$$

Unfortunately h_s is subject to a wide range of errors broadly categorised as radial orbit error, tidal phenomena, environmental media delay, sea–surface effects and telemetered instrumental errors. Most of these can be effectively removed. However, in a few cases our understanding of the physical phenomena causing them is inadequate. Thus there is a need for significant improvement in some corrections.

The corrected sea surface height, h_{ssh} is given by

$$h_{ssh} = h_s + \Delta h_{roe} + \Delta h_{tide} + \Delta h_{env} + \Delta h_{ss} + \Delta h_{inst} \tag{4.2}$$

where the height corrections are,

Δh_{roe}, are for radial orbit error,
Δh_{tide}, tidal corrections,
Δh_{env}, environmental path length,
Δh_{ss}, sea-surface effect, and
Δh_{inst}, finally instrumental effects.

Each of the above error sources are now described in detail. A list of contemporary methods of correction are shown in Table 4.1.

Correction Parameter	Methods of correction	Source
Radial orbit error	Spline Fit	*Le Traon* et al. (1995)
via Crossover adjustment		See Section 6.3
	Sinusoidal fit	*Tai* (1988),
		Jolly and *Moore* (1996)
via long–wavelength removal	Along-track slopes	*Sandwell* (1984)
Solid Earth Tide	Cartwright–Ray	*Cartwright* and *Ray* (1991)
Ocean Tide	CSR3.0	*Eanes* and *Bettadpur* (1995)
	FES95.2.1	*Le Provost* et al. (1994)
Ocean Loading Tide	CSR3.0	*Eanes* and *Bettadpur* (1995)
	FES95.2.1	*Le Provost* et al. (1994)
Pole Tide	Algorithm	*Wahr* (1985)
Wet Troposphere	Microwave Radiometer	*Eymard* et al. (1994)
	ECMWF Model	*Eymard* et al. (1994)
Dry Troposphere	Pressure Model	*Eymard* et al. (1994)
Ionosphere	Bent	*Bent* et al. (1975)
	IRI95	*Bilitza* et al. (1995)
	Klobuchar	*Klobuchar* (1987)
	Dual frequency	*Monaldo* (1993)
Sea-State Bias	Fraction of SWH	*Carnochan* (1997),
		Gaspar et al. (1994)
	Wave history model	*Glazmann* et al. (1994)
Inverse Barometric	Local Pressure Model	*Zlotnicki* (1994)
	Global Pressure Model	*Ponte* et al. (1991),
		Cheney (1997b)
USO drift	Drift Model	Published on WWW
Bias Jumps		Published on WWW
Doppler	See equation 3.29	*Chelton* et al. (1989)

Table 4.1: A list of correction methods for each of the contributing error sources.

4.2 Radial Orbit Error

Until recently, the largest source of signal error being aliased into an altimetric measurement was the incorrect computation of a satellites' radial position above a reference ellipsoid for any given epoch. This, the radial orbit error, has a charac-

teristically large error at once per orbital revolution and over a large range of other frequencies. In order to show how this error may be effectively removed it is important to briefly acknowledge what is required to calculate a satellite's ephemeris and therefore appreciate how errors are generated.

To begin with, independent observations of the satellite's position are required. These come in the form of

1. Range tracking measurements from Precise Range and Range–rate Equipment (PRARE) on–board ERS-2[1] or Satellite Laser Ranging (SLR). The former relies on *visible* stations relaying microwave signals originating from the PRARE instrument back to it. And in the latter case the opposite occurs with laser retro–reflectors being mounted on the satellite.

2. Range–rate observations from instruments such as DORIS (Doppler Orbitography and Radiopositioning Integrated by Satellite) and again PRARE.

DORIS has proved to be a reliable means of tracking with atmospheric effects having been solved for and enough stations being available for a good global coverage. Both SLR and PRARE, however, are still susceptible to atmospheric effects and with too few stations unevenly spread global coverage of the satellite has proved to be inadequate. Altimetry and Dual satellite crossover residuals (described in section 6.3) may be included to assist tracking data.

Precise orbit determination software uses weighted observation data and, via the use of initial state vectors, builds an ephemeral step–by–step positioning of the satellites motion. A major requirement is the need to model all forces incident on the platform. The major forces come in the form of gravitation, Luni–Solar tides and atmospheric/solar drag. Of these, gravity field mis–modelling provides the main error source. However, vast improvements in gravity modelling have provided a reduction of orbit error from meters in the 1970's down to what is now of the order of centimetres.

To date the altimetric satellite with the most accurately defined ephemeris is TOPEX/Poseidon, combining SLR and DORIS tracking in addition to the on–board GPS (Global Positioning System) equipment. With the advantage of an orbital mean altitude of 1334 km, where atmospheric drag and gravity is significantly reduced, orbital accuracies are reported as low as 2 cm RMS (see *Le Traon* and *Ogor*, 1998).

[1]PRARE failed on ERS-1 due to a design flaw.

For the purpose of studies carried out within this thesis, ERS-1 carried SLR and PRARE (Precise Range and Range–rate Equipment) tracking capability. However the combination of PRARE failure shortly after launch combined with the relatively low mean orbital height of 794 km has resulted in orbits that require further processing.

There are two methods explored within this thesis; the first utilises the method of using T/P with very precise orbits as a reference and using crossover theory to essentially remove the error. This methodology is described in great detail in chapter 6. Another method of reducing long–wavelength radial orbit error to below the instrumental noise floor is achieved via the computation of along–track slopes. This procedure, however, attenuates all long wavelength signal whilst amplifying the medium to short–wavelengths and therefore, unfortunately, high frequency noise. Also, along–track slopes are of little use if it is the sea–surface heights that are to be analysed. This technique has its obvious advantages in the analysis of short wavelength sea–surface features.

4.3 Tidal Modelling

There are four main tidal components to be taken into account, cover and correct for the majority effect on the sea–surface. These are; 1. Solid–Earth tide, Δh_{se}, 2. Ocean tide, Δh_{ot}, 3. Ocean Loading tide, Δh_{olt} and 4. Polar tide, Δh_{pt}. The expansion of Δh_{tides} within equation 4.2 giving

$$\Delta h_{tides} = \Delta h_{se} + \Delta h_{ot} + \Delta h_{olt} + \Delta h_{pt}. \tag{4.3}$$

Methods of determining the tidal components originally came from analysis of data from tide gauges. However, with the advent of the SRA and attention being paid to orbit choice it is now possible to use altimetry to make significant improvement to such tidal models (described in detail in *Parke* et al., 1987). For example, the T/P orbit characteristics were particularly chosen to avoid aliasing of all major tidal constituents and hence is a useful instrument for their analysis. However sun-synchronous satellites such as ERS alias errors within the solar tides and with the 35 day repeat cycle aliasing will also occur with the lunar tides. The ERS-1 was placed in this orbit in order that the Along–Track Scanning Radiometer (ATSR) could sample sea–surface temperatures at the same local time via fixing the local time at the descending node to 10:30am.

4.3.1 Solid Earth Tide

The Solid Earth Tide with an amplitude of ~20 cm results from the gravitational forcing from the Sun and Moon. The contemporary model to use is the Cartwright–Ray model *Cartwright* and *Ray* (1991).

4.3.2 Ocean Tide

The gravitational attraction of the Sun and Moon on the oceans mainly causes the generation of this tide with an amplitude of around a metre. Complications occur in analysing this tide due to resonances within ocean basins and due to the ellipticities of the Earth and Lunar orbits. Also over continental shelves large uncertainties occur hence local models are generally preferred. Typical models are the U.S. CSR3.0, *Eanes* and *Bettadpur* (1995) or the French FES(95.2.1), *Le Provost* et al. (1994). Such representations of the major constituents are now well modelled over the oceans, thanks mainly to TOPEX, however some long–period tides are not well known. The former of these, incidentally, contains model discrepancies at two frequencies centred approximately close to 60 days. This is due to the 10 day T/P repeat cycle that aliases a proportion of the semi–diurnal tides, *Wunsch* and *Stammer* (1995).

4.3.3 Ocean Loading Tide

This tide exists as a result of the mass of water within the oceans effectively compressing the Earth's crust. The effect may be modelled as a percentage (~7%) of the Ocean tide itself. This gives rise to a correction generally below 7 cm. Data products will sometimes provide a merging of the Ocean and Ocean loading tides known as the Elastic Ocean Tide.

4.3.4 Pole Tide

The geocentric Polar motion tide (see *Wahr*, 1985) has component periods ranging between mainly 12 and 14 months and has an amplitude less than 2 cm.

4.4 Environmental Corrections

Molecular and electronic constituents within the atmosphere can cause variations in refractivity. Thus pulses are slowed and attenuated leading to propagation errors in need of correction. Such *environmental* errors can be specifically attributed to

the dry/wet components of the troposphere and the ionosphere. Equation 4.2 is expanded to give

$$\Delta h_{env} = \Delta h_{dt} + \Delta h_{wt} + \Delta h_{iono} \tag{4.4}$$

where, corrections are for the dry troposphere Δh_{dt}, wet troposphere Δh_{wt} troposphere and Δh_{iono} the ionosphere.

4.4.1 Tropospheric Corrections

For frequencies up to 100 GHz the total tropospheric correction, Δh_t, are calculated by integrating electromagnetic wave refractivity (see *Bean* and *Dutton*, 1966) throughout the troposphere of height, z_t given by

$$\Delta h_t = \int_0^{z_t} (N(z) \times 10^{-6}) dz \text{ meters} \tag{4.5}$$

where, $N(z)$ is the refractivity as a function of height z. N is then approximated by the following empirical expression

$$N = \frac{K_1 P_d(z)}{T(z)} + \frac{K_2 e(z)}{T(z)} + \frac{K_3 e(z)}{T^2(z)} \tag{4.6}$$

where,

$P_d(z)$, is the dry partial pressure in millibars,
$e(z)$, the water vapour pressure and
$T(z)$, is the temperature in Kelvin (K).

K_1, K_2 and K_3 may be empirically determined.

The separate wet and dry corrections are determined by splitting equation 4.6 into two parts representing dry and wet pressure components respectively. Substituting the first component on the RHS of equation 4.6 into equation 4.5 gives Δh_{dt} such that

$$\Delta h_{dt} = K_1 \times 10^{-6} \int_0^{z_t} \frac{P(z)}{T(z)} dz. \tag{4.7}$$

Alternatively, an empirical version of equation 4.7 may be used (described in *Cudlip* et al., 1994) that requires only surface pressure, P_0 and latitude, ϕ such that

$$\Delta h_{dt} = -2.227 P_0 (1 + 0.0026 \cos 2\phi) \quad \text{mm.} \tag{4.8}$$

Values of surface pressure may be obtained from a model derived at the European Centre for Medium–term Weather Forcasting (ECMWF) on a $0.5° \times 0.5°$ grid updated at 6 hourly intervals. Equation 4.8 remains fairly constant varying between 2.05 and 2.32 m for a corresponding surface pressure range of 900 and 1020 mb.

Similarly, Δh_{wt}, is obtained via the substitution of water vapour pressure components, e, of equation 4.6 into equation 4.5 giving

$$\Delta h_{wt} = K_2 \times 10^{-6} \int_0^{z_t} \frac{e(z)}{T(z)} dz + K_3 \times 10^{-6} \int_0^{z_t} \frac{e(z)}{T^2(z)} dz \tag{4.9}$$

This wet range correction may also be modelled empirically giving

$$\Delta h_{wt} = -Q \left(2.584 \times 10^{-5} + 5.324 \times 10^{-2} \ln \left(1 - \frac{32.5}{T_0} \right) \right) \quad \text{meters} \tag{4.10}$$

here, Q and T_0 are total integrated water content and surface temperature respectively. They are obtained from either a microwave radiometer or model and give typical corrections ranging between 0 and 40 cm. For the Centre ERS d'Archivage et de Traitement (CERSAT) releases of data products for the ERS satellites, h_{wt} is given directly from an algorithm developed by *Eymard* et al. (1994). This relationship requires only the brightness temperature measured from the 23.8 GHz, T_{24}, and the 36.5 GHz, T_{36}, of the microwave sounder (ATSR-M) channels giving

$$\Delta h_{wt} = 209.64 - 74.74 \ln(280 - T_{24}) - 33.98 \ln(280 - T_{36}). \tag{4.11}$$

Microwave radiometers are used on all current altimeter missions such as the ATSR-M on–board the ERS missions *Eymard* et al. (1994). On missions such as GEOSAT, where no radiometer was available it was necessary to either use radiometry data from instruments on–board other dedicated satellites in orbit over the same period; such as TIROS Operational Vertical Sounder (TOVS) and Special Sensor Microwave Imager (SSMI) or via the use of models. Original GEOSAT data products contained highly inaccurate values ($\sim$15 cm RMS over equatorial regions) from the U.S. Fleet Numerical Ocean Model (FNOC), *Cheney* et al. (1991). However, the latest enhanced GEOSAT data release (*Cheney*, 1997b) contains a

re–analysis of water vapour data from NASA Water Vapour Project (NVAP) and National Centers for Environmental Prediction (NCEP) with the latter combining radiometry and model data.

4.4.2 Ionospheric Refraction

The ionosphere is a highly variable medium residing approximately between 50 and 2000 km above the Earth's surface with maximum electron densities of 2 to 5×10^{12} electrons m^{-3}. There are strong variations on a diurnal, seasonal and solar cycle basis with a latitudinal trend.

Free electrons resident within the ionosphere cause refraction and hence path delays with height errors between 5 and 25 cm *Rush* (1986). Ionospheric models have been developed from ionosonde and Faraday rotation experiments such as the Bent (*Bent* et al., 1975) and IRI95 models (*Bilitza* et al., 1995).

For the single frequency altimeter the use of such models is necessary to measure the ionosphere height correction, Δh_{iono}. Following *Lawrence* (1964) this integrated ionospheric effect requires a correction given by

$$\Delta h_{iono} = \frac{A}{f^2} \int_0^{h_{alt}} N_o(z) dz = \frac{AT}{f^2} \text{ m} \tag{4.12}$$

where,

- T, is the Total Electron Content (TEC) obtainable from a model,
- A, an empirically determined constant equal to 40.3 $m^3 e^{-1} s^{-2}$,
- f, the frequency in Hertz, and
- N_0, the electron density as a function of vertical displacement, z.

It can be seen from equation 4.12 that the correction is a function of frequency. Following *Monaldo* (1993), if a radar transmits at two carrier frequencies, f_1 and f_2, then the need to calculate a correction from model TEC values becomes redundant. Here, Δh_{iono} may be determined by the height measurements, h_1 and h_2, in addition to the two carrier frequency values. Thus,

$$\Delta h_{iono} = \frac{f_1^2 h_1 - f_2^2 h_2}{f_1^2 - f_2^2}. \tag{4.13}$$

For the dual–frequency altimeter such as TOPEX it is possible to make highly accurate corrections. *Schreiner* et al. (1997), quotes TEC accuracies of $200 \pm 4 \times 10^{16}$ electrons for the Ku and C–band channels. Even under extreme solar conditions,

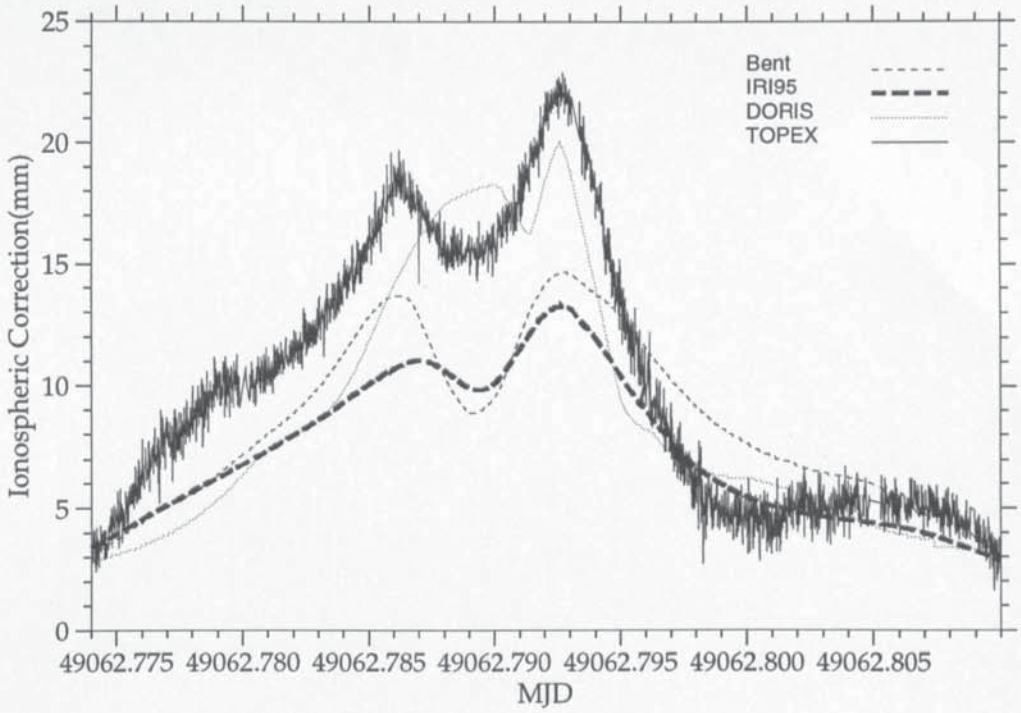

Figure 4.1: Ionospheric correction for Dual-frequency, DORIS and Bent/IRI95 models during a period of extreme ionospheric activity during MJD 49062 (16th March 1993).

such as those shown in Fig. 4.1, we see that the dual frequency DORIS tracking system also allows reasonable correction. However the two ionospheric models display errors as large as 9 cm in places. This illustrates the need for the on–going model review and update. In fact it is most likely that the use of TOPEX derived ionospheric corrections may help improve such models.

The future use of such models in correction schemes, however, is limited as data entry into the EOS–MTPE programme (*Asrar* and *Greenstone*, 1995) requires that only dual–frequency altimeters be incorporated. Following the discussion in section 3.3, any argument concerning increased instrument mass/power requirements for a dual frequency altimeter will be dispelled with low mass Solid State technology.

4.5 Sea–Surface Effects

There are two sea–surface corrections described here, namely the inverted barometric effect, Δh_{ib} and sea-state bias, Δh_{ssb}. Equation 4.2 can be expanded for

Δh_{ss}, taking these into account, i.e.,

$$\Delta h_{ss} = \Delta h_{ib} + h_{ssb} \tag{4.14}$$

4.5.1 Inverted Barometric Effect

The Inverted Barometer (IB) effect is a complex phenomenon. Fluctuations in sea–level pressure cause the generation of geostrophic currents leading to sea–level change over a period of 2 days to 2 weeks following the event (*Wunsch*, 1972). The traditional model used to counter this effect (see *Gill* and *Niiler*, 1973) takes into account the localised pressure that results in either an inflation or deflation of the sea–level. This is dependent on whether surface pressure is less than or greater than a global average. The associated height correction is given by,

$$\Delta h_{ib} = -\frac{1}{\rho g}(P_0 - \bar{P}_0) \tag{4.15}$$

where,

$\rho \approx 1.025$ g/cm^3,	is the density of sea water,
$g \approx 981$ cms^{-2},	is the acceleration due to gravity,
P_0,	is the atmospheric pressure (mb), and,
$\bar{P}_0 \approx 1013.3$ mb,	represents the average atmospheric pressure.

Zlotnicki (1994) suggests since P_0 can only be determined to 3 mb, thus a correction error between 3 and 5 cm is evident. In addition, following *Ponte* et al. (1991) it is becoming custom to take into account the globally averaged IB effect such as in the enhanced release of GEOSAT data (*Cheney*, 1997b).

4.5.2 Sea–State Bias

Electromagnetic, or more commonly sea–state bias, is a phenomenon under on–going debate as to exactly how it is manifested and, in particular, the most apt method for it to be dealt with. Contemporary thinking suggests that there is a two–way process at work. In the first instance, sea–surface waves scatter more pulse energy from wave troughs than crests. Secondly, scattered energy at the tracking stage are fitted with a model, such as the Brown model described in section 3.2.5, that assumes the sea–surface is Gaussian and thus tracks the median of these specular points rather than the actual mean sea surface. This leads to a

bias error.

The simplest, though least effective, method of correcting for sea–state bias is to take a percentage, m, of the SWH, $H_{1/3}$, such that,

$$\Delta h_{ssb} = mH_{1/3} \text{ meters.} \tag{4.16}$$

Separate studies by *Carnochan* (1997) and *Gaspar* et al. (1994) give values of 5.95% and 5.5% respectively. It has been suggested by *Tokmakian* et al. (1994) that this method underestimates, by as much as $m = 2\%$, the effect in areas of swell. Alternatively, over estimating occurs in wind–wave dominated seas, hence, this method is deemed unacceptable.

Ultimately, the process is far more complex and a number of alternatives to equation 4.16, reviewed by *Glazmann* et al. (1994), are available. These take into account such physical phenomena as wave–age, gravity wave turbulence and wind fetch.

4.6 Instrumental System Errors

In addition to the range of errors concerning the orbit, tidal systems, environment and sea-surface there are also a set of contributions that emanate from the instrument itself. These are described here (in addition to chapter 3) since they are accounted for at the ground processing or post–processing stage.

Instrumental corrections cover

1. USO drift occuring over a relatively long period of time due to continuous thermal changes within the electronic sub–system. The effect can be modelled, as in the case of GEOSAT, or measured via the use of independent USO systems maintained in a more suitable environment. Incorrect modelling of this effect for TOPEX caused inaccurate reporting of sea–level rise of 3.9 ± 1.8 mm per year by *Nerem* (1995) that was later retracted in February 1997 (*Nerem*, 1997) following the discovery and subsequent publication of the problem.

2. Bias Jumps are sudden changes in telemetered height output levels as a result of altimeter switch–on that are monitored and distributed to the scientific community for post–processing over the internet.

3. Doppler shift errors, as described in section 3.2.7, are corrected for in ground processing. A typical Doppler shift of 30 ms^{-1} can translate to an error

of ~ 2.5 cm for the ERS satellites (Values calculated from Table 3.1 and equation 3.29.)

4. The Centre–of–gravity (COG) offset is a correction applied to reference all measurements to adjust the satellites height from plane of the antenna aperture to the COG referenced by all other instruments.

5. Frequency Modulation Crosstalk is simply the interference between transmission and receiver stages within the RA which may easily be removed.

6. Skewness bias is caused by antenna mis-alignment with a contribution from SWH.

4.7 Final Considerations

In this chapter we have seen how many corrections are used to adjust the raw RA height. Some of these are relatively accurate as they are supplied from other instruments or as our understanding of the phenomena are complete. However, some model corrections are poorly understood and require further analysis in the future. Here, the prime candidates are sea–state bias, localised inverted barometer effect and model derived ionospheric effect. Radial orbit error is now reducing to an acceptable level which with GEOSAT Follow–on and JASON-1 should reduce to the 1–2 cm level, close to the accuracy of the tracking data.

Chapter 5

Fourier Domain Processing of the Gravity Field

In this chapter the geodetic theory relating to the modelling of the geoid and gravity anomaly field is explored via the use of fast Fourier transform (FFT) techniques. This is achieved by first of all reviewing FFT properties and introducing the procedures necessary for spectral MSS optimal interpolation in chapter 6. In addition the Stokes and Vening–Meinesz boundary value problems are solved. This forms the basis for developing the global gravity anomaly field in chapter 7 and its subsequent transformation to a mean sea surface for model integration in chapter 8.

5.1 The Fourier Transform

The Fourier transform is a vital analytical tool for signal processing (*Bracewell*, 1978). Despite a number of shortfalls it has been shown to be very efficient in terms of the numerical processing of noisy and non uniform data. However most importantly it can deal very simply with least squares minimisation in a relatively short computational time in comparison to other spatial counterparts. Thus it may be used to alleviate some of the more complex problems in physical geodesy. In particular its use in the solution of a number of gravity field recovery procedures has now become well documented (see *Nash* and *Jordan* (1978), *Schwarz* et al. (1990), *Sandwell* (1992), *McAdoo* and *Marks* (1992) and *Hwang* and *Parsons* (1996), *Andersen* and *Knudsen* (1998) for example.) However very few methodologies have been developed for MSS studies. *Jolly* (1995) for example, made an attempt for a single 35 day cycle of ERS-1 data, though results were not that encouraging. Here, we will take an alternative approach though in principle there are

similarities. These will be discussed further in chapter 6.

The continuous forward Fourier transform is described in a number of publications including *Bracewell* (1978), *Sideris* and *Tziavos* (1988) and *Schwarz* et al. (1990). In studies described here we deal analytically with transforms in one to three dimensions. However, computationally we only require one and two dimensions; as will become evident with final solutions. In vector form the three dimensional continuous Fourier transform is given by

$$F(\mathbf{u}) = \mathcal{F}[f(\mathbf{x})] = \iiint_{-\infty}^{\infty} f(\mathbf{x}) e^{-\imath 2\pi(\mathbf{u}\cdot\mathbf{x})} d\mathbf{x} \tag{5.1}$$

where, $\imath = \sqrt{-1}$ is the imaginary unit. $\mathbf{u}$ and $\mathbf{x}$ are

$$\mathbf{u} = u\hat{\mathbf{i}} + v\hat{\mathbf{j}} + w\hat{\mathbf{k}} \quad \text{and}$$

$$\mathbf{x} = x\hat{\mathbf{i}} + y\hat{\mathbf{j}} + z\hat{\mathbf{k}} \quad \text{respectively.}$$

u, v and w are spatial frequencies measured in cycles per unit distance (or degree) corresponding to the coordinates x, y and z respectively and $\mathcal{F}$ is known as the Fourier operator. Likewise the inverse transform may be determined such that

$$f(\mathbf{x}) = \mathcal{F}^{-1}[F(\mathbf{u})] = \iiint_{-\infty}^{\infty} F(\mathbf{u}) e^{\imath 2\pi(\mathbf{u}\cdot\mathbf{x})} d\mathbf{u}. \tag{5.2}$$

The two–way transformation may now be represented by

$$f(x, y, z) \Longleftrightarrow F(u, v, w) \tag{5.3}$$

Since we will be dealing with discrete gridded data it is necessary to use an alternative methodology known as the discrete Fourier transform (DFT). The fast Fourier transform (FFT) algorithm is then used to compute the DFT at speed. The discrete form assumes data is on a regular grid at intervals, Δx, Δy and Δz corresponding to discrete frequencies Δu, Δv and Δz. Each dimension also contains element lengths, L, M and N in the x, y and z directions. Physical record lengths X, Y and Z are given by

$$X = \Delta x L = 1/\Delta u; \quad Y = \Delta y M = 1/\Delta v; \quad Z = \Delta z N = 1/\Delta w. \tag{5.4}$$

So if a gridded function, $f(x, y, z)$ is available then its forward three dimensional

DFT (see *Vassiliou* and *Schwarz*, 1987, for example) is given by

$$F(l\Delta u, m\Delta v, n\Delta w) = \Delta x \Delta y \Delta w \sum_{i=0}^{L-1} \sum_{k=0}^{M-1} \sum_{l=0}^{N-1} f(i\Delta x, j\Delta y, k\Delta z) e^{-\imath 2\pi(\frac{li}{L}+\frac{mj}{M}+\frac{nk}{N})}$$
$$l = 0, 1, \ldots, L-1,$$
$$m = 0, 1, \ldots, M-1, \quad \text{and}$$
$$n = 0, 1, \ldots, N-1 \tag{5.5}$$

where, Δu, Δv and Δw are discrete spatial frequencies. The inverse DFT allowing conversion of a signal in the frequency domain to its spatial or temporal counterpart is given by

$$f(i\Delta x, j\Delta y, k\Delta z) = \Delta u \Delta v \Delta w \sum_{l=0}^{L-1} \sum_{m=0}^{M-1} \sum_{n=0}^{N-1} F(l\Delta u, m\Delta v, n\Delta w) e^{\imath 2\pi(\frac{li}{L}+\frac{mj}{M}+\frac{nk}{N})}$$
$$i = 0, 1, \ldots, L-1,$$
$$j = 0, 1, \ldots, M-1 \quad \text{and}$$
$$k = 0, 1, \ldots, N-1. \tag{5.6}$$

Since data is discrete, it falls under the conditions of the Nyquist sampling theorem. This theorem determines the minimum sampling period necessary to allow all frequency components to be resolved. Failure to maintain this sampling period causes high frequencies to be aliased into lower frequency signals and vice–versa. This is also known as a frequency wrap around effect (see *Bracewell*, 1978). Therefore the highest spatial frequencies, u_{nq}, v_{nq} and w_{nq}, that can be resolved are $u_{nq} = 1/2\Delta x$, $v_{nq} = 1/2\Delta y$ and $w_{nq} = 1/2\Delta z$ respectively.

The DFT is an efficient means of estimating the frequency spectrum of any given sampled signal. However computational speed may be vastly improved via the use of a FFT of which there are a number of algorithms. The Cooley & Tuckey algorithm (*Cooley* and *Tukey*, 1967) was the first developed for data sets containing a power of 2 number of elements. The method used here is the general–radix Singleton algorithm that allows grid sizes of any number of elements (*Singleton*, 1967).

We now refer to the FFT with transformations expressed by the relationship $f(x, y, z) \Longleftrightarrow F(u, v, z)$.

In addition to the Nyquist phenomenon, the FFT is subject to a number of other

shortfalls, namely;

1. Gridded data is required to be complete. If this is not the case then discontinuities may exist resulting in the effect known as Gibbs' or ringing phenomenon occurring. In the extreme, large discontinuities cause large spatial gradients. This would require an unfeasibly large number of frequency components that the FFT cannot provide since data is discrete and of finite length. Data gaps are therefore required to be filled with either a model or an interpolated value. If boundaries are naturally smooth then the discontinuity is minor and the effect diminished.

2. Data is assumed to be periodic; this is rarely the case. In the analysis of signals on the Earth longitude is periodic as opposed to latitude that is aperiodic. Here we essentially have the same problem as in the above point in the sense that discontinuities occur at the grid extremes. Once again the finite data sequence length is unable to cope with the discontinuity and side-lobes are generated in the frequency domain. To alleviate this problem a process known as windowing is adopted. Here data at the latitudinal extremes of the grid are smoothed, or weighted, in order to convert the discontinuity into a smooth slope. Typically a cosine function is used but as a result there is an irrecoverable loss of signal. In regional studies all edges are required to be windowed. The method of windowing used in this thesis is the Hanning window.

Other transforms exist such as the Hankel transform (see *Bracewell*, 1978, for example) for circular functions and the Wavelet transform (*Foufoula-Giorgiou* and *Kumar*, 1994) for the analysis of signals on a wide range of spatial scales. Where these methods, especially in the later case, are relatively new to this subject, the FFT is not and has a solid background in physical geodesy. However, other transforms will inevitably become more widely used in this particular field.

5.1.1 FFT Spectral Properties

There are a number of properties relevant to theory in this chapter. These are

1. The linearity relationship

$$af(x,y) \Longleftrightarrow aF(u,v) \tag{5.7}$$

where, a is a constant.

2. The Fourier transform derivative. For example, the derivative of the function $f(x, y)$ with respect to x is

$$\frac{\partial f(x,y)}{\partial x} \Longleftrightarrow \imath 2\pi u F(u,v). \tag{5.8}$$

It can be seen that the spatial differential is essentially the multiplication by frequency in the spectral domain. Thus higher frequencies are amplified relative to lower frequency counterparts. Also at zero frequency, $u = 0$, the function is set to zero resulting in a zero signal bias in the spatial domain. For completeness, the nth derivatives w.r.t. x and y are

$$\frac{\partial^n f(x,y)}{\partial x^n} \Longleftrightarrow (\imath 2\pi u)^n F(u,v), \qquad \frac{\partial^n f(x,y)}{\partial y^n} \Longleftrightarrow (\imath 2\pi v)^n F(u,v). \tag{5.9}$$

3. Convolution in the spatial domain is represented by multiplication in the spectral domain.

$$f(x,y) * g(x,y) = \int_{-\infty}^{\infty}\int_{-\infty}^{\infty} f(x_0,y_0)g(x_0-x,y_0-y)dx_0dy_0 \tag{5.10}$$

$$\Longleftrightarrow F(u,v)G(u,v) \tag{5.11}$$

where $*$ is the convolution operator. Alternatively, multiplication in the spatial domain relates to a spectral convolution, i.e.,

$$f(x,y)g(x,y) \Longleftrightarrow F(u,v) * G(u,v). \tag{5.12}$$

In the latter case G could typically be a windowing function.

4. The cross–correlation between two functions $f(x, y)$ and $g(x, y)$ is

$$R_{fg} = f \circledast g = \int_{-\infty}^{\infty}\int_{-\infty}^{\infty} f(x_0,y_0)g(x_0+x,y_0+y)dx_0dy_0 \tag{5.13}$$

where, $\circledast$ is the correlation operator. Hence,

$$f(x,y) \circledast g(x,y) \Longleftrightarrow F^*(u,v)G(u,v),$$

where, $F^*(u, v)$ represents the complex conjugate of $F(u, v)$. If $f = g$ the auto–correlation can be also be found.

5. The Power Spectral Density (PSD) is a measure of energy concentration and distribution in terms of frequency. For signals f and g the PSD, P_{fg}, is given by

$$P_{fg} = F^*G = |FG| \tag{5.14}$$

If $f = g$ then the auto-power spectrum is gained, i.e.,

$$P_{ff} = F^*F = |F|^2 \tag{5.15}$$

6. Power Spectral Density from covariance function C_{fg}

$$P_{fg} = \mathcal{F}\{C_{fg} - \mu_f\mu_g\} \tag{5.16}$$

where, μ_f and μ_g are the signal means. If either μ_f or μ_g are zero then $P_{fg} = \mathcal{F}\{C_{fg}\}$.

So here we can see two separate methods of gaining a signal's PSD characteristics either from its spatial form or its associated covariance function.

5.2 Spectral Optimal Interpolation

Optimal estimation studies of the geoid and mean sea surface have been investigated by *Moritz* (1980), *Wunsch* and *Zlotnicki* (1984), *Blanc* et al. (1990) and more recently *Jolly* (1995). In this section the spatial optimal interpolation theory is developed from the above references and we then transform these for treatment in the Fourier domain.

We intend to develop an estimate $\hat{s}$, of an unknown signal s, from a noisy set of observations, l. This estimate is deemed optimum by minimising a weighted least squares difference $\langle|\hat{s} - s|^2\rangle$, where the brackets represent a weighted integral over the surface. In matrix notation the linear estimate, $\hat{\mathbf{s}}$ based on a minimum linear variance is given by *Moritz* (1980) as

$$\hat{\mathbf{s}} = \mathbf{C}_{sl}\mathbf{C}_{ll}^{-1}\mathbf{l} = \mathbf{a}_{sl}\mathbf{l} \tag{5.17}$$

where, $\mathbf{C}_{ss}$ is the auto-covariance function (ACV) of s, $\mathbf{C}_{ll}$ the ACV of l and $\mathbf{C}_{sl}$ the cross-covariance between s and l. Also, $\mathbf{a}_{sl} = \mathbf{C}_{sl}\mathbf{C}_{ll}^{-1}$ is known as the least squares estimator matrix. The *a posteriori* estimate of the error, $\mathbf{C}_{\epsilon\epsilon}$, may be

obtained by

$$\mathbf{C}_{\epsilon\epsilon} = \mathbf{C}_{ss} - \mathbf{C}_{sl}\mathbf{C}_{ll}^{-1}\mathbf{C}_{ls} = \mathbf{C}_{ss} - \mathbf{C}_{sl}\mathbf{C}_{ll}^{-1}\mathbf{C}_{sl}^{\mathbf{T}} \tag{5.18}$$

where, $^{\mathbf{T}}$ represents the transpose of the matrix.

As mentioned above the least squares estimator, $\mathbf{a}_{sl}$, is given by

$$\mathbf{a}_{sl} = \mathbf{C}_{sl}\mathbf{C}_{ll}^{-1}. \tag{5.19}$$

Now, if we now make the assumption that the noisy signal, l is a linear combination of signal s and a collective noise signal n, such that

$$l = s + n \tag{5.20}$$

then we find that

$$\mathbf{C}_{ll} = \mathbf{C}_{ss} + \mathbf{C}_{nn} \tag{5.21}$$

and

$$\mathbf{C}_{sl} = \mathbf{C}_{ss} + \mathbf{C}_{sn} = \mathbf{C}_{ss} \tag{5.22}$$

since we assume there is no correlation between signal and noise, i.e., $\mathbf{C}_{sn} = 0$. Hence, equation 5.19 can now be rearranged to give

$$\hat{\mathbf{s}} = \mathbf{a}_{sl}\mathbf{l} = \mathbf{C}_{ss}\left[\mathbf{C}_{ss} + \mathbf{C}_{\mathbf{nn}}\right]^{-1}\mathbf{l} \tag{5.23}$$

and the *a posteriori* error estimate from equation 5.18 is now

$$\mathbf{C}_{\epsilon\epsilon} = \mathbf{C}_{ss} - \mathbf{C}_{ss}\left[\mathbf{C}_{ss} + \mathbf{C}_{nn}\right]^{-1}\mathbf{C}_{ss}. \tag{5.24}$$

Our ultimate intention is to develop a spectral equivalent of equations 5.23 and 5.24. The least squares estimator, $\mathbf{a}_{sl}$ is now equal to $\mathbf{C}_{ss}\left[\mathbf{C}_{ss} + \mathbf{C}_{nn}\right]^{-1}$. Rearranging we get

$$\left[\mathbf{C}_{ss} + \mathbf{C}_{nn}\right]\mathbf{a}_{sl} = \mathbf{C}_{ss} \tag{5.25}$$

Taking the Fourier transform of equation 5.25 using 5.16 gives transform pairs, $\mathbf{C}_{ss} \Longleftrightarrow P_{ss}$, $\mathbf{C}_{nn} \Longleftrightarrow P_{nn}$ and $\mathbf{a}_{sl} \Longleftrightarrow A_{sl}$. Since equation 5.25 may be written

as a convolution integral in the spatial domain (see *Schwarz* et al., 1990) then its spectral equivalent is a multiplication of components. Thus

$$[P_{ss} + P_{nn}]\, A_{sl} = P_{ss}. \tag{5.26}$$

Rearranging to obtain the spectral least–squares estimator we get

$$A_{sl} = \frac{P_{ss}}{P_{ss} + P_{nn}}. \tag{5.27}$$

Therefore, in the spectral domain the matrix inversion of $[\mathbf{C}_{ss} + \mathbf{C}_{nn}]$ in equation 5.23 is now simply a division of PSDs, $P_{ss} + P_{nn}$ at each discrete frequency. Transforming equation 5.17, into the spectral domain and noting that with $\mathbf{l} \Longleftrightarrow L$ and $\hat{\mathbf{s}} \Longleftrightarrow \hat{S}$ gives our spectral estimation, $\hat{s}$ such that

$$\hat{S} = A_{sl} L = \frac{P_{ss}}{P_{ss} + P_{nn}} L \quad \text{and therefore} \tag{5.28}$$

$$\hat{s} = \mathcal{F}^{-1}\left[\frac{P_{ss}}{P_{ss} + P_{nn}} L\right]. \tag{5.29}$$

Thus we see A_{sl} is simply a filtering function of the data function l. Also if there were no noise components within the signal (i.e., $P_{nn} = 0$) there would be exact signal replication since $A_{sl} = 1$, i.e., $\hat{S} = L$ or $\hat{s} = l$. Similarly the *a posteriori* error covariance estimate of equation 5.24 is modified to become

$$\mathbf{C}_{\epsilon\epsilon} = \mathcal{F}^{-1}\left[P_{ss} - \frac{P_{ss}}{P_{ss} + P_{nn}} P_{ss}\right]. \tag{5.30}$$

Now it has been shown that P_{nn} can be developed by a covariance analysis of the noise elements within the data, $\mathbf{C}_{nn}$. Alternatively a noise surface may be developed from the altimetry itself. The methodology of putting spectral optimal interpolation into practice and the modifications to equation 5.28 are discussed in the next chapter.

5.3 Geodetic Boundary Value Problems

Here flat Earth approximations to the Stokes' and Vening–Meinesz' Boundary Value Problems (BVPs) are derived. Stokes' problem involves the conversion of gravity anomalies, Δg to geoidal heights, N on the sphere. Whilst the Vening–

Meinesz' formulation, a variation on the Stoke's method, converts Δg to north and south deflections of the vertical. Complex derivations for both transforms exist (see *Schwarz* et al., 1990, for example) using convolution integrals on the sphere. For example, Stokes' transform (*Stokes*, 1849) is given by

$$N = \frac{R_e}{4\pi\gamma} \iint_\sigma S(\psi)\Delta g d\sigma \tag{5.31}$$

where,

N,	is the geoid height,
R_e,	the mean radius of the Earth,
γ,	the normal gravity,
σ,	the unit sphere, and
$S(\psi)$,	is Stokes' function for a computation angle ψ.

Stokes' function is a series of Legendre polynomials. Here,

$$\begin{aligned} S(\psi) &= \sum_{n=2}^{\infty} \frac{2n+1}{n-1} P_n(\cos\psi) && (5.32) \\ &= \frac{1}{\sin(\psi/2)} - 6\sin\frac{\psi}{2} + 1 - 5\cos\psi - 3\cos\psi \ln\left[\sin\frac{\psi}{2} + \sin^2\frac{\psi}{2}\right] && (5.33) \\ &\simeq \frac{2}{\psi}. && (5.34) \end{aligned}$$

Despite this assumption the derivation may be simplified by an alternative methodology.

A straight forward method for deriving solutions to the two boundary value problems using Laplace's equation and the fast Fourier transform exists. The Stokes' transform is developed from first principles whilst the Vening–Meinesz transform is adapted from theory developed by *Sandwell* (1992). Additionally a combined forward Stokes' and inverse Vening–Meinesz' transform essentially allows a geoid to be recovered from vertical deflection components.

To begin with a brief summary of geophysical parameters introduced in chapter 2 is given with their spectral equivalents.

5.3.1 Review of Gravity Field Parameters

There are four geodetic parameters critical for studies within this thesis. These are the

Geoid, N that may be obtained via Brun's formula linking it to the anomalous

potential, T by

$$N = \frac{T}{\gamma} \tag{5.35}$$

where, γ is the normal gravity. The FFT of 5.35 is obtained simply by the use of equation 5.7.

$$\mathcal{F}[N] = \hat{N} \Longleftrightarrow \frac{1}{\gamma}\mathcal{F}[T]. \tag{5.36}$$

$\hat{N}$ being the spectral transform of the geoid.

Eastern Deflection of the Vertical, $\eta(x, y)$ is given by

$$\eta = -\frac{1}{\gamma}\frac{\partial T}{\partial x} \tag{5.37}$$

and its spectral analogue using the differentiation relationship 5.9 is therefore

$$\eta \Longleftrightarrow \mathcal{F}[\eta] = \Theta = -\imath\frac{2\pi u}{\gamma}\mathcal{F}[T] \tag{5.38}$$

Northern Deflection of the Vertical, $\xi(x, y)$ is given by

$$\xi(x, y) = -\frac{1}{\gamma}\frac{\partial T}{\partial y} \tag{5.39}$$

hence giving the spectral equivalent

$$\xi \Longleftrightarrow \mathcal{F}[\xi] = \Xi = -\imath\frac{2\pi v}{\gamma}\mathcal{F}[T] \tag{5.40}$$

Gravity Anomaly, Δg in spherical coordinates is given by *Heiskanen* and *Moritz* (1967)

$$\Delta g(r) = -\frac{\partial T}{\partial r} - \frac{2}{r}T \tag{5.41}$$

where, r is the radial distance.

For our purposes we need to refer to a flat Earth approximation of Δg. This may be conveniently achieved via the removal of a long wavelength geoid. In

this case we now refer to an x, y, z coordinate system and

$$\Delta g \simeq -\frac{\partial T}{\partial z}. \tag{5.42}$$

Thus the residual geoid can be treated on a flat–Earth with the long wavelength component being added back after processing. The equivalent spectral transform is thus

$$\Delta g \Longleftrightarrow \mathcal{F}[\Delta g] = \Delta G = -\imath 2\pi w \mathcal{F}[T] \tag{5.43}$$

5.3.2 The Stokes' Transform

The Stokes' transform may be derived from Laplace's equation of the anomalous potential outside the geoid i.e.,

$$\nabla^2 T = \frac{\partial^2 T}{\partial x^2} + \frac{\partial^2 T}{\partial y^2} + \frac{\partial^2 T}{\partial z^2} = 0. \tag{5.44}$$

Using Equation 5.9 to transform 5.44 into the frequency domain and performing the necessary differentiation gives

$$4\pi^2 u^2 \mathcal{F}[T] + 4\pi^2 v^2 \mathcal{F}[T] + 4\pi^2 w^2 \mathcal{F}[T] = 0 \tag{5.45}$$

where, a three dimensional FFT is used. In the trivial case $\mathcal{F}[T] = 0$. Thus, the non–trivial case leaves

$$-w^2 = u^2 + v^2. \tag{5.46}$$

Rearranging and considering a x, y, z co–ordinate system with z positive vertically upwards, gives

$$w = -\imath\sqrt{u^2 + v^2}. \tag{5.47}$$

Now 5.44 may also be transformed. Thus,

$$-4\pi^2 u^2 \mathcal{F}[T] - 4\pi^2 v^2 \mathcal{F}[T] + \imath 2\pi w \mathcal{F}[\frac{\partial T}{\partial z}] = 0. \tag{5.48}$$

But from the flat Earth approximation in equation 5.42 substituted into 5.48 we get

$$-2\pi u^2\mathcal{F}[T] - 2\pi v^2\mathcal{F}[T] + \sqrt{(u^2+v^2)}\Delta G(u,v) = 0 \tag{5.49}$$

where, $\Delta g(x,y) \Longleftrightarrow \Delta G(u,v)$. Hence substituting 5.36 into 5.49 and rearranging gives

$$\hat{N} = \mathcal{F}[N] = \frac{1}{2\pi\gamma q}\Delta G(u,v) \tag{5.50}$$

where $q = \sqrt{(u^2+v^2)}$ is the total circular frequency. The geoid, $N(x,y)$, is now simply

$$N(x,y) = \mathcal{F}^{-1}\left[\frac{\Delta G(u,v)}{2\pi\gamma q}\right]. \tag{5.51}$$

It can be seen from equation 5.51 that at the zero circular frequency, i.e., $q = 0$ that a singularity occurs. This may be alleviated by a method suggested by *Heiskanen* and *Moritz* (1967) and converted for spectral domain usage by *Schwarz* et al. (1990). This involves substituting $1/q$ in equation 5.51 with

$$2\sqrt{\pi}\sqrt{\Delta x\Delta y} + \frac{\delta(u,v)-1}{q}. \tag{5.52}$$

Thus when $q = 0$, the spectral geoid $\hat{N}$ is no longer a singularity. However, this formulation is in error. In actuality any value in equation 5.51 at the zero frequency translates to a bias in the spatial domain. Therefore replacing the singularity by a zero results in an output signal with a zero mean.

The gravity anomaly, Δg may be determined by rearranging 5.50. Here,

$$\Delta g(x,y) = \mathcal{F}^{-1}\left[2\pi\gamma q\hat{N}\right]. \tag{5.53}$$

We can therefore see that Δg is in–phase with the geoid. However since multiplication with q occurs, this implies higher frequencies are more prominent.

5.3.3 The Vening–Meinesz' Transform

The Vening–Meinesz' transform is adapted from *McAdoo* and *Marks* (1992) again using the Laplace method similar to the above. Here, however, gravity anomalies are to be determined from DOV components. We convert Laplace's equation (5.44)

to the spectral domain via a single partial differentiation in each dimension using the property given in equation 5.9, i.e.,

$$\begin{aligned}
\frac{\partial T(x,y,z)}{\partial x} &= \imath 2\pi u \mathcal{F}[T(x,y,z)], \\
\frac{\partial T(x,y,z)}{\partial y} &= \imath 2\pi v \mathcal{F}[T(x,y,z)] \quad \text{and} \\
\frac{\partial T(x,y,z)}{\partial z} &= \imath 2\pi w \mathcal{F}[T(x,y,z)].
\end{aligned}$$

So essentially we get

$$\imath 2\pi u \mathcal{F}[\frac{\partial T}{\partial x}] + \imath 2\pi v \mathcal{F}[\frac{\partial T}{\partial y}] + \imath 2\pi w \mathcal{F}[\frac{\partial T}{\partial z}] = 0. \tag{5.54}$$

Substituting η, ξ and Δg for $\partial T/\partial x$, $\partial T/\partial y$ and $\partial T/\partial z$ using equations 5.37, 5.39 and 5.42 respectively gives

$$-\imath 2\pi\gamma u \mathcal{F}[\eta] - \imath 2\pi\gamma v \mathcal{F}[\xi] + \imath 2\pi w \mathcal{F}[\Delta g] = 0. \tag{5.55}$$

Considering the transform equations 5.38, 5.40 and 5.43 then allows

$$w\Delta G = \gamma(u\Theta + v\Xi) \tag{5.56}$$

to be formed. Now substituting equation 5.47 into 5.56 and rearranging gives the spectral gravity anomaly

$$\Delta G(u,v) = \frac{\imath\gamma\,(u\Theta + v\Xi)}{\sqrt{u^2+v^2}}. \tag{5.57}$$

Finally taking the IFFT gives us the inverse Vening–Meinesz' transform, i.e.,

$$\Delta g(x,y) = \mathcal{F}^{-1}[\Delta G(u,v)] = \imath\gamma\mathcal{F}^{-1}\left[\frac{(u\Theta + v\Xi)}{\sqrt{u^2+v^2}}\right]. \tag{5.58}$$

Therefore it can be seen that providing DOV components are available in gridded form then Δg may be obtained. The relevance of this will become apparent in chapter 7 when the global gravity anomaly field is determined in order to improve MSS modelling. Further, the existence of the imaginary $\imath$ operator in 5.58 shows DOV components are out of phase with the gravity anomaly.

The Forward Transform may also be found. Equation 5.57 may be written as

$$\Delta G(u,v) = \frac{\imath\gamma u\Theta}{\sqrt{u^2+v^2}} + \frac{\imath\gamma v\Xi}{\sqrt{u^2+v^2}} = \imath\gamma\hat{\mathbf{q}}\cdot\mathbf{D} \tag{5.59}$$

where, $\mathbf{D}$ is the spectral DOV vector

$$\mathbf{D} = \Theta\hat{\mathbf{i}} + \Xi\hat{\mathbf{j}} \tag{5.60}$$

and the circular frequency vector $\mathbf{q}$ is

$$\mathbf{q} = u\hat{\mathbf{i}} + v\hat{\mathbf{j}} \tag{5.61}$$

and so $\hat{\mathbf{q}} = \mathbf{q}/|\mathbf{q}|$.

Now since $\mathbf{D}$ and $\hat{\mathbf{q}}$ are in parallel (see equations 5.38 and 5.40) the forward transform can be determined by taking the product of $\hat{\mathbf{q}}$ with equation 5.59 giving

$$\hat{\mathbf{q}}\Delta G(u,v) = \imath\gamma(\hat{\mathbf{q}}\cdot\mathbf{D})\hat{\mathbf{q}}. \tag{5.62}$$

Hence the forward Vening–Meinesz transform is thus

$$\mathbf{D} = -\frac{\imath}{\gamma}\hat{\mathbf{q}}\Delta G. \tag{5.63}$$

5.3.4 The Geoid from DOV components

Additionally the geoid, N may be expressed in terms of spectral DOV components, Θ and Ξ by substituting equation 5.57 into 5.51 giving

$$N(x,y) = \frac{\imath}{2\pi}\mathcal{F}^{-1}\left[\frac{(u\Theta + v\Xi)}{q^2}\right]. \tag{5.64}$$

Therefore, providing DOV components are available then in principle the geoid may be determined spectrally.

5.3.5 Vertical Gravity Gradient

The vertical gravity gradient, $\partial\Delta g/\partial z$, is a powerful analytical tool in physical geodesy and requires no spectral transformation. This parameter is determined by the substitution of η, ξ and Δg (equations 5.37, 5.39 and 5.42) in Laplace's

equation (5.44). Thus

$$-\gamma\frac{\partial\eta}{\partial x}-\gamma\frac{\partial\xi}{\partial y}-\frac{\partial\Delta g}{\partial z}=0. \tag{5.65}$$

Rearranging we get

$$\frac{\partial\Delta g}{\partial z}=-\gamma\left(\frac{\partial\eta}{\partial x}+\frac{\partial\xi}{\partial y}\right)\qquad\text{Eötvös} \tag{5.66}$$

where, Eötvös units are s^{-2}. Hence a quick means of mapping the high frequency gravity field by only taking first gridded differences of η and ξ is available. Also any land, ice and sea boundaries may be evaluated without the problem of the Gibbs' ringing effect at such discontinuities.

Chapter 6

Spectral Optimal Interpolation for a ERS-1 MSS Solution

6.1 Introduction

An optimally interpolated mean sea surface is now constructed using high density altimetry from the ERS-1 geodetic phase using spectral techniques developed in chapter 5. For the ERS-1 geodetic phase the platform was placed into a 168–day repeat orbit for 2 cycles. However, rather than repeating the orbit, the satellite was manœuvered at the end of the first cycle. The adjustment to the satellites orbit allowed the ground track of the second cycle to interleave with that of the first. With a total of 2411 passes within each cycle an equatorial spacing of approximately 8 km ($\sim 0.075°$) is realised. Thus in principle, a mean sea surface resolution of ~16km ($\sim 0.15°$) is achievable in view of the Nyquist sampling theorem.

Altimetry is first corrected for tidal, environmental/electronic and surface effects as discussed in chapter 4. Long wavelength radial orbit error is then minimised via the use of dual ERS-1 and TOPEX/Poseidon (TP—E) dual crossover residual time series. A continuous radial orbit error correction is achieved by fitting cubic B–splines to the set of residuals. After further editing, Sea Surface Variability (SSV) (a major problem in MSS determination) is reduced within the ERS-1 sea heights via a model derived from TOPEX/Poseidon data.

Corrected altimetry is binned and gridded forming a *first guess* MSS and is then optimally interpolated (see Figure 6.1) within the frequency domain. The resultant product is then validated against both independent and dependent sea surface height data sets. Here, 15 cycles of high precision T/P sea surface heights are used as an independent source of validation. Additionally the MSS is compared against

ERS-1 and enhanced GEOSAT geodetic phase corrected sea surface heights.

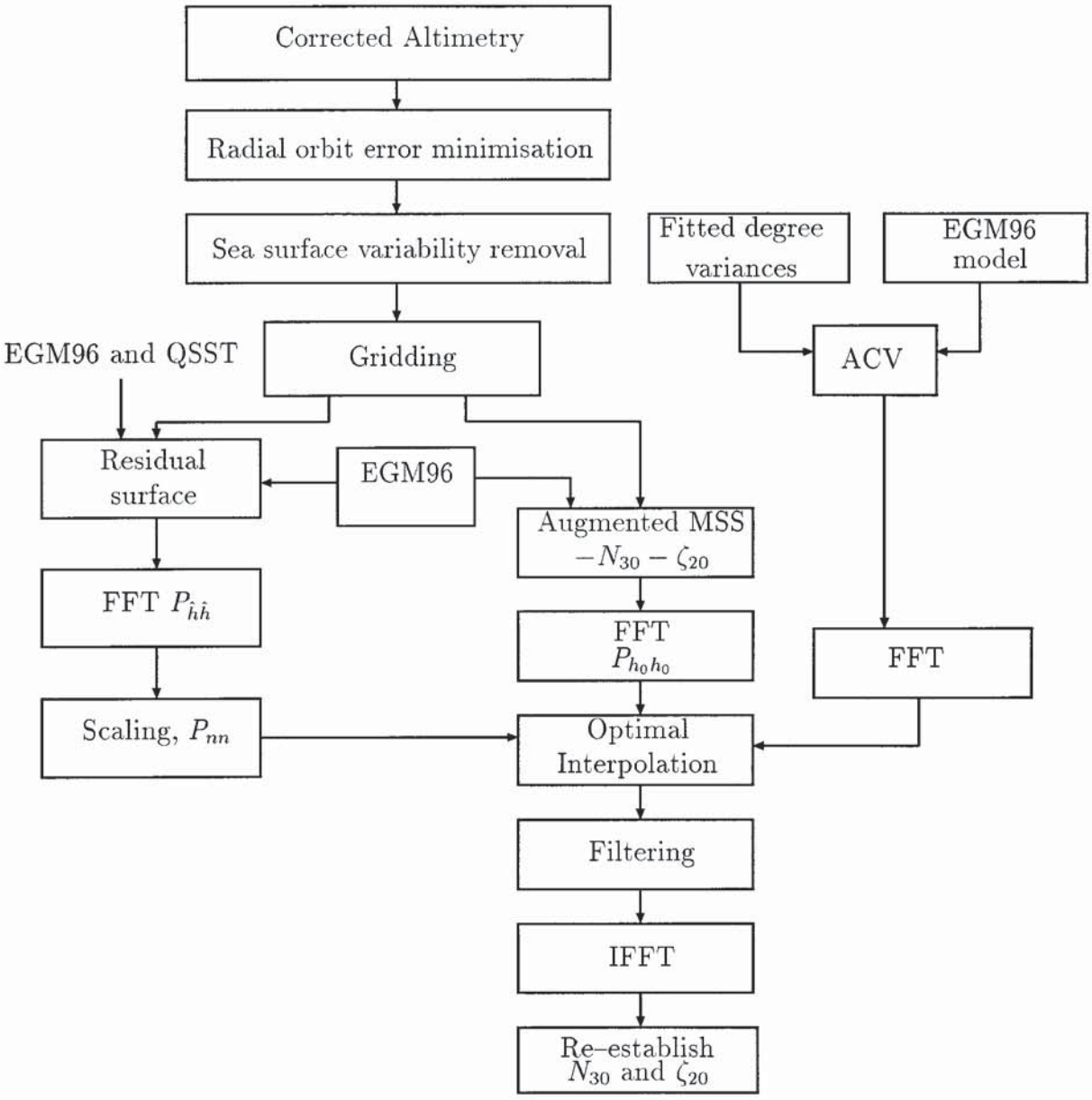

Figure 6.1: Schematic diagram describing optimally interpolated MSS procedure.

6.2 Data Pre–Processing

Off–line Ocean Product (OPR) data for the entire ERS-1 geodetic phase between 10th April 1994 and 23rd March 1995 (MJD 49454–49790) were used. The altimetric Geophysical Data Records (GDRs) were edited for land/ice flagged data leaving only ocean/shallow sea surface heights. This supplies as much information

as possible despite the poor tidal definition over the majority of shallow water and coastal regions.

The remaining data was then corrected for

Tides: Solid Earth tide, ocean/ocean loading tides supplied by the CSR3.0 model and also polar tides are catered for.

Tropospheric delay: The ERS-1 microwave sounder (ATSR-M) provided information on atmospheric total water vapour content in order to correct for the wet tropospheric effect. The dry tropospheric effect was catered for by French meteorological model pressure values.

Ionospheric delay: The Bent model determined ionospheric corrections stored in the GDR's was utilised.

Inverse Barometer effect: The standard localised effect using equation (4.15) in section 4.5.1 was used. No global average was applied as specified in section 4.5.1.

Sea–state bias: This was calculated as 5.95% of the significant wave height (see *Carnochan*, 1997, for determination of this parameter).

USO drift and bias Jumps: supplied by ESRIN on the World Wide Web.

In addition data were also edited if 10 per–second sea height observations had a standard deviation exceeding 25 cm; wet tropospheric corrections were derived from a model, significant wave height exceeded 25 m; backscatter coefficient (σ°) was outside $6 \leqslant n \leqslant 25$dB and any other model failed to supply a correction.

6.3 Radial Orbit Error Minimisation

In chapter 4 the case was put forward for need to reduce long wavelength radial orbit error for the ERS-1. Fortunately such a method is available in the form of dual crossover minimisation. This assumes that if the ephemeris of one satellite is accurately known then it may be used to enhance the less accurate ephemeris of a second satellite.

Between July 1993 and July 1995, both TOPEX/Poseidon and ERS-1 were functional and since T/P has the more accurate orbit (*Tapley* et al. (1996) quote a typical orbital error of $\sim$2.8 cm RMS for a 10 day repeat period) then in principle the radial orbit error of ERS-1 may be reduced.

Applying dual crossover theory to the T/P and ERS-1 platforms we take the difference between altimetric sea surface heights, $H_{TP}(t_1)$ and $H_E(t_2)$ (T/P and ERS-1 sea heights respectively) at corresponding times t_1 and t_2. These differences are taken at crossover locations where T/P ground tracks crossover with those of ERS-1. The ith crossover residual, ΔH_i^{DX}, will contain errors due to;

1. the two separate orbital heights, Δ_{TP} and Δ_E,
2. those contained in processing corrections, δ_{TP} and δ_E, and
3. variations in quasi–static sea-surface topography (QSST), ζ_{TP} and ζ_E.

The ith residual may therefore be represented by the function

$$\begin{aligned}\Delta H_i^{DX} &= H_{TP}(t_1) - H_E(t_2) \\ &= \Delta_{TP}(t_1) - \Delta_E(t_2) + \zeta_{TP}(t_1) - \zeta_E(t_2) + \delta_{TP}(t_1) - \delta_E(t_2). \end{aligned} \tag{6.1}$$

We assume $\Delta_{TP} \simeq 0$ (i.e., TOPEX/Poseidon radial orbit error is small and maybe therefore be disregarded) and residual differences in correction errors, $\delta_{TP} - \delta_E$, are given by δ_e. The time difference between crossover measurements is important, since one measurement is required to be de–correlated to another. If TP—E crossover differences are determined with an interval of less than 5 days, for example, then sea surface topography changes will remain small, hence $\zeta_{TP} - \zeta_E \simeq 0$. Thus equation 6.1 will reduce to

$$\Delta H_i^{DX} = \Delta_E + \delta_e \tag{6.2}$$

Dual TP—E crossover difference residuals were computed leading to a discrete time series of radial orbit error corrections for the ERS-1 ephemeris.

Le Traon et al. (1995) showed that fitting cubic B–spline functions across dual and single satellite crossover residuals was a viable method of computing a continuous correction for the radial orbit error. They showed the method could provide a typical fit of ~ 7 cm RMS to the ERS-1 single satellite crossover data set. The method therefore showed improvements over the alternative procedure of the least squares fitting of sinusoids to dual crossover residuals. Here, *Jolly* and *Moore* (1996) reported a fit of 11.8 cm RMS over a 35–day cycle whilst *Cazenave* et al. (1996) published 7.5 to 9 cm for ten ERS-1 geodetic phase sub–cycles (37 days). More recently *Le Traon* and *Ogor* (1998) further analysed the cubic spline method claiming the ERS-1 orbit error could be minimised to just 2 cm RMS difference to T/P orbits.

The procedure adopted for studies described within this study is based on a modified version of the *Le Traon* et al. algorithm. The fundamental difference here is the use of only dual crossovers. The inclusion of single crossovers complicates the spline fitting procedure and provides only limited benefit. Essentially, single ERS-1 crossovers have been shown to be of use outside the T/P latitudinal range (±66°), and in regions of complex geometry, such as Indonesia and the Mediterranean. However tidal modelling over these regions and continental shelves are inaccurate. Secondly, the MSS derived here will only be developed over T/P coverage. Thus a simplified procedure for MSS modelling is deemed acceptable.

Dual TP—E crossover residuals were calculated using T/P orbit heights taken directly from AVISO distributed data products whilst ERS-1 orbital ephemerides were calculated at Aston University rather than those available on CDROM GDR's distributed by CERSAT. Residual time differences less than 5 days were chosen in order to avoid the removal of oceanic signals.

A two–stage procedure was used to reject erroneous residuals. In the first instance an initial bias of 44 cm was removed from all residuals avoiding the skewing of the data and then a weak rejection threshold of 1 metre was applied. Secondly, residuals were split up into separate TOPEX–ERS-1 (T–E) and Poseidon–ERS-1 (P–E) sets. Statistics were calculated, a bias removed and 3σ rejection criterion applied (results are given in Table 6.1.) Residuals were finally combined and sorted with respect to ERS-1 referenced time to create a discrete time series of radial corrections to the ERS-1 ephemeris.

In order to enhance the ERS-1 orbit over all altimetry points it is necessary to fit cubic B–Splines over the entire residual time series bounded by times, t_{min} and t_{max}. Following *Hayes* (1974) we assume the time series contains random errors.

The ith normalised cubic B–Spline is defined by $N_i(t)$ over a selected set of h knots given by $\lambda_1 \longrightarrow \lambda_h$. Additionally, a condition that $N_i(t) = 0$ is applied outside the range $\lambda_{i-4} < t < \lambda_i$. Within these limits $N_i(t)$ is computed from the recurrence relation

$$N_{n,i}(t) = (t - \lambda_{i-n})N_{n-1,i-1}(t) + (\lambda_i - t)N_{n-1,i}(t); \tag{6.3}$$

here, $N_{n,i}(t)$ is the B–Spline of degree $n-1$ (we require degree 3, so $n = 4$) that is initialised with $n = 1$. So that,

$$N_{1,i}(t) = \begin{cases} 1, & \lambda_{i-1} \leqslant t < \lambda_i \\ 0, & \text{otherwise} \end{cases} \tag{6.4}$$

For the generation of the full set of B–Splines it is a requirement of the algorithm (*Hayes*, 1974) that four additional knots are included at the extremities of the time series, i.e.,

$$\lambda_{-3} < \lambda_{-2} < \lambda_{-1} < \lambda_0 \leqslant t_{min} < t_{max} \leqslant \lambda_{h+1} < \lambda_{h+2} < \lambda_{h+3} < \lambda_{h+4}.$$

This augmented set of knots allows $h + 4$ B–Splines to be produced, i.e.,

$$N_i(t), \quad \text{for} \quad i = 1, 2, \ldots, h + 4, \tag{6.5}$$

and allows the estimated radial orbit error, Δh_{roe} to be determined such that

$$\Delta h_{roe}(t) = \sum_{i=1}^{h+4} c_i N_i(t). \tag{6.6}$$

The coefficients, c_i are determined in the least–squares sense via the generation of the observation equations, f_j for each data point j over a set of m dual crossover differences, or

$$\sum_{i=1}^{h+4} c_i N_i(t_j) = f_j, \qquad j = 1, \ldots, m. \tag{6.7}$$

In matrix form this may be represented by

$$\mathbf{Ac} = \mathbf{f}. \tag{6.8}$$

Here $\mathbf{A}$ is a m by $h + 4$ matrix whilst $\mathbf{c}$ and $\mathbf{f}$ are column matrices. Converting the observation equations to normal equations, i.e.,

$$\mathbf{A}^{\mathrm{T}}\mathbf{Ac} = \mathbf{A}^{\mathrm{T}}\mathbf{f}. \tag{6.9}$$

c_i are retrieved via a suitable matrix inversion of $\mathbf{A}^{\mathrm{T}}\mathbf{A}$. Hence,

$$\mathbf{c} = (\mathbf{A}^{\mathrm{T}}\mathbf{A})^{-1}\mathbf{A}^{\mathrm{T}}\mathbf{f}. \tag{6.10}$$

Cubic spline fitting departed from that prescribed by *Le Traon* et al. (1995) (also described in *Cullen* et al. (1997)) in that the criteria for the choice of knot locations differed. Here, knots were positioned at the beginning and end of each pass if there were at least 5 residuals within the arc. Also, a third knot was positioned at the central point in the arc if at least 10 residuals existed.

Phase	Period (MJD)	No of crossovers T	P	Total	Pre fit σ (cm) T	P	No of Arcs	No of Knots	No of residual rejections	RMS Fit σ (cm)
C	48725–49350	559464	57533	616960	13.1	13.05	16508	45851	26365	5.92
D	49350–49450	144780	12980	157760	10.71	10.76	3532	9942	9950	5.91
E	49450–49790	425787	34333	460120	12.11	11.39	12152	34102	17315	5.80
F	49790–49960	184767	25626	210393	10.36	11.08	5580	15659	6904	5.75

Table 6.1: Statistics for the fit of cubic splines to dual TP/E crossover residuals for the phases C(1^{st} Multi-disciplinary), D(2^{nd} Ice), E(Geodetic) and F(2^{nd} Multi-disciplinary). ERS-1 orbits are calculated from SATAN–A programme.

Additionally, an iterative procedure was also employed in order to further remove erroneous residuals not detected by simple thresholding. This was achieved by selecting knots for the data set, fitting the spline, calculating statistics and removing residuals that differed from the spline fit by 3σ. This process was then repeated for several iterations.

It was also noted by visual inspection that the cubic spline fit for residuals over equatorial regions was not acceptable. This was most likely due to the greater number of dual crossovers at the latitudinal extremes of the T/P orbit constraining the fit in these regions. In order to alleviate this it was necessary to apply a larger significance to equatorially based residuals in the form of a weighting scheme. The jth residual was weighted as a function of latitude, ϕ given by

$$W_j(t) = \cos^2 \phi. \tag{6.11}$$

It may be noticed from Table 6.1 (page 93) that a better fit is achieved in comparison to the $\sim$7cm achieved by the *Le Traon* et al. algorithm. The most probable reason for this is due to the use of a greater number of knots applied in the procedure and the employment of the iterative procedure. A typical spline fit is displayed in Fig. 6.2 (page 94) for a portion of the day 7th August 1994. Also a histogram is shown in Fig. 6.3 (page 95) displaying the reduction in residual values before and after orbit enhancement. Finally, the before and after fit crossover differences are displayed for the entire ERS-1 geodetic mission in Figure 6.4 (page 96.) Here we can see the overall reduction in orbit error although some regions exist were the spline fit seems not to have totally succeeded. The likely reason for this stems from high frequency noise within the set of crossovers. Here the spline fitting procedure fits to the long wavelength signal thus attenuating the higher frequency

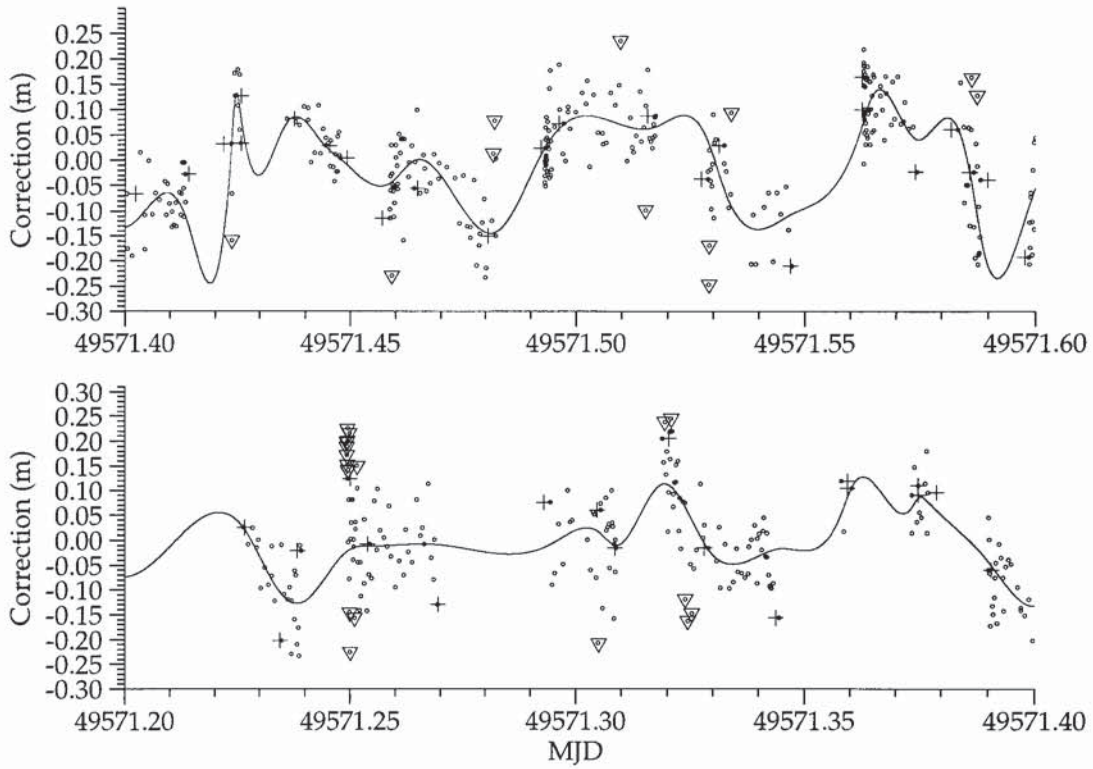

Figure 6.2: Cubic spline fit for dual TP-E crossover residuals for MJD 49571 (7th August 1994). Symbols are; (—) representing the cubic B–spline, (o) are residuals, (+) are knot locations and ($\bigtriangledown$) represent rejected residuals.

components.

6.3.1 Sea–Surface Variability Removal

The effect of Sea Surface Variability (SSV) on a MSS model is the generation of cross–track gradients in regions of intense activity such as the Kurishio and Gulf stream currents. Typically SSV would be reduced via the stacking of repeat data. However, in using ERS-1 geodetic phase data stacking of altimetry cannot take place; though an alternative method is available. This process removes SSV from each observation via the following steps.

1. For precise variability generation T/P data was chosen for reasons of accuracy and independence from ERS-1 data.

2. The data (see *Lam* and *Moore*, 1995, for a fuller explanation) is binned into 2° by 360°/157° bins. The mean is computed for each bin and removed from each measurement resident within that bin. Essentially this is the removal of a long wavelength MSS leaving variability over the time limits imposed by

the data.

3. Under the assumption that variability remains constant within the dimensions of the bin, a spatial optimal interpolation scheme (*Moritz*, 1980) is applied to all bins from which variabilities at intervals of 5 days are computed.

4. From the time series a variability can be determined for a particular date (within the time series limits) via a simple linear interpolation.

This method will remove a significant proportion of the variability signal although some of it will be inevitably retained. This would equally be the case with the use of stacked data.

6.3.2 Gridding

There are a large number of methods for gridding data. Bi–linear interpolation, distance weighted gridding and the fitting of surface splines have all been used in previous MSS studies. The method used here is that of distance weighting. Data is sorted into bins of square size 0.075° corresponding to the ERS-1 2 × 168 day equatorial ground track spacing of ~8 km. Each bin has an weighted average value

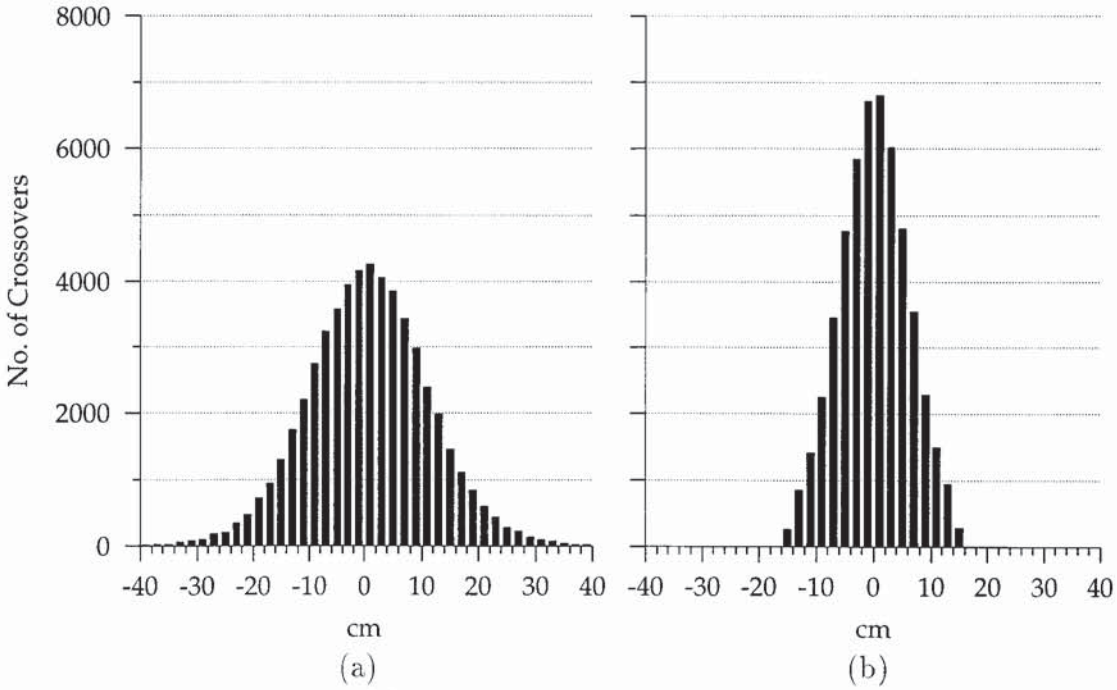

Figure 6.3: (a) Before and (b) after orbit enhancement crossover difference histograms showing reduction in radial orbit error.

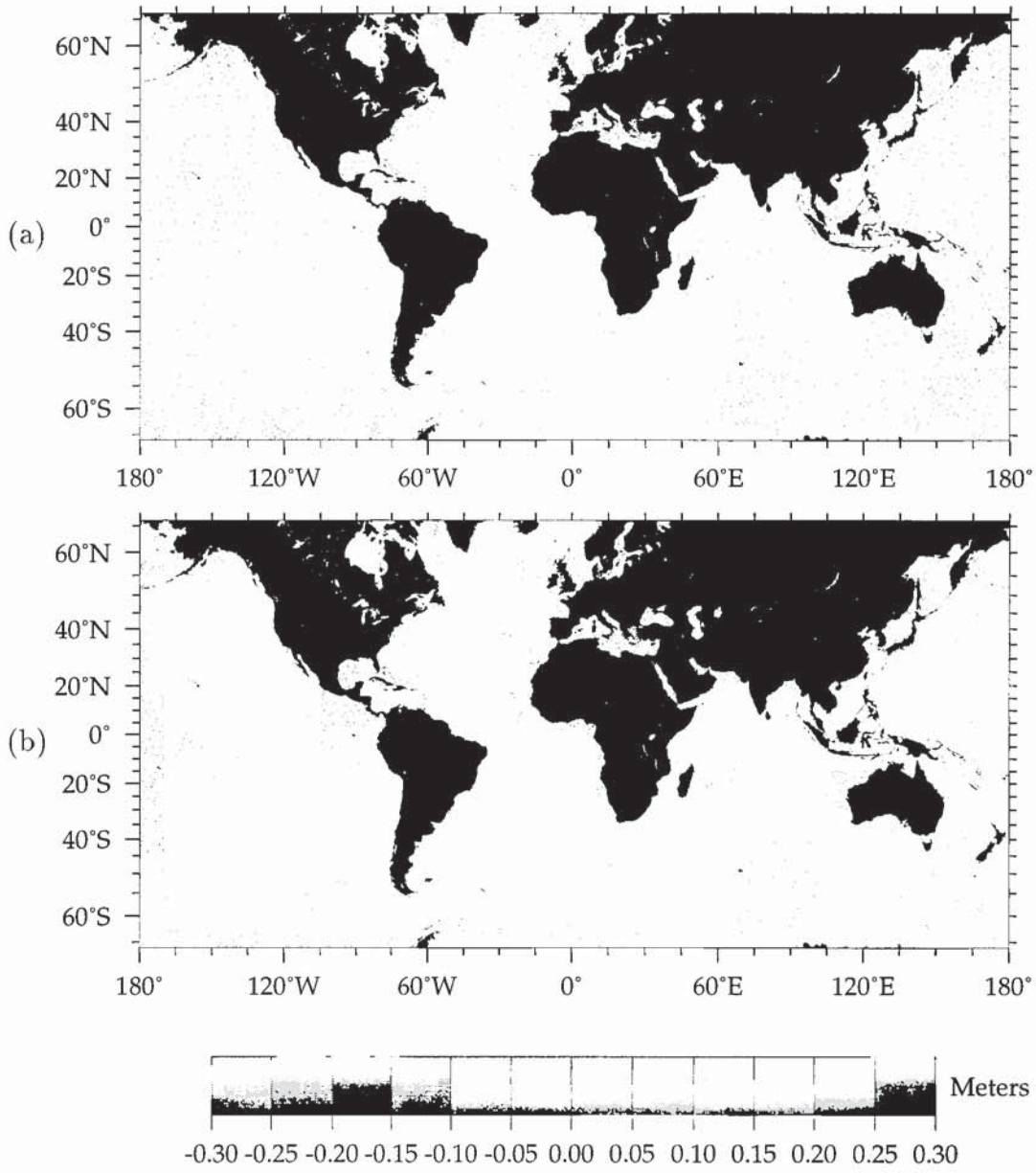

Figure 6.4: Crossover difference for (a) before and (b) after orbit enhancement for the entire geodetic phase of the ERS-1 mission.

determined. The weighting scheme is calculated from

$$W_j = e^{-d/\sqrt{2\Delta x}} \tag{6.12}$$

where, d is the distance from the grid point in degrees and Δx is the grid spacing, also in degrees. Additionally an iterative scheme is employed. Here any data points $\pm 3\sigma$ from the mean bin value are edited and a new average is computed. For ERS-1 a grid was computed over the whole $\pm 82°$ latitudinal range despite erroneous radial

orbit error minimisation outside the TOPEX/Poseidon coverage. These regions are then used later for windowing as part of the optimal interpolation procedure but are left out of the final model.

On account of the large amounts of data the actual software procedure does vary slightly (see appendix C.)

6.4 Spectral Optimal Interpolation

Spectral optimal interpolation requires that equation 5.28 be adapted for practical use. Reiterating, this equation is given by

$$\hat{S} = A_{sl}L = \frac{P_{ss}}{P_{ss} + P_{nn}}L \tag{6.13}$$

where,

$\hat{S}$, is the spectral estimation of the MSS,
L, is the spectrum of the original noisy data set, and
A_{sl}, the spectrum of the least squares estimator.

A_{sl} is expanded utilising Power Spectral Densities (PSDs) for P_{ss}, the estimate of signal power, and P_{nn}, the estimate of altimetric measurement noise power in the frequency domain. There are three main reasons for adapting equation 6.13 namely;

1. The ERS-1 covers a latitudinal range of $\pm 82°$. Therefore the first MSS guess will contain wavelengths (from the total loss of 16° of information over both polar caps) in the latitudinal direction that cannot be resolved by the FFT.

2. Due to the non–periodicity of the surface in the latitudinally direction a windowing procedure is required to smooth the latitudinal extremes ($\pm 82°$ to 66°). This also results in long wavelength components being unresolved.

3. Finally, it was suggested by *Wunsch* and *Zlotnicki* (1984) that the spatial least–squares procedure is improved when a long wavelength model has been removed. This is based on the premise that reduced power allows an easier distinction between residual signal and noise. It was therefore decided that this methodology should also be applied in the frequency domain.

The procedural modification that is required due to the above three points is the same. That is, the removal of a geoid to degree and order 30 (cosine tapered

to degree 40)[1] and sea surface topography to degree 20. The geoid removal was chosen arbitrarily at a cut–off of degree 30 and sea surface topography model, whilst being the secondary source of long wavelength energy, is resolvable from the geoid to $n \sim 20$ degrees (see Figure 6.5). These long wavelength components

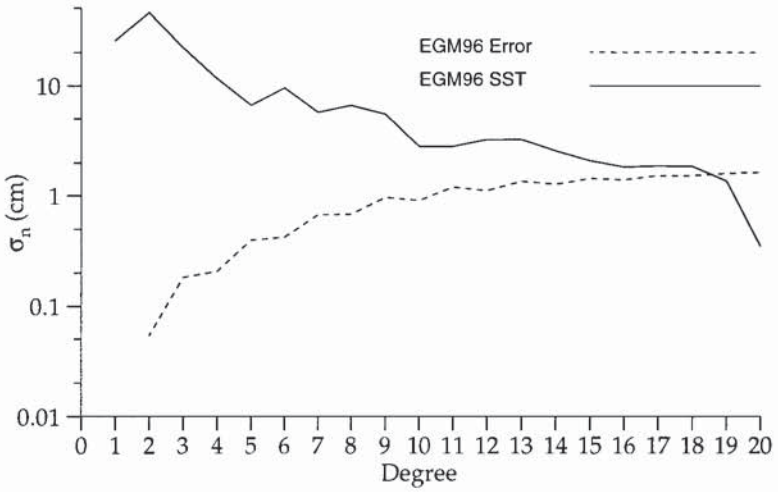

Figure 6.5: EGM96 geoid error against its SST signal to degree 20.

are re–applied back into the model at the end of the procedure. Additionally, this removal supports leaving out single crossovers in the radial orbit error minimisation methodology since latitudinal extremities ($> |66°|$) are disregarded in the final model.

Following *Blanc* et al. (1990), the optimal MSS estimate $\hat{h}$, at a point with geodetic coordinates ϕ, λ is given in the spatial domain by *Mazzega* and *Houry* (1989) such that

$$\hat{h}(\phi, \lambda) = h_{lw} + C_{h_0 h_0}[C_{h_0 h_0} + C_{nn}]^{-1}(d_0 - h_{lw}) \tag{6.14}$$

where,

[1]Cosine tapering of the EGM96 model coefficients is used to reduce spectral ringing (see *Cazenave* (1994) for a description and example of this phenomenon in terms of spherical harmonic expansions).

$\hat{h}$, represents our gridded final optimal estimate;

d_0, is the altimetric data set;

h_0, represents an initial *guess* MSS signature minus a long wavelength component,

h_{lw}, long wavelength component.

h_{lw} is a combined 20 by 20 sea surface topography, ζ_{20} and N_{30}, a 30 by 30 geoid both derived from the EGM96 gravity field model, i.e.,

$$h_{lw}(\phi, \lambda) = N_{30}(\phi, \lambda) + \zeta_{20}(\phi, \lambda). \tag{6.15}$$

h_{lw} is removed from the gridded noisy sea surface heights, d_0, for reasons described above regarding the non–resolvability of the longer wavelengths. Also, there are two covariance matrices namely $C_{h_0 h_0}$, the auto–covariance describing our initial estimate h_0, and C_{nn} the auto–covariance describing the errors within the altimetric signal. Conversion to the spectral domain (see section 5.2) avoids the large matrix inversion of $[C_{h_0 h_0} + C_{nn}]$ and reduces computation time significantly (see *Schwarz* et al., 1990, for example). Therefore,

$$\hat{h} = \mathcal{F}^{-1}\left[H_{lw} + \left(\frac{P_{h_0 h_0}}{P_{h_0 h_0} + P_{nn}}\right)(D_0 - H_{lw})\right] \tag{6.16}$$

where, $\mathcal{F}^{-1}$ denotes the inverse FFT operator (see chapter 5) for the transformation from frequency to spatial domains. Also $\hat{H}$, D_0 and H_{lw} are transformations of $\hat{h}$, d_0 and h_{lw} respectively in equation 6.16. Computationally, the calculation of H_{lw} would typically be in the spatial domain (being added back after the optimal interpolation procedure.) Likewise $D_0 - H_{lw}$ would also be computed in the spatial domain, i.e., if $H_r \Longleftrightarrow (d_0 - h_{lw})$. Then,

$$\hat{h} = h_{lw} + \mathcal{F}^{-1}\left[\left(\frac{P_{h_0 h_0}}{P_{h_0 h_0} + P_{nn}}\right) H_r\right]. \tag{6.17}$$

The associated enhanced MSS covariance error, $C_{\hat{h}\hat{h}}$, may also be adapted from equation 5.24. Here,

$$C_{\hat{h}\hat{h}} = C_{h_0 h_0} - C_{h_0 h_0}[C_{h_0 h_0} + C_{nn}]^{-1} C_{h_0 h_0} \tag{6.18}$$

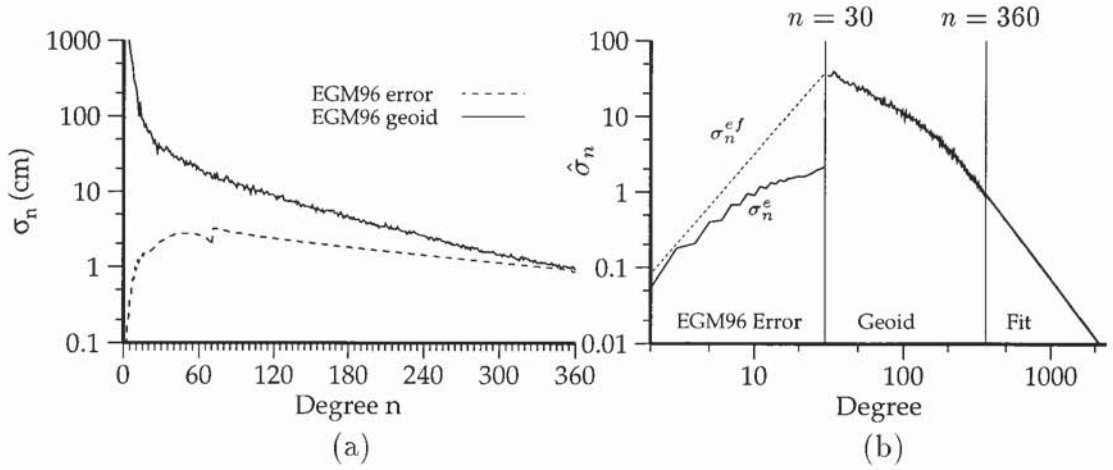

Figure 6.6: (a) EGM96 geoid and geoid error degree standard deviations, (b) degree constructed standard deviations for first guess description of the reduced wavelength MSS. Between degrees 2 and 30 there is the EGM96 geoid error and a linear fit to remove the discontinuity at degree 30 (see text.)

and its spectral equivalent is

$$P_{\hat{h}\hat{h}} = P_{h_0h_0} - \frac{P_{h_0h_0}}{P_{h_0h_0} + P_{nn}} P_{h_0h_0} \tag{6.19}$$

from which the covariance may be estimated via the inverse transformation of P_{nn}, i.e.,

$$C_{\hat{h}\hat{h}} \Longleftrightarrow P_{\hat{h}\hat{h}}. \tag{6.20}$$

It is therefore possible, in theory, to calculate the optimal estimate $\hat{h}$ by constructing the spectral equivalent of equation (6.14) through three FFT transformations giving $(D_0 - H_{lw})$, $P_{h_0h_0}$ and P_{nn}. Such parameter constructions are now described.

6.4.1 Generating the Auto–Covariance Function, $C_{h_0h_0}$

The auto–covariance of the reduced *first guess* MSS signal, $d_0 - h_{lw}$, is required as a signature for errors to be reduced within the MSS. This function, $C_{h_0h_0}$ is to be computed from a combination of

1. EGM96 geoid error degree variances, i.e., σ,
2. EGM96 geoid degree variances to degree 360, i.e., D,
3. beyond degree 360 a geoid degree variance fit computed to deal with the EGM96 spectral limit.

The anomalous potential, T, auto–covariance (ACV) function C_{TT} determined from a spherical harmonic expansion of the Earth is given by *Heiskanen* and *Moritz* (1967), such that

$$C_{TT} = \sum_{n=1}^{n_{max}} \sigma_n^2 P_n(\cos\psi) \tag{6.21}$$

where, n is the degree, $P_n(\cos\psi)$ are Legendre polynomials, ψ is the spherical distance between two points and $n_{max}=2400$ corresponds to the maximum resolution obtainable. σ_n^2 are potential degree variances calculated from

$$\sigma_n^2 = \sum_{m=0}^{n} (\sigma_{\bar{C}_{nm}}^2 + \sigma_{\bar{S}_{nm}}^2) \tag{6.22}$$

where m is the order and $\sigma_{\bar{C}_{nm}}$, $\sigma_{\bar{S}_{nm}}$ are C and S coefficient standard deviations, see chapter 2.

On the geoid the ACV is computed from Brun's equation (Eq. 5.35) and rearranged to give

$$C_{h_0 h_0} = R_e^2 \sum_{n=1}^{n_{max}} \hat{\sigma}_n^2 P_n(\cos\psi) \tag{6.23}$$

where, R_e is the mean radius of the Earth. $\hat{\sigma}_n^2$ represents degree variances for the signature MSS model here developed from

$$\hat{\sigma}_n = \begin{cases} \sigma_n^e, & 2 \leqslant n \leqslant 30 \\ D_n, & 31 \leqslant n \leqslant 360 \\ D_n^f, & 361 \leqslant n \leqslant 2400 \end{cases} \tag{6.24}$$

where, σ_n^e, D_n and D_n^f are standard deviations for EGM96 geoid error, EGM96 geoid and EGM96 geoid extrapolation fit. Geoid and geoid error degree standard deviations are displayed in Figure 6.6a. Figure 6.6b shows the combination degree standard deviation fit describing the distribution of spherical degree signal energy for the MSS signature. Additionally the fit for $n>360$ is computed to potential degree variances via $7\times10^{-22}n^{-4.55}$. It can also be seen from Fig. 6.6b that between degrees 2 and 30 an EGM96 model error, σ_n^e and an error fit, σ_n^{ef} are provided. In fact the fit σ_n^{ef} is used since the rather large discontinuity at $n=30$ between and σ_n^e and D_n is large enough to cause significant *ringing* with the subsequent ACV conversion to the frequency domain. The fit, σ_n^{ef} to the EGM96 potential degree

variances between degrees 2 and 30 is given by $2.5 \times 10^{-5} n^{-5.1}$.

Given this arrangement, $C_{h_0 h_0}$ is calculated using equation 6.23 over the globe at the same grid specifications as previously described (i.e., 0.075°). The spherical angle between two points is determined from a basic spherical triangle (*Todhunter* and *Leathem*, 1901), or

$$\psi = \cos^{-1}[\cos\phi' \cos\lambda'] \tag{6.25}$$

where, ϕ' and λ' are latitudinal and longitudinal co–ordinates referenced to a particular computation point.

The one dimensional normalised ACV is shown in Figure 6.7 for the EGM96 error, geoid error and reduced MSS signature. These show the various signal correlation lengths provided at the half normalisation point. The two dimensional plot over the globe using equation 6.23 is shown in Figure 6.8 (here a log magnitude is given in order to display the small signal contours of equal correlation.)

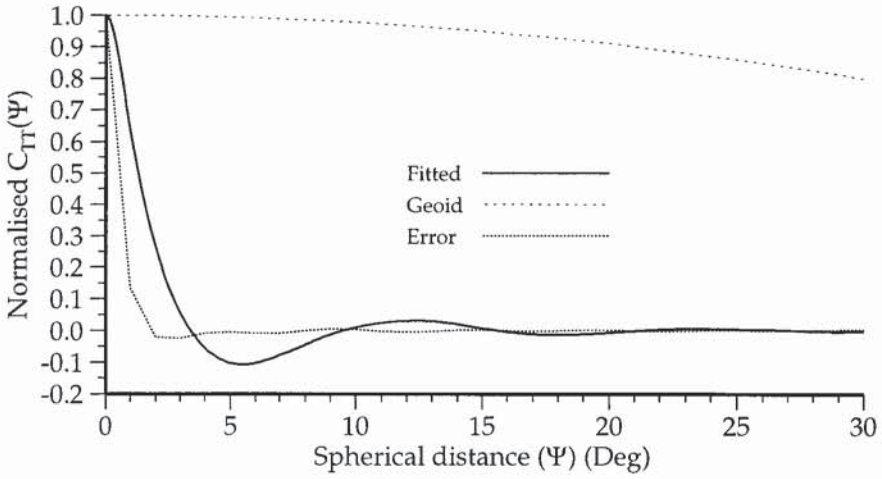

Figure 6.7: 1–dimensional auto–covariance function.

The power spectral density, $P_{h_0 h_0}$, can be simply computed using the FFT relationship given in equation 5.16. The perfect symmetry shown in Figure 6.8 means windowing is obsolete. However windowing is used in order to maintain consistency with other parameters. In the spectral domain, $P_{h_0 h_0}$, is almost entirely real due to FFT rounding errors resulting in a negligible ($< 10^{-18}$) imaginary component.

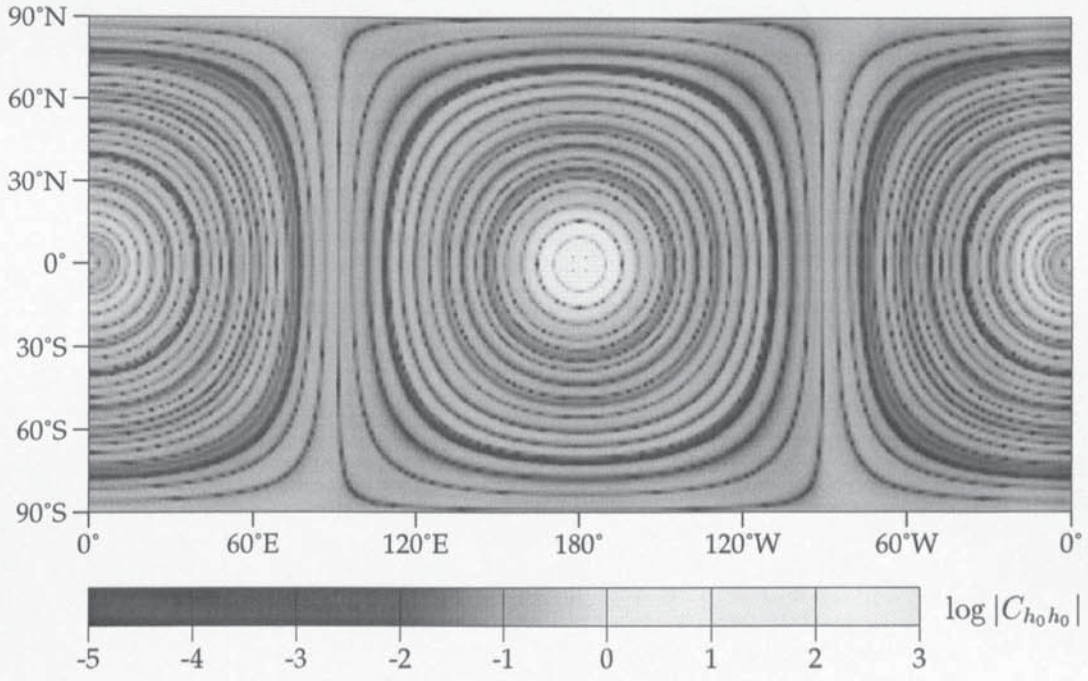

Figure 6.8: Gridded auto–covariance function, $C_{h_0 h_0}$.

6.4.2 Altimetric Error PSD, P_{nn}

Traditionally with spatial optimal interpolation a set of model covariance functions describing each of the major altimetric error sources would be used. Following *Wunsch* and *Zlotnicki* (1984), *Mazzega* and *Houry* (1989) and *Blanc* et al. (1990), covariance models are computed for radial orbit, instrumental, atmospheric propagation and oceanic variability errors. From these errors a total error ACV function, C_{nn} would be obtained. Studies that have used this procedure have been limited to small regions mainly due to computational requirements.

Unfortunately, at a high resolution over the globe the modelling of most of the covariance parameters is time consuming. In section 5.1.1 it was shown how the PSD of a function may be obtained either from its covariance or alternatively from the signal. Here, we investigate the use of altimetry to form the PSD of the errors resident within altimetric signal itself. The prospect of using altimetry for this is advantageous in terms of computation speed and in not having to rely on model covariances.

First of all a residual altimetric surface is computed by removing a 20 by 20 sea

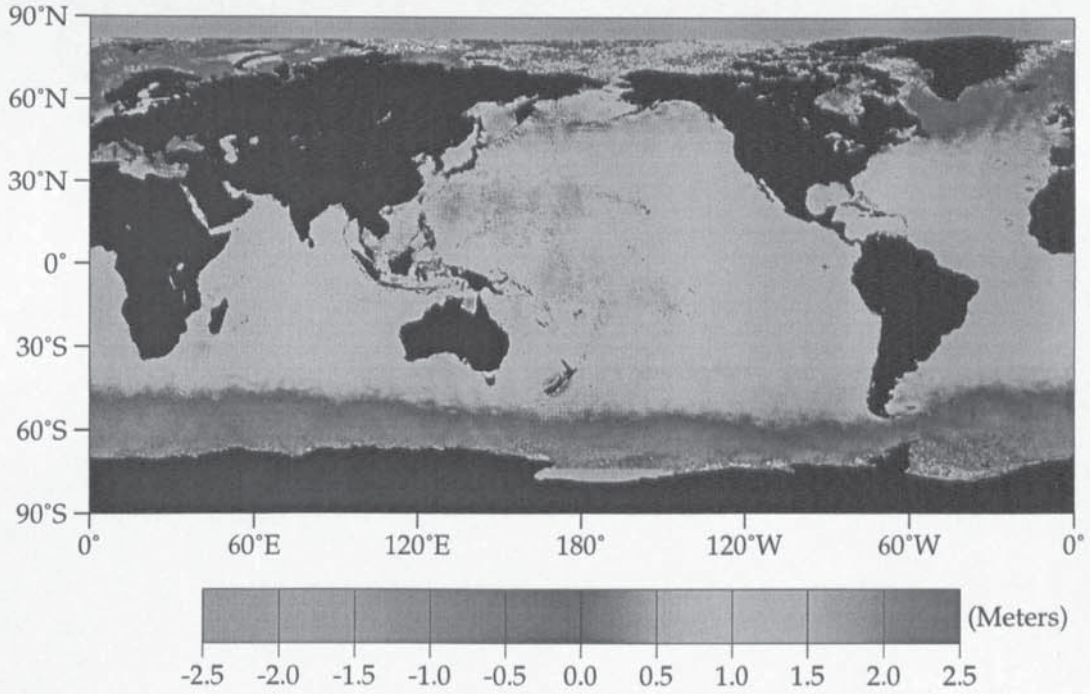

Figure 6.9: ERS-1 Geodetic Phase sea surface topography with RMS value of 0.65 meters.

surface topography, ζ_{20} and 360 by 360 degree geoid, N_{360}, from a first guess MSS.

$$S_r(\phi, \lambda) = M(\phi, \lambda) - N_{360}(\phi, \lambda) - \zeta_{20}(\phi, \lambda) \tag{6.26}$$

where, S_r is the residual surface and M the original gridded MSS. Removal of N_{360} from the MSS gives a measure of ERS-1 geodetic phase sea surface topography, see Figure 6.9 as displayed. Further removal of a sea surface topography model, ζ_{20} gives the residual surface S_r shown in Figure 6.10. This surface contains degree 2 to 360 EGM96 geoidal error, degree 1 to 20 EGM96 sea surface topography error and errors in all correction parameters (see chapter 4 and section 6.2 in this chapter.) Unfortunately the residual surface contains MSS power for degrees greater than 360; this problem will be dealt with shortly. There are some land/ice and water boundary points that resulted in values in excess of 50 cm. Removing these points was best achieved via the use of a Laplacian non–directional edge detector, i.e.,

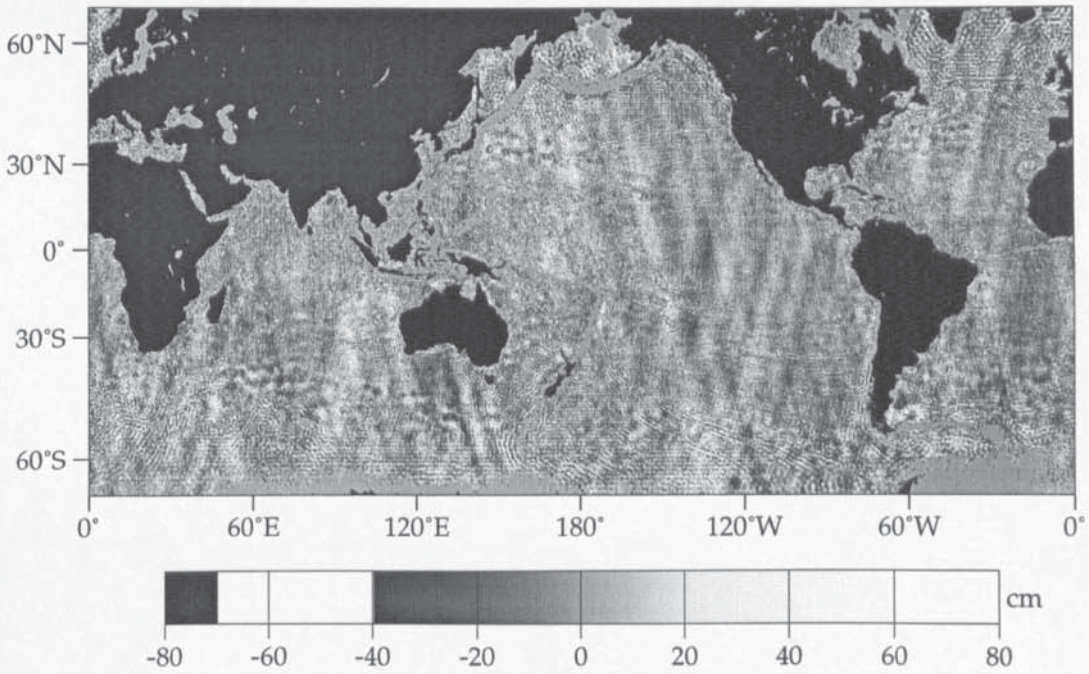

Figure 6.10: Residual ERS-1 Surface revealing familiar residual orbit error streaks and very small scale ($>$ 360 degrees) tectonic features. The RMS of this surface is 29 cm.

multiplication of S_r with the kernel

$$\begin{bmatrix} 0 & -1 & 0 \\ -1 & 4 & -1 \\ 0 & -1 & 0 \end{bmatrix}. \tag{6.27}$$

The resultant surface contains regions that may then be thresholded; this coped well with the removal of erroneous boundary points. Analysing Figure 6.10 it can be seen that low amplitude orbit streaks dominate the surface. A closer examination reveals residual short wavelength tectonic signatures are also visible.

The residual surface contains large land and ice based regions that cannot easily be filled. However, since the signal and therefore boundary discontinuities are small, the surface is transformed without any filling strategy.

The residual signal, S_r is converted to its equivalent PSD $P_{S_r S_r}$ via equation 5.15 after appropriate Hanning windowing between latitude degrees 82 and 75. Since, S_r is non–symmetric its Fourier transform is complex.

As mentioned earlier removal of EGM96 sea surface topography and geoid results

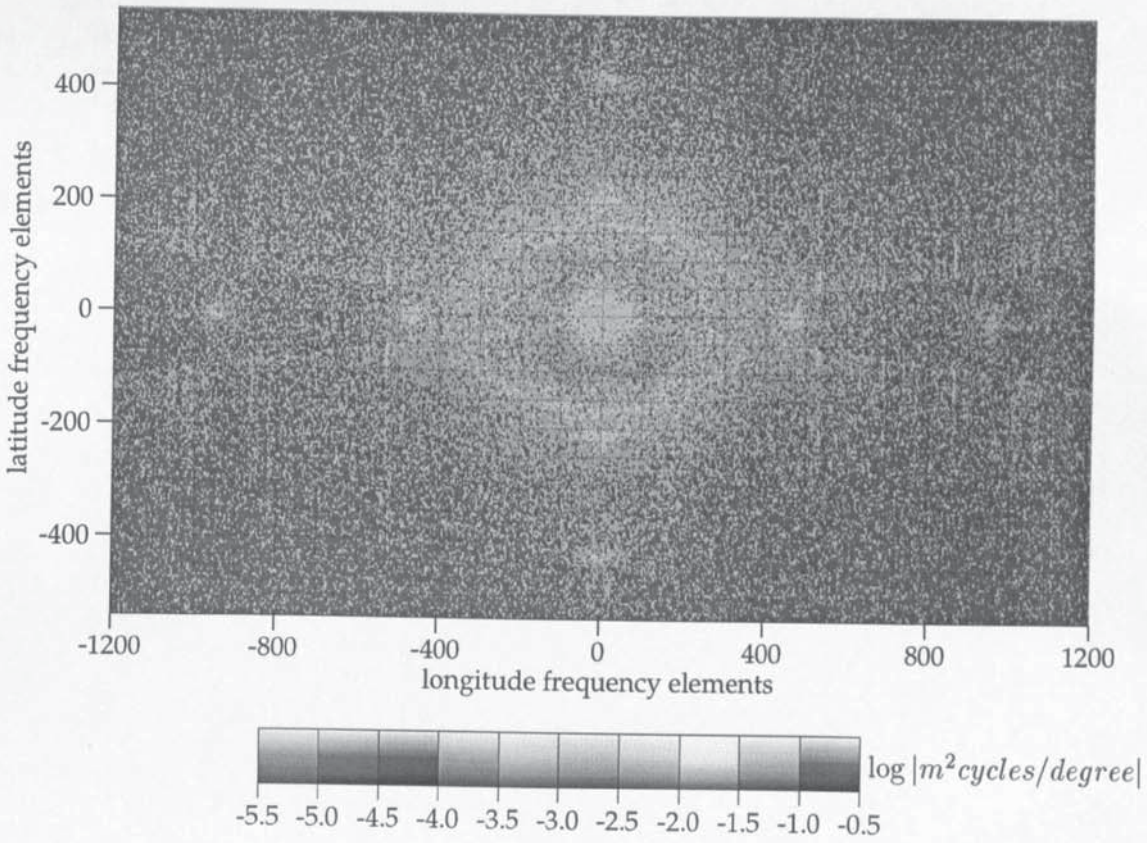

Figure 6.11: Spectrum of gridded residual ERS-1 surface.

in a complete high frequency sea surface signal. The final noise spectrum P_{nn} may therefore be obtained via a scaling of $P_{S_rS_r}$ above degree $n = 360$. Thus

$$P_{nn} = \begin{cases} P_{S_rS_r}, & 2 \leqslant n \leqslant 360 \\ P_{S_rS_r}/B, & n > 360 \end{cases} \tag{6.28}$$

where, B represents a scaling factor that was arbitrarily given a value of 10. A logarithmic plot of P_{nn} is shown in Figure 6.11. Here the residual radial orbit error is clearly seen as the oval shape surrounding the centre of the figure. Isolation of this feature in an inverse transformation recreates the orbit streaks seen in Figure 6.10.

6.4.3 Spectral Optimal Interpolation

Having defined each of the spectral parameters, P_{ss} and P_{nn}, the spectral least squares estimator, A_{sl}, may be computed. The spectral estimator is computed simply via the necessary addition and multiplication at each discrete frequency location. The optimally interpolated MSS may then be obtained from equation 6.16.

Here it must be noted that the reduced sea surface grid ($d_0 - h_{lw}$) will contain large land regions devoid of data creating large boundary discontinuities. Since the FFT procedure requires a complete data set it is necessary to fill any void regions such as with a degree 31 to 360 EGM96 derived geoid in the frequency domain. Additional filtering may be conducted to reduce any high frequency noise. This may be achieved by a cosine windowing function between the relevant frequencies. The resultant spectral surface is transformed to the spatial domain where the long wavelength EGM96 geoid and sea surface topography are added back. The RMS of the resultant surface is 35.3 m.

6.5 Validation

The optimally interpolated MSS with a re–established geoid (N_{30}) and sea surface topography (ζ_{20}) is presented in Figure 6.12. This figure displays both large basin scale features in addition to high power small scale features such as;

1. Subduction zones seen by the ocean trenches, see the Aleutian, and range of western Pacific trenches, for example.

2. Volcanic island chains, such as the Hawaiian island ridge assumed to be caused by mantle plumes and displaying the so called absolute motion of the lithosphere moving above the Asthenosphere over geological time scales.

3. The many sea–mounts as evidenced in the the Western Pacific.

Although just visible, one can make out some of the mid–ocean ridges. However, the removal of the high energy long wavelength components is required if any low energy small scale features are to resolved. This requires a truncated and cosine tapered long wavelength geoid model removal. An example of this will be given in chapter 8.

The MSS developed within this chapter did not contain TOPEX data and since TOPEX contains the most accurate sea heights to date it is reasonable to use this as an independent means of validating the MSS. There are approximately 33 T/P cycles within the ERS-1 geodetic phase. Fifteen TOPEX cycles were chosen beginning with cycle 58 and then every second cycle up to and including cycle 86.

Each TOPEX corrected sea surface height was retrieved and had sea–surface variability removed. The four surrounding MSS grid points were found and a comparison height was calculated via bi–linear interpolation. Differences were calculated and rejections made at threshold difference of 60 cm.

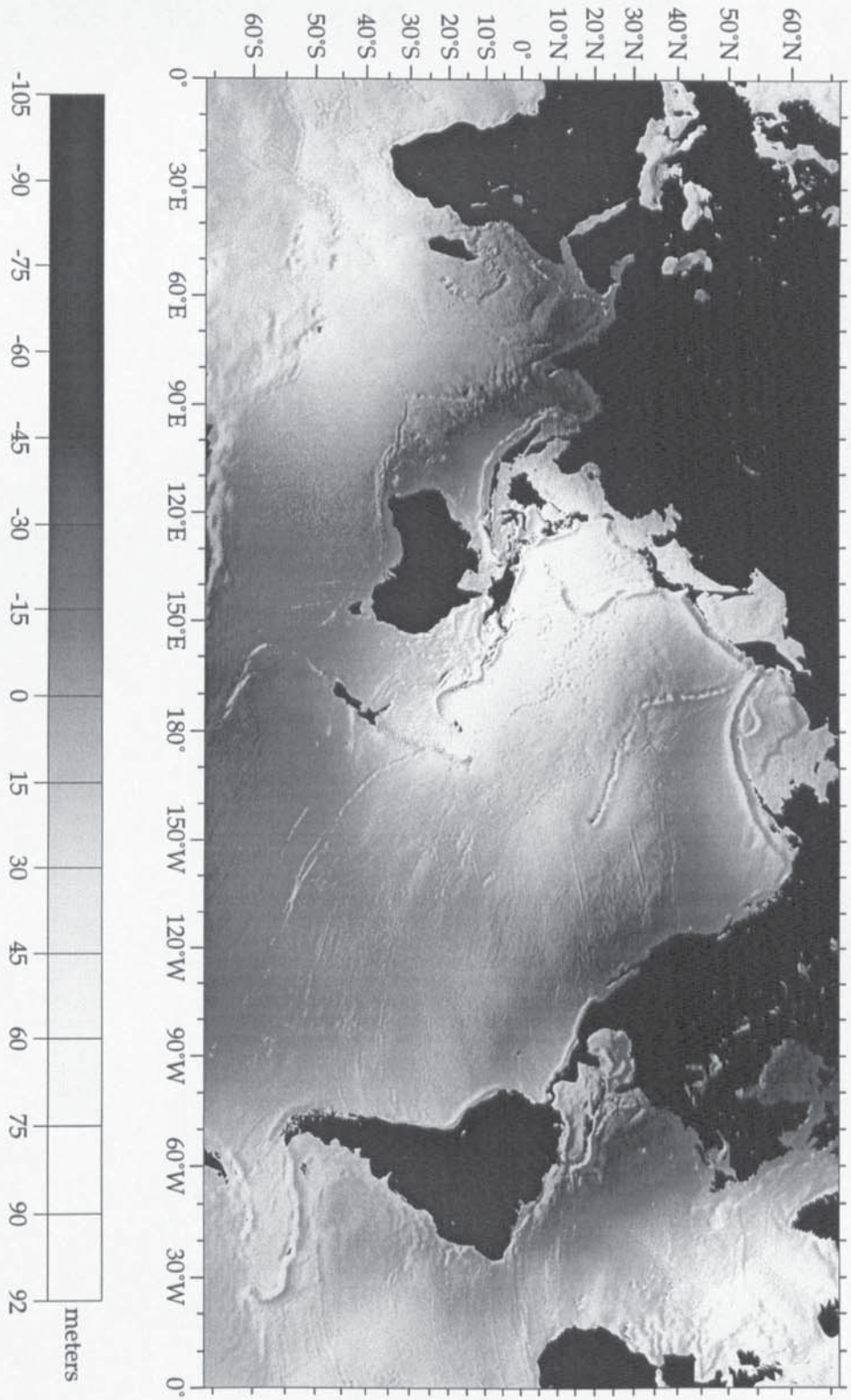

Figure 6.12: Global mean sea surface from ERS-1 geodetic phase data using a Mercator projection.

Table 6.2 contains the full set of results against TOPEX data. Comparisons are given for shallow (16.5–18.5 cm RMS), ocean (12.3–13.8 cm RMS) and for all data (12.7–14.1 cm RMS). For the un-optimally interpolated MSS a comparison (also

Table 6.2) for shallow (19.9–20.7 cm RMS), ocean (15.7–16.2 cm RMS) and for all data (15.8–16.5 cm RMS) was made. An improvement of the spectrally optimally interpolated MSS over the original has thus been made in the 3 to 4 cm range over all ocean types. An example of global comparisons between the optimally and un–optimally interpolated surfaces is given for cycle 66 in Figure 6.13. Here, an overall reduction in differences is evident between the two surfaces.

A comparison is also made to the original ERS-1 geodetic phase data. The data is corrected and radial orbit error and SSV reduced. The data is split into 9 sub–cycles of 37 days and a comparison is made as shown in Table 6.3. Here differences are between 10.1 and 10.3 cm RMS over all the cycles against ~14.5 cm RMS for the un–optimally interpolated surface. Against enhanced GEOSAT sea–heights (see Table 6.4) the model provided a bad fit. However considering the mis–modelling within the GEOSAT altimetry (i.e., orbital accuracy and lack of radiometer) the results are reasonably good. Comparisons show a model fit of ~18 cm RMS against ~22 cm for an un-optimally interpolated surface.

For completeness, a comparison with the EGM96 geoid plus sea–surface topography model gave an RMS comparison against TOPEX cycles of approximately 26.5–27.5 cm whilst for the OSU91A it was ~29 cm. Thus verifying an improvement between these two models.

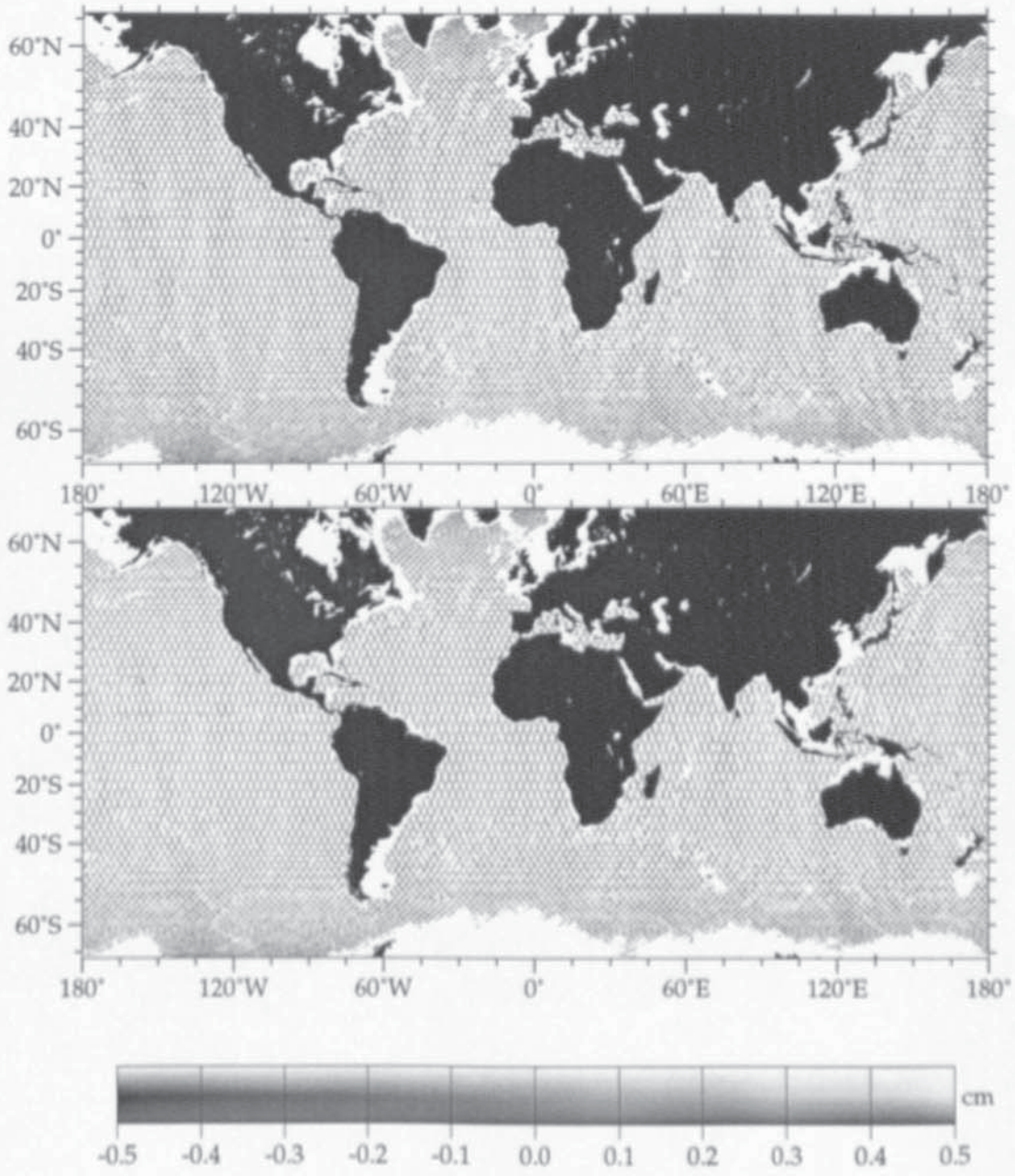

Figure 6.13: Comparison of the mean sea surface against TOPEX/Poseidon cycle 66 sea-surface heights (top) before optimal interpolation and (bottom) after optimal interpolation.

Cycle	Shallow Water				Ocean				Ocean and Shallow			
No.	No. of Points	No. of Rejections	σ_{oi} (cm)	σ_u	No. of Points	No. of Rejections	σ_{oi} (cm)	σ_u	No. of Points	No. of Rejections	σ_{oi} (cm)	σ_u
58	37978	5876	17.9	20.6	466854	19051	13.5	16.0	504832	24927	13.8	16.3
60	38870	6108	17.4	20.1	456290	14363	13.5	15.9	495159	20471	13.8	16.3
62	40635	6873	18.1	20.5	449658	12040	13.3	15.7	490293	18913	13.6	15.8
64	41919	7038	17.6	20.3	440646	9991	13.0	15.8	482565	17029	13.4	16.2
66	42959	7534	16.5	19.9	433848	8855	12.3	15.7	476807	16385	12.7	16.1
68	43721	8141	17.7	20.2	424169	7999	12.9	15.7	467890	16140	13.3	16.1
70	46456	9169	17.9	20.3	423010	7729	13.3	15.8	469466	16898	13.7	16.2
72	48632	9608	17.7	20.7	419016	7516	13.4	15.9	467648	17124	13.9	16.3
74	49552	10145	18.5	20.5	419456	7707	13.7	15.7	469008	17852	14.1	16.2
76	48465	9913	18.3	20.5	415101	7613	13.7	15.9	463566	17526	14.1	16.3
78	48660	9653	18.2	20.2	422631	7615	13.6	15.8	471291	17268	14.0	16.2
80	45536	8625	18.0	20.4	423357	8225	13.6	15.9	468893	16850	13.9	16.3
82	42306	6913	18.4	20.2	439551	10553	13.7	16.1	481857	17466	14.0	16.4
84	39316	6076	17.9	20.6	456689	15010	13.8	16.2	496005	21086	14.1	16.5
86	37802	6059	18.3	20.6	463180	18166	13.8	16.1	500982	24225	14.1	16.5

Table 6.2: Validation of optimally interpolated MSS against TOPEX altimetry. Comparison is made over shallow, ocean and for both, σ_{oi} and σ_u are RMS values for the optimally interpolated and original surfaces respectively.

	Shallow Water				Ocean				Ocean and Shallow			
Cyc. No.	No. of Points	No. of Rejections	σ_{oi} (cm)	σ_u	No. of Points	No. of Rejections	σ_{oi} (cm)	σ_u	No. of Points	No. of Rejections	σ_{oi} (cm)	σ_u
1	119077	8075	16.9	19.8	1427378	19983	9.3	14.1	1546455	38058	10.0	14.6
2	123960	18817	16.8	19.9	1423606	19930	9.4	14.0	1547566	38747	10.1	14.5
3	118936	18054	17.1	20.3	1365908	17756	9.3	14.1	1484844	35810	10.0	14.6
4	129162	19606	17.3	20.2	1406652	18286	9.5	14.3	1535814	37892	10.3	14.8
5	129549	19665	17.2	20.1	1407212	18293	9.6	14.2	1536761	37958	10.3	14.7
6	128989	19503	17.0	20.3	1415789	19821	9.5	14.2	1544778	39324	10.2	14.7
7	128569	19516	17.1	20.1	1426074	19965	9.4	14.1	1554643	39481	10.2	14.6
8	136218	20677	16.9	20.2	1499052	19487	9.4	14.0	1635270	40164	10.1	14.5
9	179127	27191	16.8	20.1	1928250	25067	9.4	13.9	2107377	52258	10.1	14.4

Table 6.3: Optimally interpolated and un–optimally interpolated MSS against 9 sub–cycles of ERS-1 geodetic phase altimetry.

	Shallow Water				Ocean				Ocean and Shallow			
Cyc. No.	No. of Points	No. of Rejections	σ_{oi} (cm)	σ_u	No. of Points	No. of Rejections	σ_{oi} (cm)	σ_u	No. of Points	No. of Rejections	σ_{oi} (cm)	σ_u
1	142469	23899	21.3	29.1	834650	70889	18.1	21.8	977119	94788	18.6	23.0
3	140209	21782	20.6	28.7	787400	54800	18.1	21.7	927609	76582	18.4	22.9
5	152311	25695	20.4	28.6	816324	47469	17.3	20.6	968635	73164	17.8	22.0
7	127765	22988	20.5	28.9	712288	39193	17.4	20.5	840083	62181	17.9	21.9
9	141123	25339	20.6	29.4	796941	43298	17.2	20.3	938064	68637	17.7	21.9
11	142695	25674	20.9	29.3	799649	47695	17.8	21.0	942344	73369	18.2	22.4
13	150149	29291	21.3	30.1	868745	71320	17.7	21.2	868745	100611	18.2	22.7
15	135992	26459	21.4	30.1	820440	75784	18.8	22.4	956432	102243	19.1	23.5
17	126827	22067	21.0	29.3	768265	68457	17.8	21.5	895092	90524	18.4	22.4
19	137735	22996	21.3	29.0	722095	52779	18.1	21.5	859830	75775	18.6	22.9
21	126370	21870	21.0	29.1	653579	41094	18.1	21.5	779949	62964	18.6	22.9
23	104340	21091	20.3	29.2	610020	34624	17.5	20.5	714360	55715	17.9	21.9

Table 6.4: Optimally interpolated and un–optimally interpolated MSS against 10 23–day sub–cycles of GEOSAT geodetic mission altimetry.

6.6 Conclusion

In this chapter the methodology used to determine a high resolution/precision MSS model has been described. In summary the procedure was as follows:

1. Minimise radial orbit error via the use of a modified *Le Traon* et al. cubic spline fitting to dual ERS-1 and TOPEX/Poseidon crossovers.

2. The removal of TOPEX derived sea surface variability in order to reduce cross–track gradients in the end product.

3. The gridding of the geodetic phase altimetric data set.

4. The spectral optimal interpolation procedure requiring the following

   - The generation of an auto–covariance function describing the MSS signature.
   - The generation of a surface describing altimetric errors (this has in the past been developed using covariance models of the major error contributing sources.)
   - The spectral transformation of the various components described by equation 6.16 using FFT techniques introduced in chapter 5.
   - Inverse transformation resulting in the production of the final surface.

In comparison to other recent MSS models, such as those described by *Kim* (1993), *Yi* (1995) and *Cazenave* et al. (1995), all show comparisons with T/P in the region of 9.5–13 cm RMS. All these models however, contain a years worth of TOPEX data and therefore have an advantage when compared against the same data. Thus, although such models may be good, off the T/P ground–track there is no actual means of assessing this in terms of their performance along–track. Inclusion of stacked TOPEX 10 and ERS-1 35 day repeat altimetry into the model described here would almost certainly yield further improvements. Additionally, a study concerning how the altimetric error surface compares with model covariances describing the altimetric error would be useful. Here, covariances determined empirically from the altimetry could help improve modelling and vice–versa.

Chapter 7

Gravity Anomalies from Enhanced GEOSAT Sea Surface Heights

7.1 Introduction

In chapters 1 and 2 the case to improve mean sea surface models was advanced. Such improvements essentially require that both existing and future altimetry sea surface heights are integrated into a combined mean sea surface solution. Here a procedure is developed for the integration of the newly released (August 1997) enhanced GEOSAT geodetic mission data (*Cheney*, 1997b) into the optimally interpolated ERS-1 MSS model constructed in chapter 6.

Combining the two satellite altimetric data types however is complex. Substantial errors still remain both within the GEOSAT ephemeris and wet tropospheric models despite the respective computation of orbits using the JGM3 gravity field and the re–analysis data tropospheric water vapour.

The procedure developed here for mean sea surface model integration is presented in two chapters:-

1. This chapter deals with the reduction of long wavelength radial orbit error within the GEOSAT ephemeris. This allows for the development of a global gravity anomaly field. The method adopted is a variation on the *McAdoo* and *Marks* (1992) methodology. This procedure reduces radial orbit error via the computation of along–track altimetric slopes. Slopes are then converted to north and east deflections of the vertical (see Figure 7.1 for a schematic) and then to the gravity anomaly field via the use of FFT techniques described

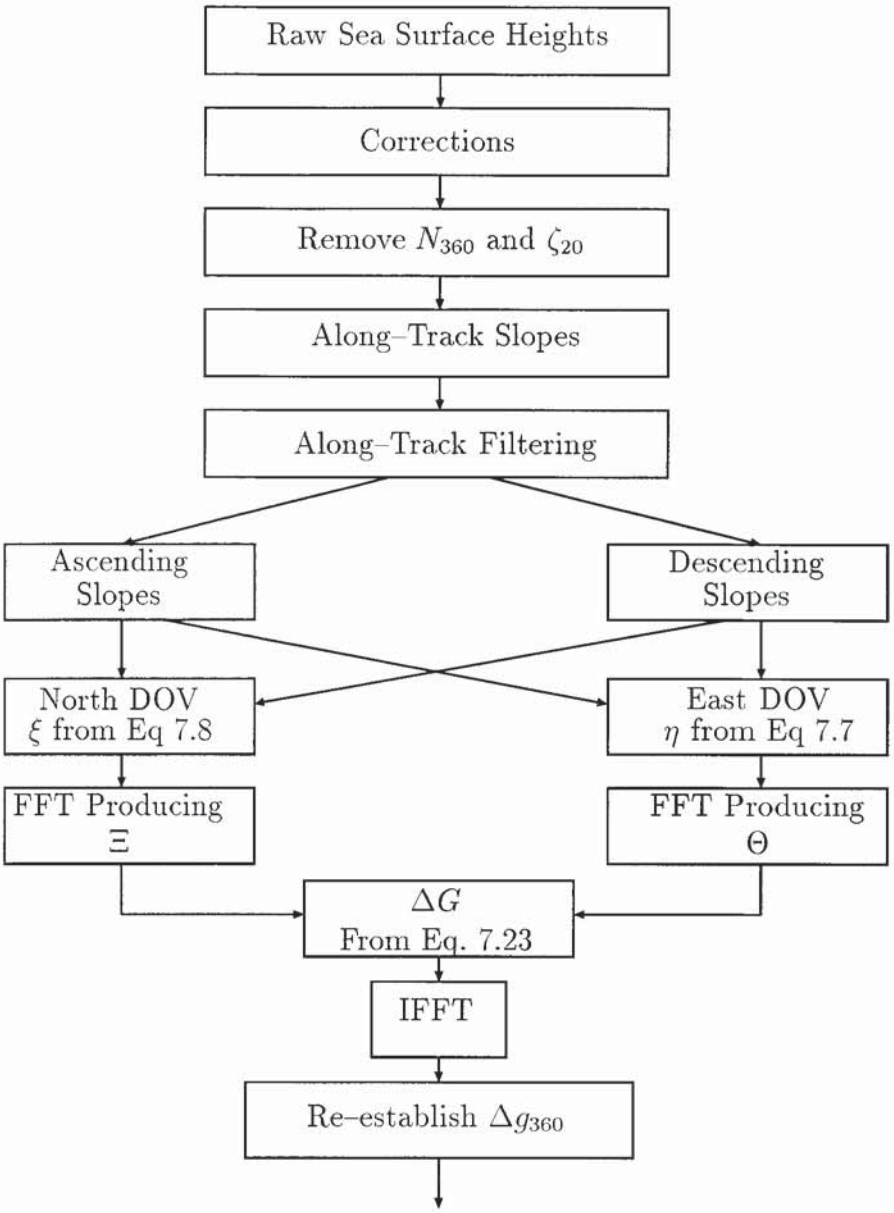

Figure 7.1: Schematic diagram showing procedure allowing global gravity anomaly field to be determined.

in section 5.3. Since the improved GEOSAT altimetry is used this serves as an opportunity to present a new gravity anomaly model with a standard contemporary technique.

2. Chapter 8 deals with conversion of the gravity anomaly field to a MSS for integration within the optimally interpolated ERS-1 MSS. Since the gravity anomaly field is used it essentially allows for the possible inclusion of shipboard or terrestrially collected gravity data at a future date.

Gravity anomaly field processing was explained in a complete form by *Heiska-*

nen and *Moritz* (1967). Their study described a wide range of historical methods prior to its date of publication. Since then there have been a number of investigations describing the generation of the field via non–FFT methods typically; *Moritz* (1980), *Mazzega* and *Houry* (1989) and *Rapp* and *Pavlis* (1990).

More relevant to the study carried out here is the use of fast Fourier transform utilities. Early gravity anomaly techniques using the FFT were developed by *Haxby* et al. (1983) and expanded upon by *Sandwell* and *McAdoo* (1990), *McAdoo* (1990) and *Small* and *Sandwell* (1992). More recently with the use of high resolution data (GEOSAT and ERS-1) procedures have been refined. There are numerous examples of these such as; *Sandwell* (1992), *McAdoo* and *Marks* (1992), *Hwang* and *Parsons* (1995), *Anderson* and *Knudsen* (1995), *Hwang* and *Parsons* (1996). Also gravity fields have been produced around the ERS-1 latitudinal extremities using the *McAdoo* and *Marks* methodology (see *Laxon* and *McAdoo* (1994) and *McAdoo* and *Laxon* (1997).)

7.2 Data Pre–Processing

The U.S. Navy's GEOSAT (GEOdetic SATellite) was launched on March 12 1985 and placed into a drifting orbit for approximately 18 months. This geodetic mission (GM) commenced on March 30th 1985 and ended on September 30th 1986 producing some 30 million ocean/shallow water observation data.

The data was originally classified during the later stages of the cold war. However a series of data de–classification began in 1991 and ended on 22nd June 1995. Unfortunately, the original GDR's contained highly inaccurate modelling of orbital ephemeris, ionospheric and wet tropospheric corrections in addition to the poorer modelling of tides, sea state bias, etc., due to the incomplete knowledge of their phenomena. A description of the original GDR's can be found in *Cheney* et al. (1991).

In Summer 1997 an upgrade of the GEOSAT data was released; this is described by *Cheney* (1997b) and also on an online publication *Cheney* (1997c). The data sets main features include:

- Re–computed orbits (*Williamson* and *Nerem*, 1994) using the JGM3 gravity field *Tapley* et al. (1996). These orbits are claimed to be an improvement by a factor 10 with reference to those computed by Naval Surface Weapons Center (NSWC) on the original geophysical data records *Cheney* (1997a).

- The use of the International Reference Ionosphere IRI95 rather than the out-

dated Bent model *Bent* et al. (1975).

- An upgraded wet tropospheric correction from a 40 year re–analysis of water vapour *Kalnay* (1996).

The 549 days (~18 months) of GDR's were initially corrected for

1. Solid Earth, ocean, ocean loading and pole tides.
2. Wet and dry tropospheric pulse slowing effect.
3. Sea state bias provide by a four parameter model (see *Gaspar* et al. (1996)) sea–surface effects.
4. Ultra–stable oscillator drift and internal calibration.
5. Globally averaged inverse barometer effect applied at 6 hourly intervals.

Data was rejected in the circumstances that

1. Data was land flagged.
2. Sea–surface heights disagreed by 5 meters with a reference Ohio State University MSS supplied on the GDR's (see *Yi* (1995), *Rapp* and *Nerem* (1995) and *Rapp* (1997)).
3. The 10 per–second sea heights had a standard deviation greater than 25 cm.
4. No wet tropospheric model correction was available. There are two model corrections supplied on the GDR's namely the National Centers for Environmental Prediction (NCEP) and NASA Water Vapour Project (NVAP).
5. No dry tropospheric model (again there are two – NCEP and ECMWF) provided a correction.
6. Sea–State Bias and Wind Speed flags were set as invalid.
7. The ionospheric model could not provide a correction.
8. Either of the three (x,y,z) attitude flags *Lillibridge* (1997) were set. The three flags represent the state of antenna pointing and thus illumination angle of the footprint. GEOSAT was designed with a gravity gradient stabilisation system in the form of a boom. *Cheney* et al. (1991) attributes large data loss due to the effect of solar radiation pressure on this mechanism.
9. Significant wave heights were greater than 25 meters.

7.3 The Global Gravity Anomaly Field

Following the preliminary correcting and rejection of altimetry the complex process of developing the gravity anomaly field can commence. Figure 7.1 displays the procedure schematically that is now explained.

Sea surface heights have a combined EGM96 geoid to degree and order 360, N_{360}, and sea surface topography to degree and order 20, ζ_{20} removed. This removal facilitates the need to process data on a flat Earth as described by the gravity anomaly formulation in section 5.3. Following *Sandwell* (1984) the predominant long wavelength once and twice per revolution radial orbit error resident within GEOSAT sea heights is reduced via the computation of along track slopes. An example of a sea height profile and its corresponding along track deflection of the vertical is shown in Figure 7.2. The along track deflection of the vertical measured in μradians is calculated via first differences using the formula

$$\frac{\partial N}{\partial s} \equiv N' = \frac{h_i - h_{i-1}}{\Delta s} \tag{7.1}$$

where,

N, is the geoid height,
Δs, the along track distance,
N', the along track slope,
i, is the measurement index, and
h, the sea height.

The along track deflection of the vertical, see Figure 7.5, d_a is then simply

$$d_a = \tan^{-1} N' \tag{7.2}$$

However since the deflection angles are very small then d_a is approximated such that

$$d_a \simeq N'. \tag{7.3}$$

Unfortunately, along track slopes, whilst accentuating small scale tectonic features also amplify high frequency noise components. Therefore the production of slope profiles require filtering. This may be achieved by a simple Gaussian low–pass filtering function with the resultant effect being shown for a single profile in Figure 7.2b. The filtered signal is achieved via the convolution of the raw signal with

the kernel $e^{-t^2/2}$, with t being the time difference between altimeter measurements. This is the same filtering technique described by *McAdoo* and *Marks* (1992) and *Sandwell* (1992).

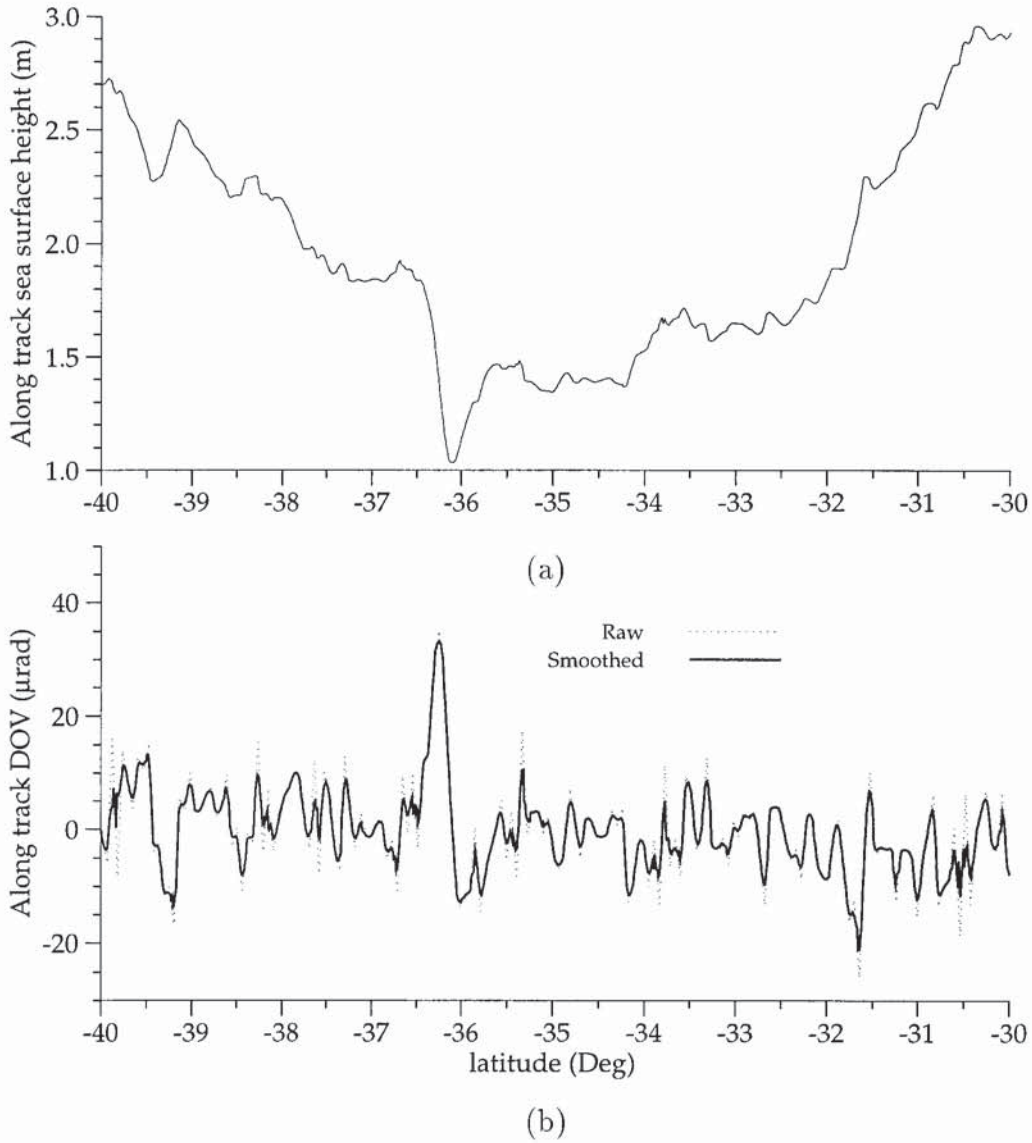

Figure 7.2: Conversion of (a) along–track sea–surface heights to (b) smoothed along–track deflections of the vertical.

The smoothed slopes are finally gridded using a similar method as that described in chapter 6. Here slopes are gridded into separate ascending and descending data sets necessary for the determination of deflection of the vertical components.

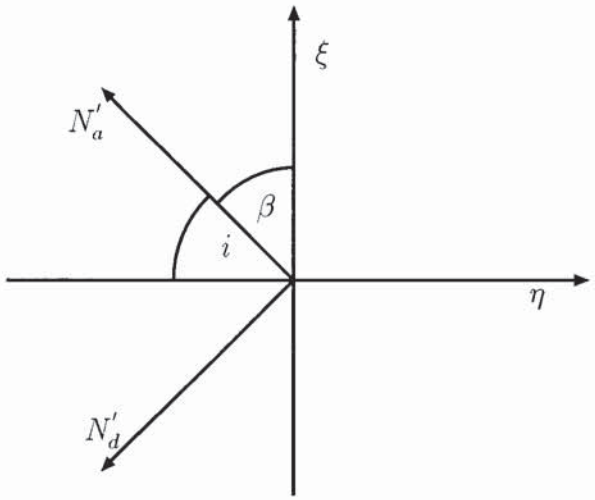

Figure 7.3: Diagram showing ascending and descending slopes, N'_a and N'_d

7.3.1 Generation of the Vertical Deflections, η and ξ

Here a description is given of how northern, ξ, and eastern, η, deflection of the vertical components may be determined from the ascending and descending deflection grids. We refer to the respective along–track ascending and descending gridded slopes by

$$\begin{aligned} N'_a &\equiv (\partial N/\partial s)_a \\ N'_d &\equiv (\partial N/\partial s)_d. \end{aligned} \tag{7.4}$$

With reference to Figure 7.3 it may now be seen that each of these components can be determined with respect to an azimuth angle, β. This angle will be different at each grid point and defines how the slopes may be converted to vertical deflections. Thus,

$$N'_a = -\frac{\partial N}{\partial x}\sin\beta + \frac{\partial N}{\partial y}\cos\beta \tag{7.5}$$

and

$$N'_d = -\frac{\partial N}{\partial x}\sin\beta - \frac{\partial N}{\partial y}\cos\beta. \tag{7.6}$$

Now solving equations 7.5 and 7.6 for $\partial N/\partial y$ and $\partial N/\partial x$ gives the respective DOV components, ξ and η, i.e.,

$$\xi \simeq \frac{\partial N}{\partial y} = -\left(\frac{-N'_a + N'_d}{2\cos\beta}\right) \tag{7.7}$$

and

$$\eta \simeq \frac{\partial N}{\partial x} = -\left(\frac{N'_a + N'_d}{2\sin\beta}\right) \tag{7.8}$$

What remains is the method required to compute the azimuth angle, β.

Following *Parke* et al. (1987), β is ultimately computed by considering both rotation velocity at the Earth's surface and that of the ground projected satellite velocity vector. This case will be dealt with in a moment after discussing the case on a non–rotating Earth.

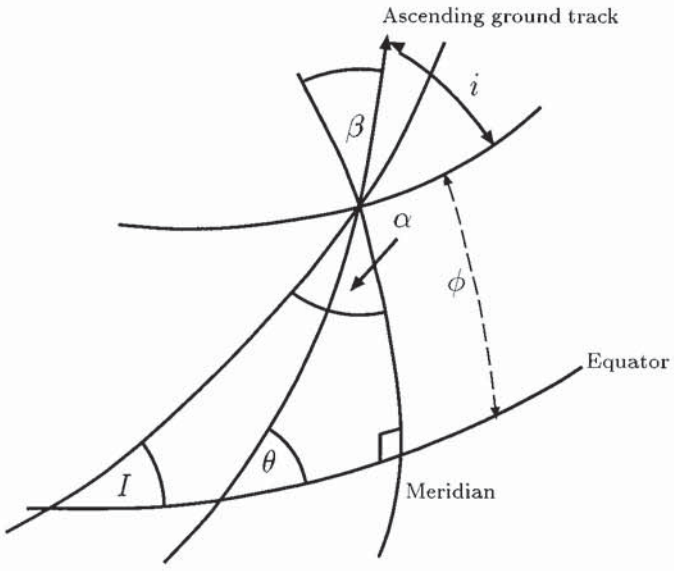

Figure 7.4: The inclination angle I, latitude ϕ and azimuth angles on a non–rotating Earth, α, and azimuth angle on a rotating Earth, β. This diagram represents prograde satellite motion.

From the use of spherical trigonometry theory (*Todhunter* and *Leathem*, 1901) the relationship regarding three angles, A, B and C and a side a is given by

$$\cos A = -\cos B \cos C + \sin B \sin C \cos a \tag{7.9}$$

From Figure 7.4 we relate these angles such that $A = I$, $B = 90°$, $C = \alpha$ and

$a = \phi$. Equation 7.9 simply reduces to

$$\sin \alpha = \frac{\cos I}{\cos \phi} \tag{7.10}$$

Thus at the equator, $\alpha = I$, whilst at the latitudinal extremity ($\phi = |180° - I|$ in the case of a retrograde platform) $\alpha = 90°$.

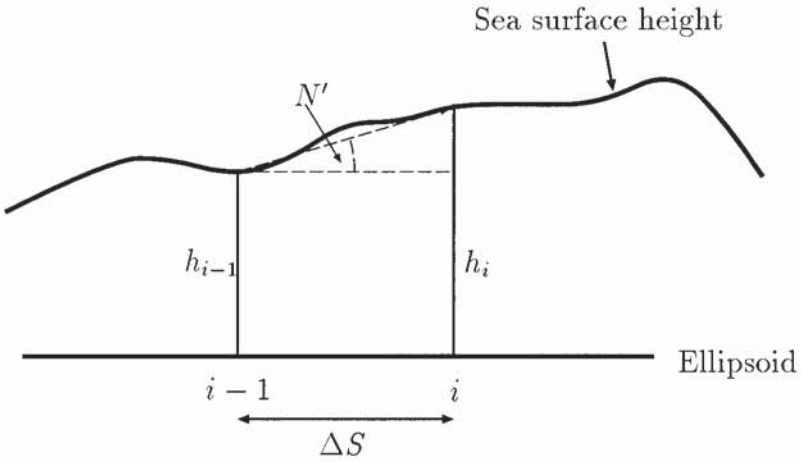

Figure 7.5: Schematic computation of along track deflection of the vertical.

Referring back to a rotating Earth, it can be seen from Figure 7.4 that α is greater than β at latitudes other than the equator and the latitudinal extremities (note that for a prograde satellite β would be increased.)

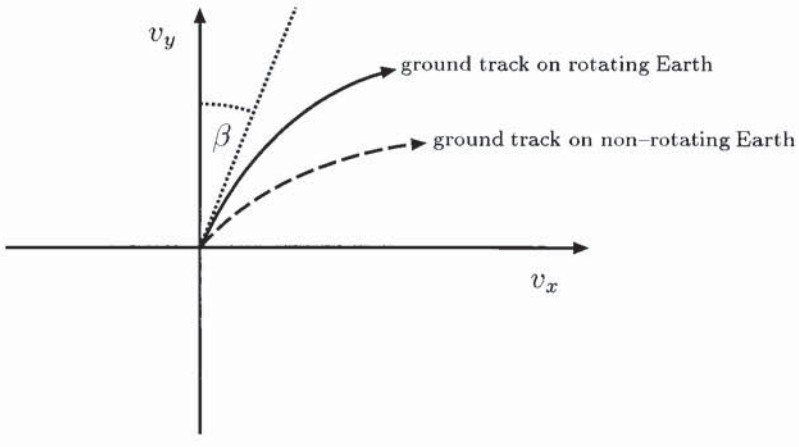

Figure 7.6: Azimuth angle, β and ground–track velocity, v_s, as a function of x and y velocities, v_x and v_y

Due to the relative rotation of the Earth and satellite the azimuth angle, β, may be determined via the calculation of ground–track component velocities v_x and v_y.

From Figure 7.6 it can be seen that β is given by

$$\beta = \tan^{-1}\left(\frac{v_x}{v_y}\right). \tag{7.11}$$

v_x consists of the addition (retrograde satellite motion) or subtraction (prograde motion) of the x components of the satellite and rotating Earth velocities at the given latitude ϕ. These are

1. $\mathbf{v_s}$, the satellites velocity vector projected onto the Earth's surface. This vector subtends an angle α from the parallel and has a magnitude v_s given by

$$v_s = R_e\sqrt{\frac{\mu_e}{a^3}} \tag{7.12}$$

where, $\mu_e = 3.986030 \times 10^5$ km^{2}s^{-2} is the gravitational constant multiplied by the Earth's mass. Thus the component of $\mathbf{v_s}$ in the x direction is given by

$$v_s \sin\alpha. \tag{7.13}$$

2. $\mathbf{v_e}$, the Earth's eastward rotational surface velocity at the equator. This results with a x component velocity at a latitude ϕ of

$$v_e \cos\phi. \tag{7.14}$$

Since $v_e = |\mathbf{v_e}|$.

Thus in the case of GEOSAT, a retrograde platform, v_x will be

$$v_x = v_s \sin\alpha + v_e \cos\phi, \tag{7.15}$$

whilst the y component velocity vector v_y is simply

$$v_y = v_s \cos\alpha. \tag{7.16}$$

Hence substituting equations 7.15 and 7.16 into 7.11 and re–arranging yields β, such that

$$\beta = \tan^{-1}\left[\tan\alpha + \frac{v_e \cos\phi}{v_s \cos\alpha}\right]. \tag{7.17}$$

Additionally, v_e may be expanded to deal with further parameters. Here,

$$v_e = R_e(\dot{\theta} - \dot{\Omega}), \tag{7.18}$$

where the components are the inertial sidereal rotation rate of the Earth, $\dot{\theta}$ and the precession rate of the satellites line of nodes, $\dot{\Omega}$. Equation 7.17 therefore becomes

$$\beta = \tan^{-1}\left[\tan\alpha + \frac{R_e(\dot{\theta} - \dot{\Omega})\cos\phi}{v_s \cos\alpha}\right]. \tag{7.19}$$

In contrast to the above method, *McAdoo* and *Marks* (1992) refers to the computation of deflection components via the use of the inclination angle, i, see Figure 7.3. Here, equation 7.19 may be quite easily re-arranged to give

$$i = \frac{\pi}{2} - \beta = \tan^{-1}\left[\frac{\tan i'}{1 + \frac{(\dot{\theta}-\dot{\Omega})\cos\phi}{v_s \cos i'}}\right] \tag{7.20}$$

where i if measured in radians is given by $i' = \pi/2 - \alpha$.

Thus considering equation 7.19, the value of β may now be determined from the Earth's mean radius ($R_e = 6370 \times 10^3$ m), its sidereal rotation rate ($\dot{\theta} = 7.292115 \times 10^{-3}$ rads^{-1}) and the three satellite dependent parameters (α, v_s and $\dot{\Omega}$.) α and v_s are computed from equations 7.10 and 7.12, whilst $\dot{\Omega}$ which is satellite dependent in the sense of the platforms geocentric mean height a and orbital inclination, may be computed from

$$\dot{\Omega} \simeq \frac{3C_{20}}{2}\sqrt{\frac{\mu_e}{a^3}}\left[\frac{R_e}{a^2(1-e^2)}\right]^2 \cos I \qquad \text{rad s}^{-1} \tag{7.21}$$

where, C_{20} is the largest harmonic coefficient representative of the oblateness of the Earth (see section 2.2.3). The orbital eccentricity e is small ($e \sim 0.001$); a requirement for altimetric accuracy. Equation 7.21 is an approximation since only the largest harmonic coefficient is represented. It may be further approximated ($e \simeq 0$) (see *Parke* et al., 1987) to give.

$$\dot{\Omega} \simeq -4.17 \times 10^7 a^{-7/2} \cos I \tag{7.22}$$

here, a is computed in kilometers. The required satellite dependent parameters for GEOSAT, ERS-1 and TOPEX/Poseidon are given in table 7.1.

The way that β and α vary for GEOSAT is displayed in Figure 7.7a. Here we

Platform	Inclination	Mean height	$\dot{\Omega}$	$\lvert\mathbf{v_s}\rvert$
	I°	km	rad s^{-1}	m s^{-1}
GEOSAT	108.058	800	4.144×10^{-7}	6627
ERS-1	98.549	760	2.03×10^{-7}	6679
T/P	66.010	1330	-4.232×10^{-7}	5952

Table 7.1: Orbital characteristics relevant for vertical deflection computation for GEOSAT, ERS-1 and TOPEX/Poseidon.

see the maximum difference between the two parameters occurs at the equator. Alternatively β is displayed for both GEOSAT and ERS-1 in Figure 7.7b showing the larger variation for ERS-1 due to its greater inclination angle.

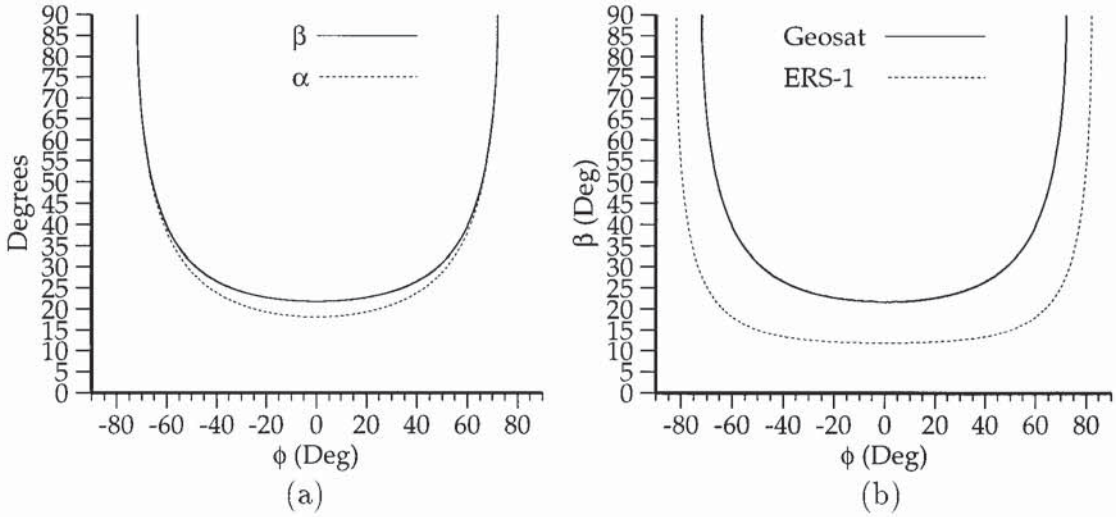

Figure 7.7: (a) GEOSAT parameters β and α over all latitudes and (b) β displayed for GEOSAT in comparison to ERS-1 showing essentially the heading for each platform.

The northern ξ and eastern η vertical deflections may now be computed at each grid point. Equations 7.8 and 7.7 are used for this and require the respective along track ascending and descending deflections determined earlier.

However, we see the fundamental problem with this methodology when, in the first instance, ξ is computed at the latitude extremity. Here, $\beta = 90°$ and thus $\xi \longrightarrow \infty$ as can be seen Figure 7.7a. If $1/\cos\beta$ is plotted against ϕ (shown in Figure 7.8a) we see the sudden large increase in the few degrees at the latitudinal extremity. Ultimately this means that the northern component is impossible to resolve in such regions. However, since the few degrees the region covers is windowed for

FFT usage the singularity is not a major problem. In Figure 7.8a $1/2\cos\beta$ is also plotted for ERS-1. Here we see that the use of a platform with a higher inclination will facilitate in gravity anomaly determination providing a suitable weighting is used.

Likewise using equation 7.8 and the coefficient $1/2\sin\beta$ we see in Figure 7.8b that the eastern DOV component is poorly resolved at the equator. In this case there is a component available and so η does not tend to infinity. Essentially, η will be more noisy at the equator. Once again, however, we see that the addition of a low inclination satellite would help improve the computation of η if the gravity anomaly is being determined from a high inclination satellite. Thus it can be shown that the use of two satellites with differing orbital planes would facilitate gravity field recovery. This is also a fundamental problem in gradiometry.

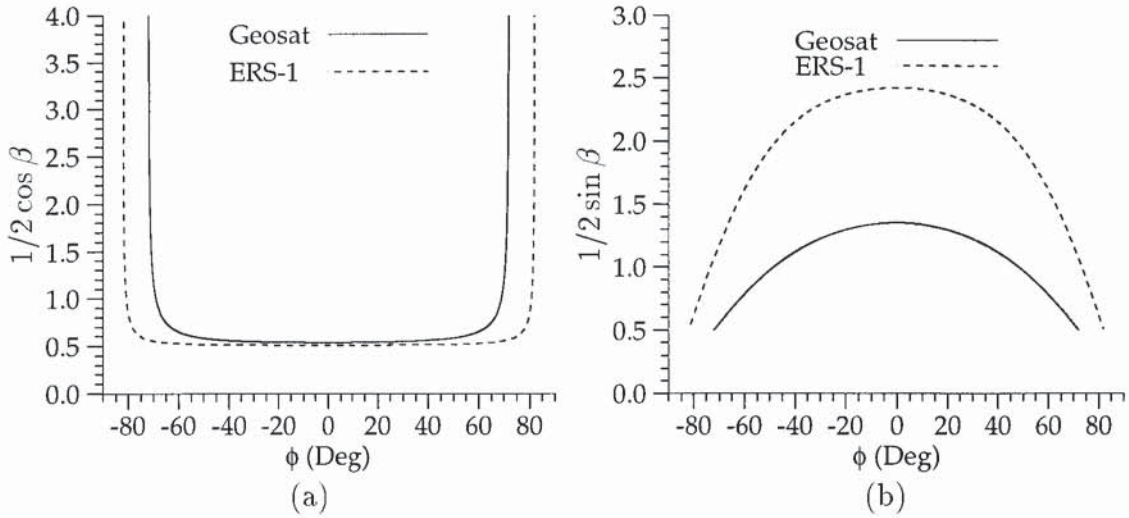

Figure 7.8: For retrograde platforms GEOSAT and ERS-1 (a) Coefficient $1/2\cos\beta$ (see equation 7.7) displaying the ξ singularity as $\beta \longrightarrow 90°$ ($\phi = I$). (b) Coefficient $1/2\sin\beta$ showing that for a lower inclination angle the peak in this coefficient is smaller at $\phi = 0°$.

Northern and eastern gridded DOV components are displayed in Figures 7.9 and 7.10. Here a particular region in the South Indian ocean has been chosen to display a range of features. The northern component enhances features in the east–west direction whilst the eastern component enhances north–south features. This effect may be particularly observed by examining the ninety–east ridge that protrudes to the north within the two figures. Here it is clearly defined by eastern vertical deflections though barely distinguishable by northern deflections.

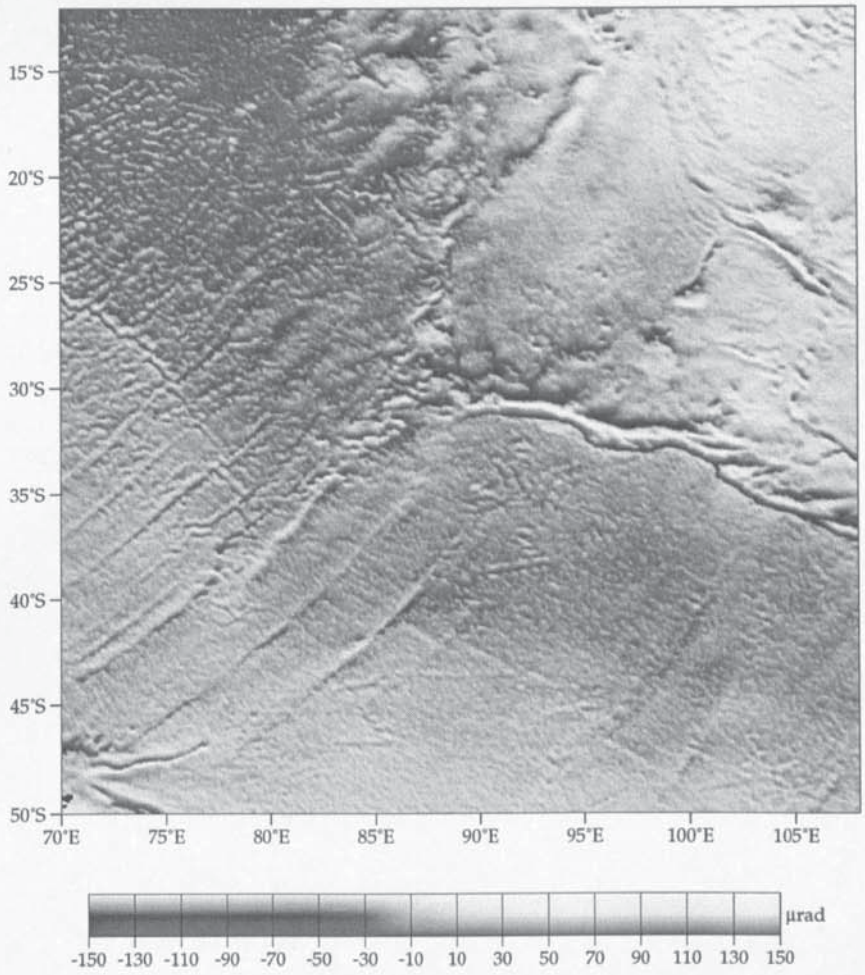

Figure 7.9: Northern gridded vertical deflection in the southern Indian ocean.

7.3.2 Construction of Gravity Anomalies

The construction of the gravity anomaly field is achieved via equation (5.57) developed in section 5.3.3. For convenience this equation is

$$\Delta G(u,v) = \frac{\imath\gamma\,(u\Theta + v\Xi)}{\sqrt{u^2+v^2}} \tag{7.23}$$

where,

$\Delta G(u,v)$,	is the spectral gravity anomaly field,
γ,	is the normal gravity,
Θ,	Fourier transform of η,
Ξ,	Fourier transform of ξ,
u, v,	spatial frequencies.

Θ and Ξ are computed from η and ξ and Hanning windowed over 5° of the latitudinal extremities, as described in chapter 5. After the computation of equation 7.23 a further low pass filter is applied to ΔG and the inverse Fourier transform is computed. The resultant gravity anomaly has the original long wavelength gravity anomaly model added back. The gravity anomaly model is computed from a spherical harmonic representation of the anomalous potential T, namely

$$T(\theta, \lambda, r) = \frac{\mu_e}{r} \sum_{n=2}^{n_{max}} \left(\frac{R_e}{r} \right)^n \sum_{m=0}^{n} [\hat{C}_{nm} \cos m\lambda + \hat{S}_{nm} \sin m\lambda] P_{nm}(\cos \theta) \quad (7.24)$$

Where,

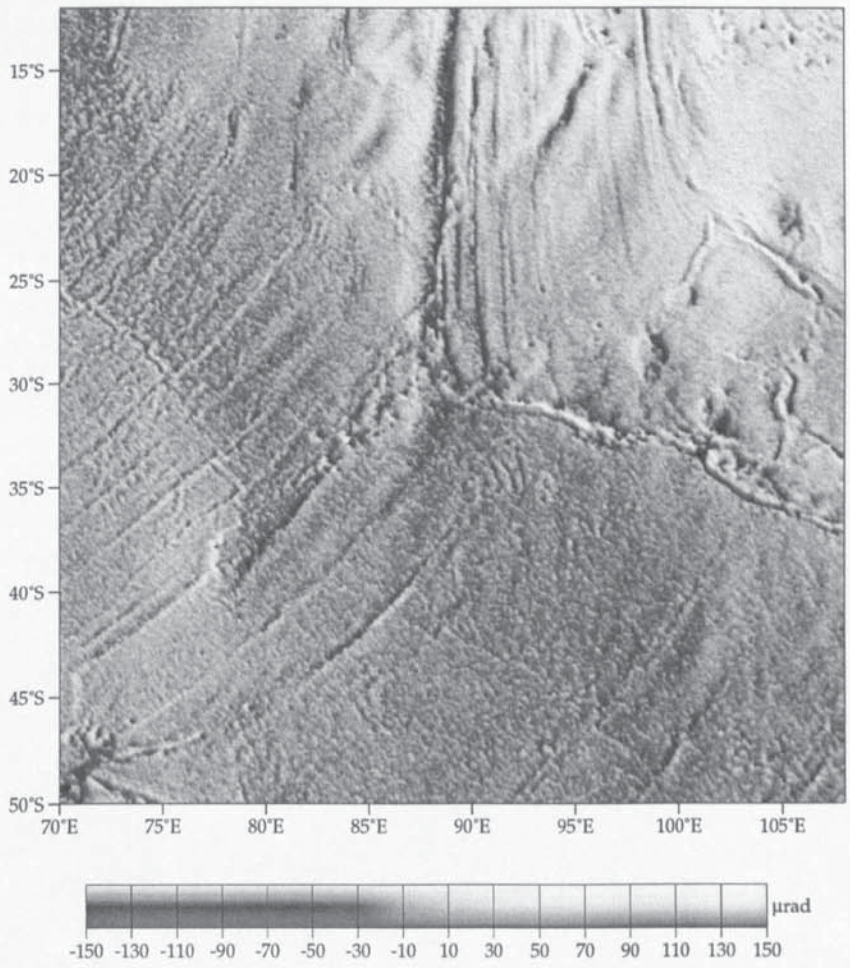

Figure 7.10: Eastern vertical deflection component in the southern Indian ocean.

r,	is the geocentric radial distance,
θ, λ,	latitude, longitude,
n, m,	degree and order,
n_{max},	maximum degree,
P_{nm},	Legendre polynomials,
$\hat{C}_{nm}$ and $\hat{S}_{nm}$,	are the differences between harmonics of the actual Earth and those of an equipotential ellipsoid.

Following *Heiskanen* and *Moritz* (1967) the relationship between gravity anomaly, Δg, and anomalous potential, T is

$$\Delta g(r) = -\frac{\partial T}{\partial r} - \frac{2}{r}T. \tag{7.25}$$

The spherical harmonic function for the computation of the gravity anomaly can therefore be determined from equation 7.25 (see appendix B.1) to give Δg on the geoid ($r = R_e$), or

$$\Delta g(\theta, \lambda) = \frac{\mu_e}{R_e^2} \sum_{n=2}^{n_{max}} (n-1) \sum_{m=0}^{n} [\hat{C}_{nm} \cos m\lambda + \hat{S}_{nm} \sin m\lambda] P_{nm}(\cos\theta) \tag{7.26}$$

7.4 Results

The global gravity anomaly field from enhanced GEOSAT data is presented in Figure 7.12 with maximum and minimum values of -374.78 and 400.83 mGal respectively. A regional detail is provided in Appendix D. The total RMS of the signal is 28.44 mGal.

It is not the ultimate intention of this study to provide a detailed tectonic interpretation since ultimately the generation of this product is a matter for mean sea surface enhancement. However it is useful to point out a number of tectonic features both large and small scale. These features include

1. Mid–ocean spreading centers - Slow spreading centers such as the mid–Atlantic ridge appear as a relatively high amplitude signal in comparison to those of high speed spreading centers.

2. A number of high amplitude ($>$ 30mGal) subduction zones at locations at the Aleutian, Philippine, Java, Marinana and Scotia plate trenches.

3. Primary transform faults and fracture zones are clearly visible whilst secondary faults and zones are harder to make out. In particular one can make out a range of triple junction features such as the south Indian ocean junction.

4. Evidence of absolute plate motions as a result of sub–lithospheric mantle plumes are provided from the existence of hot–spot swells. In the Pacific ocean one can resolve a number of linear volcanic island chains covering thousands of kilometers, other less obvious examples may be located within the Indian and Atlantic oceans.

5. Less obvious features such as the numerous seamounts in the eastern Pacific plate where the lithosphere is assumed thinner and some of the smaller tectonic micro–plates.

6. The compression of the Indian plate is clearly visible to the south of India as a result of its south–north motion into the Eurasian plate.

Ultimately the determination of global gravity fields of this type help facilitate other research such as in the locating of regions of interest for further investigation with sonar sounding. Also analysis of the frequency structure of the gravity field essentially helps determine the thermal evolution within the lithosphere and *Paleo*–tectonic reconstruction.

7.5 Validation

An independent means of assessing the accuracy of the product is available by shipboard gravity anomalies provided by the gravimeter. The GEODAS version 3.3 database contains a vast quantity of shipboard data however this was not immediately available and so the on–line version 3.3a was analysed for suitable profiles. Unfortunately just two profiles existed at the time of writing both from the U.S. National Science Foundation Nathaniel B. Parmer cruise ship. The GEODAS reference and cruise dates are

1. NBP92-8 13th Dec 1992 29th Jan 1993 track–A

2. NBP95-1 07th Feb 1995 13th Mar 95 track–B

The instrument used was a Lacoste and Romberg $S-36$ digital gravimeter and ship navigation was provided by Global Positioning System (GPS). Figure 7.11 provides gravity anomaly comparisons. Differences are 4.06 mGal RMS and 4.83 mGal for tracks A and B respectively.

Clearly, a wider range of shipboard profiles is required in order to fully validate the product. In particular, profiles are required in the equatorial regions in order to assess the degrading effect of the eastern vertical deflection in this latitudinal region. However, the results obtained here compare well with a study carried out by *Sandwell* (1992) on a GEOSAT derived field in the Pacific–Antarctic basin. *McAdoo* and *Marks* (1992) claim certain sections of ship profiles produce comparisons $\sim$2 mGal whilst others give as much as 20 mGal.

7.6 Conclusions

The global gravity anomaly field has been determined using high density enhanced altimetry from the GEOSAT geodetic mission. The product has been determined at a resolution of 0.075° which does not correspond to the maximum allowable from the Nyquist sampling theorem. The purpose of this exercise however, is for MSS model integration which in this case will require grids of equal size.

There will a number of possibilities both to improve resolution and precision. The former of these may be achieved via the re–computation of the field at the highest grid spacing. In terms of precision the integration of other data will be required in addition to other procedural improvements. In particular,

1. The inclusion of stacked ERS-1/2 35–day repeat data and ERS-1 high density geodetic phase data. However, the inclusion of stacked TOPEX/Poseidon data would have little effect on the high frequency field.

2. Some residual sea–surface variability in the wavelength range 100 to 1000 km probably exists. Effective removal of this (maybe through an optimal interpolation procedure) would be advantageous in terms of precision.

3. Ultimately, the problems encountered with the northern deflection at the latitudinal extremities and to a lesser extent, the eastern deflection at the equator need further analysis. The problem with the northern deflection is removed at the windowing stage but with loss of latitudinal coverage. However, the gravity field will be degraded at the equator. Here, platforms of differing inclination angles would clearly help.

4. In the unlikely case that a high accuracy and density altimetric geodetic mission was to take place this would provide a useful data addition as mentioned in point 1. However, if a future satellite mission with accurate orbital ephemeris were to be conducted then a method not requiring the computation of

along–track slopes could be used. A method based on *Anderson* and *Knudsen* (1995) could be adopted. Alternatively an optimal one using an inverse Stoke's transform could be investigated.

5. Dedicated non–altimetric gravity missions would clearly help gravity anomaly field development with improved accuracy.

6. The inclusion of ship–board gravity profiles can not improve the overall gravity field in terms of resolution. However they are useful for validation. Also, a valid gravity anomaly field can be used as a reference such that ship–board gravity profiles may have biases removed.

It is difficult to quantify exactly how the enhanced data has affected the gravity anomaly field recovery. Firstly, the computation of Δg using the original data would be required in order to allow a comparison. Here differencing of the two fields will show any residual features. Despite the computation of slopes to reduce long–wavelength features, some low amplitude long wavelength differences would be expected. Improvements in corrections with short wavelength characteristics would more likely improve the product.

Further, it should be noted that some oceanic signal is transfered at the computation of slopes stage and hence into the gravity anomaly field, rendering the final product an approximation to the true gravity anomaly field.

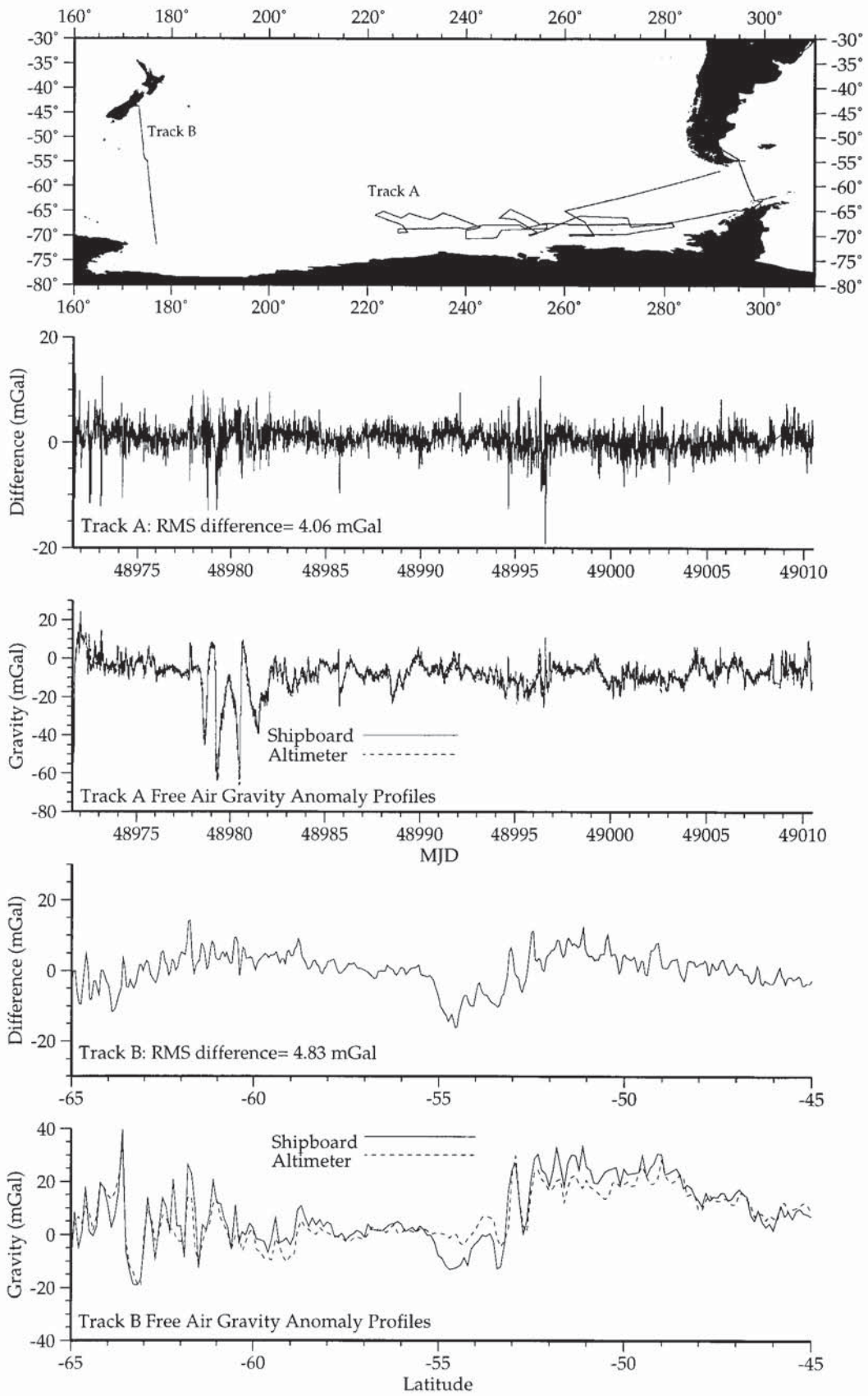

Figure 7.11: Global gravity anomaly field validation against two shipborne gravity anomaly profiles.

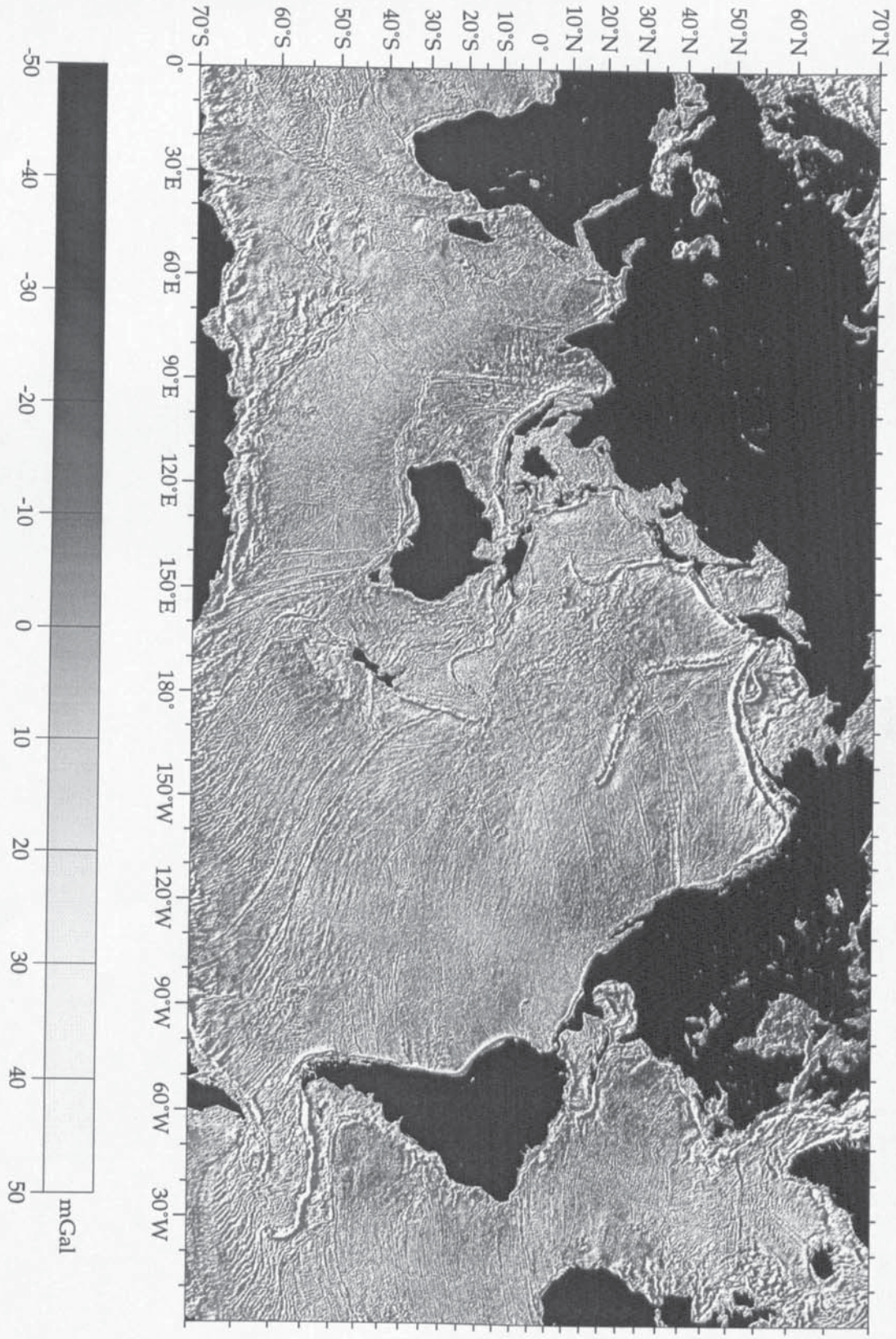

Figure 7.12: Global gravity anomaly field from enhanced GEOSAT geodetic mission data from the McAdoo—Marks methodology. Regional detail is provided in appendix D.

Chapter 8

Integrating Altimetry Data for a Combined MSS Solution

8.1 Introduction

Here the second stage for the integration of ERS-1 and GEOSAT geodetic phase data for a combined mean sea surface solution is presented. This is dealt with by first developing a GEOSAT residual mean sea surface from the gravity anomaly field described in the last chapter. This residual MSS is then combined with the ERS-1 optimally interpolated model described in chapter 6.

In chapter 7 the global gravity anomaly field was developed as a by–product of reducing the still relatively significant radial orbit error.[1]

Briefly summarising, the predominant once and twice per orbital revolution radial orbit errors are reduced via the computation of along–track slopes (Following *Sandwell*, 1984). Such a computation attenuates the orbit error to below the altimeter signal noise floor whilst accentuating short wavelength sea–surface features and with it amplifying high frequency noise. Following slope filtering to reduce this noise, north and east vertical deflections are computed using the along–track deflections and orientation alongside information regarding Earth rotation and orbital precession rate.

The global gravity anomaly field is finally derived using a spectral representation of the inverse Vening–Meinesz transform (see chapter 5 for full details.)

Although there are two similar methods allowing a MSS to be determined from the respective vertical deflection or gravity anomaly forms only the latter method

[1]Relative to ERS-1 and TOPEX/Poseidon. JGM3 derived orbits for GEOSAT are still highly inaccurate (*Cheney*, 1997b, quote 11 to 18 cm RMS for single–satellite crossover differences) resident within GEOSAT sea surface heights.

is investigated. Although both methods will be described, the vertical deflection to MSS method is left for a future investigative study.

Finally, the method developed for model integration is preliminary in the sense that it as been developed to investigate the *possibility* of improving the ERS-1 MSS via the inclusion of GEOSAT geodetic mission altimetry using spectral techniques.

8.2 The MSS from Vertical Deflections and Gravity Anomalies

In chapter 5 two methods of transforming grids of either vertical deflections (η and ξ) or gravity anomaly (Δg) to a geoid[2] *free* from orbit error. These two methods are now briefly described.

Vertical deflections to MSS: Equation 5.64 is

$$M_r(x,y) = \frac{\imath}{2\pi}\mathcal{F}^{-1}\left[\frac{(u\Theta + v\Xi)}{\sqrt{u^2+v^2}}\right] = \frac{\imath}{2\pi}\mathcal{F}^{-1}\left[\frac{(u\Theta + v\Xi)}{q^2}\right] \tag{8.1}$$

where,

M_r,	represents the residual mean sea surface,
$\mathcal{F}^{-1}[\ldots]$,	represents the inverse Fourier operator,
u, v	are spatial circular frequencies,
q,	is the total circular frequency, and,
Θ, Ξ,	are Fourier transforms of reduced signal north and east, deflection components (ξ and η respectively)
i,	is the imaginary operator equal to $\sqrt{-1}$.

The slight difference in notation between equations 5.64 and 8.1 is required since we are dealing with reduced power signals. Equation 8.1 shows that a mean sea surface is quite easily obtained providing vertical deflection grids are available.

Gravity anomaly to MSS: The residual gravity anomaly ΔG can be converted to a residual MSS, M_r following the slight modification of equation 5.51.

[2]It should be noted that here the geoid is an approximation since computation of slopes will still retain some oceanic signal. The signal is therefore referred to as a residual mean sea surface.

Here,

$$M_r = \mathcal{F}^{-1}\left[\frac{\Delta G(u,v)}{2\pi\gamma\sqrt{u^2+v^2}}\right] = \mathcal{F}^{-1}\left[\frac{\Delta G(u,v)}{2\pi\gamma q}\right]. \tag{8.2}$$

Equation 8.2 requires modification since at zero total circular frequency, $q = 0$ the function becomes singular. This may be resolved via the inclusion of equation 5.52.

The latter of these procedure was utilised despite essentially being the more complex of the two. However, as mentioned in the last chapter, this method does allow a gravity anomaly field to be developed for a *new* data set. Additionally, though this is not performed here, shipboard and terrestrial gravity profiles may be combined at some later date to help improve the model.

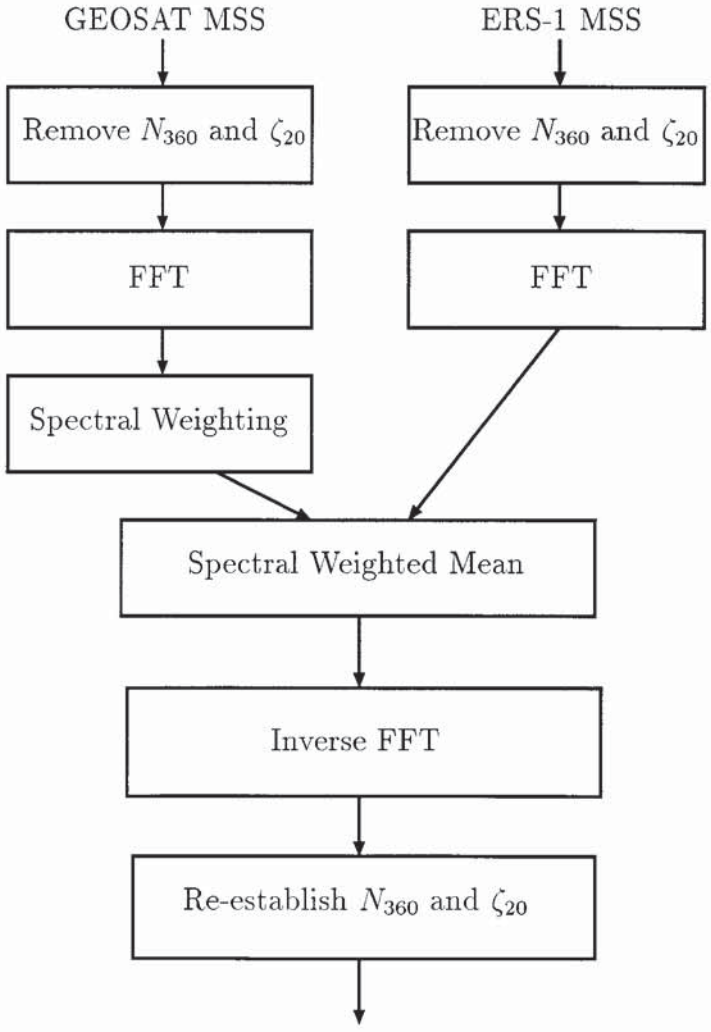

Figure 8.1: Schematic diagram for MSS model integration.

8.3 A Mean Sea Surface from a Gravity Anomaly Field

A mean sea surface may be reconstituted by re–establishing a geoid model to degree 360, N_{360} and a sea surface topography model to degree 20, ζ_{20}, i.e.,

$$M(x, y) = M_r(x, y) + N_{360} + \zeta_{20}. \tag{8.3}$$

Before considering the integration of models a simple MSS is developed as a starting point to show how the sea surface height–to–gravity anomaly–to–MSS copes as a stand alone model. The spectral gravity anomaly is determined by equation (7.23). In the spectral domain the residual field is converted to a spectral residual MSS via the use of equation 8.2 and the singularity at zero frequency is removed via the correction described in section 5.3. The GEOSAT MSS is then determined simply by the computation of the IFFT and the re–establishment of an EGM96 geoid and sea surface topography. Comparison of this surface against TOPEX/-Poseidon (cycle 66) sea surface heights produced an RMS difference of 18.4 cm; some 6 cm worse than the ERS-1 surface determined in chapter 6. This is certainly not a bad result when the collective effect of non sea surface variability removal and inclusion of residual long wavelength and medium/short wavelength errors are taken into consideration. Finally it shows that the prolonged spectral manipulation has not had any drastic effect, i.e., 18.4 cm RMS is still a considerable improvement over the combined EGM96 geoid and sea surface topography which gives an RMS of ~ 27 cm with TOPEX cycle 66. For completeness the difference between the optimally interpolated ERS-1 MSS and the GEOSAT MSS is shown in Figure 8.2. Here we see this signal is still dominated with GEOSAT orbit streaks though they are of low amplitude ($< \pm 15$ cm.)

8.4 Combining Marine geoids in the Spectral Domain

The procedure for integrating ERS-1 and GEOSAT sea surface data sets is shown schematically in Figure 8.1. The method proposed will combine both MSS at a residual stage in the frequency domain. This is the natural state of the GEOSAT residual surface after conversion from spectral gravity anomaly. However the ERS-1 surface requires the removal of the complete EGM96 geoid and sea surface topog-

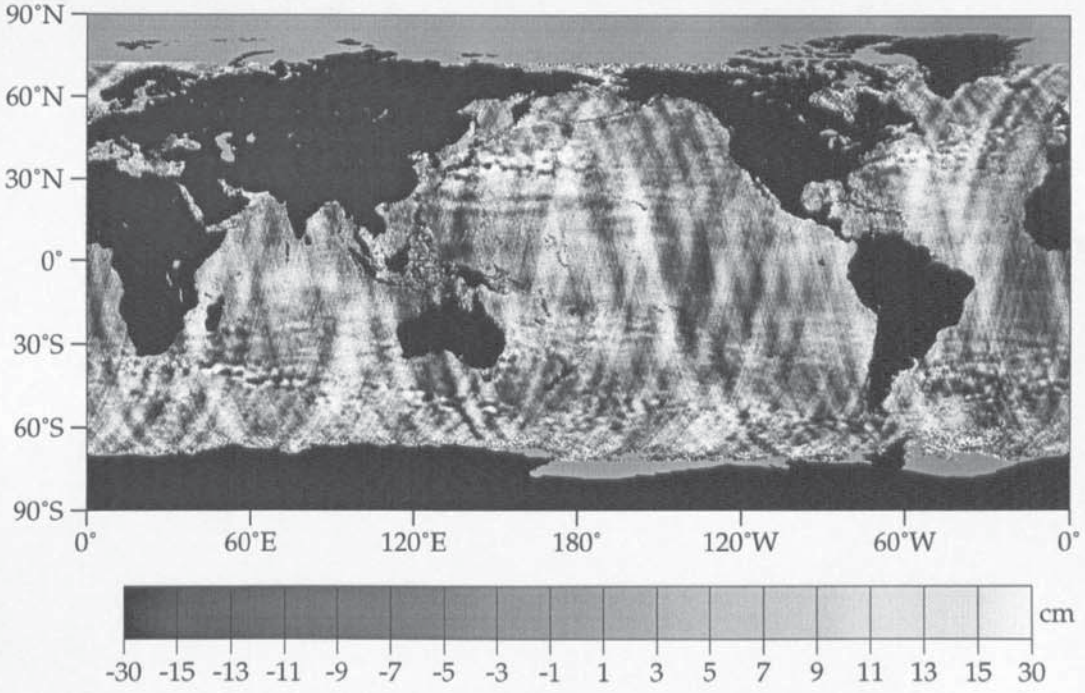

Figure 8.2: Difference between ERS-1 and GEOSAT residual altimetric surfaces.

raphy. The grid size used covers $\pm 72°$ and thus ERS-1 requires further windowing at latitudinal extremities, here set to 5° as described in the last chapter.

Considering the difference of accuracies between the two satellite dependent mean sea surfaces the integration procedure is based on a weighting system between the two models. The ERS-1 residual MSS will be the dominant model with the GEOSAT MSS having an equal weighting (a weighting of 1) for three different frequency bands. These weightings are essentially high pass cosine filters and a schematic of this is displayed in Figure 8.3. This is based on the premise that the major error in the GEOSAT mean sea surface signal is still in the medium and long wavelengths. The cut–off frequencies are 200, 500 and 2000 km and the filter width is 100 km. Outside the high pass filter the weighting will reduce to 0. Thus the final reconstituted MSS, M_{int} is given by

$$M_{int}(x,y) = N_{360} + \zeta_{20} + \mathcal{F}^{-1}\left[\frac{1}{\sum_{i=1}^{n} W_i(u,v)} \sum_{i=1}^{n} M_i(u,v) W_i(u,v)\right] \qquad (8.4)$$

where, i is the MSS index, W_i is the weighting as a function of spatial frequencies, u and v. Therefore, if M_1 represents the ERS-1 surface then $W_1 = 1$ for all frequencies.

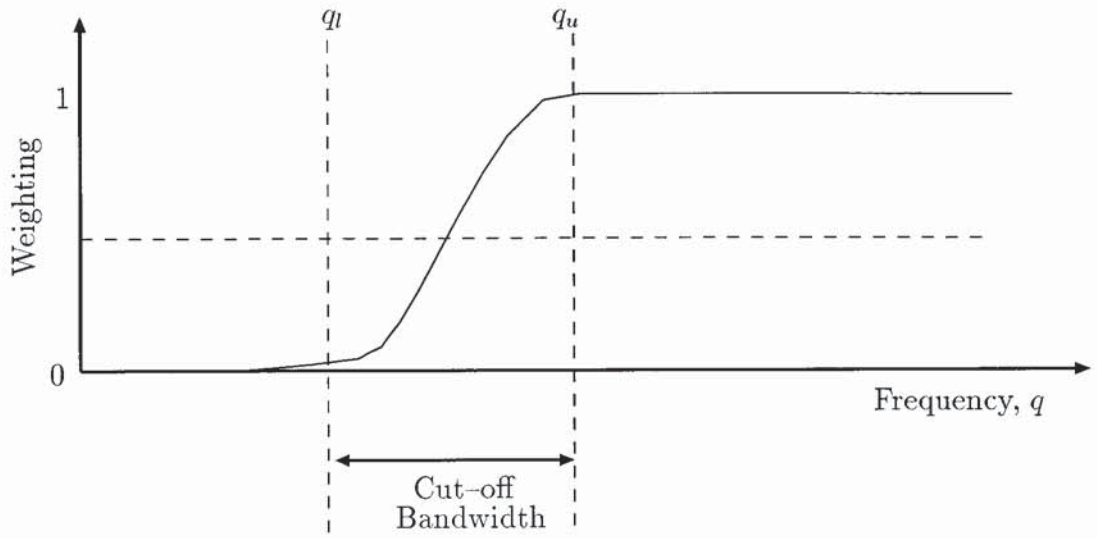

Figure 8.3: Schematic form of weighting.

Whilst the GEOSAT surface M_2 will have a weighting based upon

$$W_2(u,v) = \begin{cases} 1, & < q_l, \\ \frac{1}{2}\left(1 + \cos\pi\left(\frac{q-q_l}{q_u-q_l}\right)\right), & q_l \leqslant q \leqslant q_u, \\ 0, & > q_u \end{cases} \tag{8.5}$$

where,

q, is the total circular frequency, $q = \sqrt{u^2+v^2}$,

q_l, the lower limit cut–off, and,

q_u, is the upper limit cut–off.

Having computed the weight W_2 the weighted mean of the two residual spectral mean sea surfaces is determined. The inverse Fourier transform is computed and the EGM96 geoid and sea surface topography added back.

The weighting for the GEOSAT surface was computed for three different cut–off wavelengths mentioned earlier reflecting short and medium wavelength combinations.

8.5 Validation and Results

The resulting three MSS models were compared against 15 cycles of TOPEX sea surface heights as in chapter 6 and Table 6.3. The comparisons are displayed in Tables 8.1 8.2 and 8.3 over shallow seas, ocean and combined shallow seas and ocean.

The main focus of these results centers around the degrading of the original ERS-1 MSS as longer GEOSAT wavelengths are included. With a 2000 km cut–off the combined shallow/ocean comparison with TOPEX is between 15.5 and 17.6 cm RMS. An improvement is made with the 500 km cut–off that gives 14.2 to 16.0 cm RMS. However with the highest frequency band with cut–off at 200 km it is inconclusive whether the original MSS has been degraded.

BAND 1 (200 km cut–off)												
Cycle	Shallow				Ocean				Total			
No.	Number	Rej	σ_{oi} (cm)	σ_{in} (cm)	Number	Rej	σ_{oi} (cm)	σ_{in} (cm)	Number	Rej	σ_{oi} (cm)	σ_{in} (cm)
58	37978	5317	(17.9)	18.0	466854	18890	(13.5)	13.5	504832	24207	(13.8)	13.8
60	38870	5272	(17.4)	17.8	456289	13990	(13.5)	13.5	495159	19262	(13.8)	13.8
62	40635	6638	(18.1)	18.1	449658	11345	(13.3)	13.8	490293	17983	(13.7)	13.7
64	41919	6150	(17.6)	17.9	440646	9657	(13.0)	13.2	482565	15807	(13.4)	13.4
66	42959	7632	(16.5)	16.6	433848	8209	(12.3)	12.3	476807	15841	(12.7)	12.7
68	43721	7746	(17.7)	17.7	424169	7498	(12.9)	12.9	467890	15244	(13.3)	13.3
70	46456	8735	(17.9)	17.9	423010	6874	(13.3)	13.4	469466	15609	(13.7)	13.7
72	48632	9562	(17.7)	18.0	419016	6648	(13.4)	13.4	467648	16210	(13.8)	13.8
74	49553	10022	(18.1)	18.1	419455	7416	(13.7)	13.7	469008	17438	(14.1)	14.1
76	48465	9749	(18.3)	18.3	415101	7189	(13.7)	14.0	463566	16938	(14.2)	14.2
78	48660	9110	(18.2)	18.3	422631	7039	(13.6)	13.8	471291	16149	(14.1)	14.0
80	45536	8064	(18.0)	18.0	423357	8085	(13.6)	13.3	468893	16149	(14.0)	14.0
82	42306	6351	(18.4)	18.4	439551	9744	(13.7)	13.8	481857	16095	(14.1)	14.1
84	39316	6061	(17.9)	17.9	456689	14753	(13.8)	13.5	496005	20814	(14.1)	14.1
86	37802	5384	(18.3)	18.3	463180	17571	(13.8)	14.0	500982	22955	(14.1)	14.1

Table 8.1: Validation of integrated MSS against TOPEX data for a bandwidth cut–off at 200 km. σ_{oi} are the optimally interpolated MSS RMS values (see chapter 6) and σ_{in} are those for the integrated MSS.

BAND 2 (500 km cut–off)												
Cycle	Shallow				Ocean				Total			
No.	Number	Rej	σ_{oi} (cm)	σ_{in} (cm)	Number	Rej	σ_{oi} (cm)	σ_{in} (cm)	Number	Rej	σ_{oi} (cm)	σ_{in} (cm)
58	37978	5341	(17.9)	19.4	466854	18922	(13.5)	14.7	504832	24263	(13.8)	15.0
60	38870	5288	(17.4)	18.9	456289	14018	(13.5)	15.1	495159	19306	(13.8)	15.4
62	40635	6659	(18.1)	20.0	449658	11374	(13.3)	14.7	490293	18033	(13.7)	15.2
64	41919	6176	(17.6)	18.9	440646	9690	(13.0)	14.7	482565	15866	(13.4)	15.1
66	42959	7662	(16.5)	18.4	433848	8236	(12.3)	13.8	476807	15898	(12.7)	14.2
68	43721	7762	(17.7)	18.6	424169	7528	(12.9)	14.2	467890	15290	(13.3)	14.6
70	46456	8762	(17.9)	19.3	423010	6891	(13.3)	14.7	469466	15653	(13.7)	15.1
72	48632	9589	(17.7)	19.3	419016	6680	(13.4)	14.3	467648	16269	(13.8)	14.8
74	49553	10042	(18.1)	19.4	419455	7455	(13.7)	14.6	469008	17497	(14.1)	15.1
76	48465	9769	(18.3)	20.0	415101	7224	(13.7)	15.0	463566	16993	(14.2)	15.5
78	48660	9133	(18.2)	19.2	422631	7067	(13.6)	15.7	471291	16200	(14.1)	16.0
80	45536	8100	(18.0)	19.5	423357	8124	(13.6)	14.6	468893	16224	(14.0)	15.0
82	42306	6380	(18.4)	20.3	439551	9761	(13.7)	15.2	481857	16141	(14.1)	15.6
84	39316	6089	(17.9)	18.9	456689	14784	(13.8)	14.9	496005	20873	(14.1)	15.3
86	37802	5412	(18.3)	19.7	463180	17606	(13.8)	15.4	500982	23018	(14.1)	15.7

Table 8.2: Validation of integrated MSS against TOPEX data for cut–off at 500 km.

A point to note is that regarding the number of altimeter points rejected. As with the validation carried out within chapter 6, a point is rejected if the difference between MSS height and instantaneous sea surface height exceeds 60 cm. It can be seen from Table 8.1 that there are slightly less rejections for the integrated MSS. For each of the TOPEX cycles a comparison for the percentage number of rejections

	BAND 3 (2000 km cut-off)											
Cycle	Shallow				Ocean				Total			
No.	Number	Rej	σ_{oi} (cm)	σ_{in} (cm)	Number	Rej	σ_{oi} (cm)	σ_{in} (cm)	Number	Rej	σ_{oi} (cm)	σ_{in} (cm)
58	37978	5876	(17.9)	20.8	466854	18925	(13.5)	16.0	504832	24286	(13.8)	16.4
60	38870	6108	(17.4)	20.9	456289	14014	(13.5)	16.9	495159	19311	(13.8)	17.1
62	40635	6873	(18.1)	21.1	449658	11369	(13.3)	17.0	490293	18047	(13.7)	17.3
64	41919	7038	(17.6)	21.2	440646	9677	(13.0)	15.8	482565	15860	(13.4)	16.2
66	42959	7534	(16.5)	19.4	433848	8252	(12.3)	15.1	476807	15912	(12.7)	15.5
68	43721	8141	(17.7)	20.3	424169	7542	(12.9)	15.9	467890	15327	(13.3)	16.3
70	46456	9169	(17.9)	21.3	423010	6898	(13.3)	16.6	469466	15671	(13.7)	17.0
72	48632	9608	(17.7)	20.9	419016	6687	(13.4)	16.4	467648	16293	(13.8)	16.8
74	49553	10048	(18.1)	21.3	419455	7455	(13.7)	16.3	469008	17503	(14.1)	16.8
76	48465	9792	(18.3)	21.3	415101	7223	(13.7)	17.2	463566	17015	(14.2)	17.6
78	48660	9134	(18.2)	21.1	422631	7082	(13.6)	16.4	471291	16216	(14.1)	16.9
80	45536	8106	(18.0)	20.9	423357	8119	(13.6)	15.8	468893	16225	(14.0)	16.3
82	42306	6385	(18.4)	21.2	439551	6913	(13.7)	16.6	481857	16149	(14.1)	17.0
84	39316	6090	(17.9)	21.2	456689	6076	(13.8)	16.1	496005	20874	(14.1)	16.5
86	37802	5409	(18.3)	21.7	463180	6059	(13.8)	16.7	500982	23004	(14.1)	17.1

Table 8.3: Validation of integrated MSS against TOPEX sea–surface heights at a cut–off of 1000 km.

over shallow/ocean data is given in Table 8.4. Over each cycle an improvement is made on the number of rejection. Hence, it may be that whilst the inclusion of GEOSAT altimetry cannot improve the overall performance of ERS-1 data it can improve the scope of the computed mean sea surface.

The integrated mean sea surface that compares best with TOPEX data is displayed in Figure 8.4. This has a long wavelength EGM96 geoid to degree 20 removed so small scale features may be observed. To assist in this Figures 8.5, 8.6 and 8.7 are shown for 120° longitudinal sections of the Earth.

Comparison with the gravity anomaly field displayed in Figure 7.12 shows that most of the short–wavelength features are not as prominent. However, all the major tectonic features are displayed in the Pacific, Atlantic and Indian oceans.

8.6 Conclusion

A method for the integration of ERS-1 and GEOSAT mean sea surfaces based on their respective geodetic missions has been presented. The methodology is preliminary and requires further study in order to determine how GEOSAT data degrades the ERS-1 MSS.

Integrating the data sets with an optimal interpolation approach may prove to be a more productive method rather than the complex technique incorporated here. Additionally, vital GEOSAT geodetic mission resolution is lost in this study in order to allow resolution consistency with the ERS-1 optimal mean sea surface. A technique that allows an improvement of the optimal mean sea surface resolution

is a separate study in itself; however it would be highly useful.

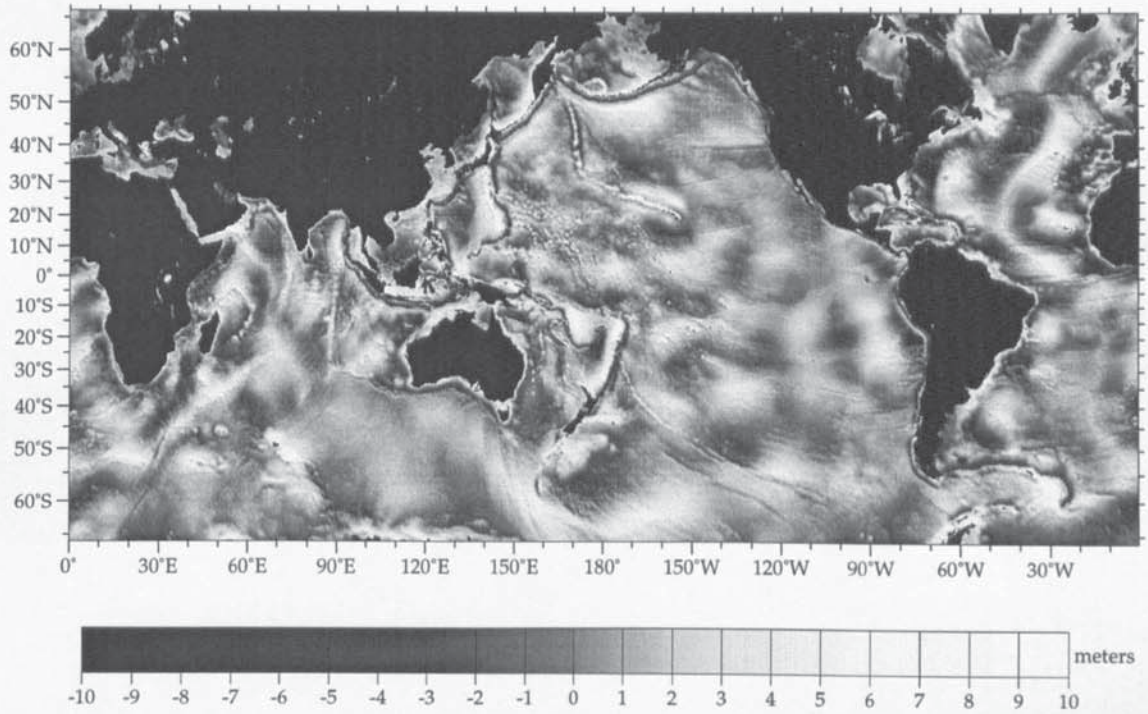

Figure 8.4: Global integrated mean sea surface with a long wavelength geoid, N_{30} and sea surface topography, ζ_{20} removed.

Cycle No.	% of Rejections ERS-1 MSS	Integrated MSS	% change
58	4.94	4.79	0.14
60	4.13	3.89	0.24
62	3.86	3.67	0.19
64	3.53	3.28	0.24
66	3.44	3.32	0.12
68	3.45	3.26	0.19
70	3.60	3.32	0.28
72	3.66	3.47	0.19
74	3.81	3.72	0.09
76	3.78	3.65	0.13
78	3.66	3.43	0.23
80	3.59	3.44	0.15
82	3.62	3.34	0.28
84	4.25	4.20	0.05
86	4.84	4.58	0.26

Table 8.4: Comparison of valid data points for optimally interpolated ERS-1 MSS in chapter 6.

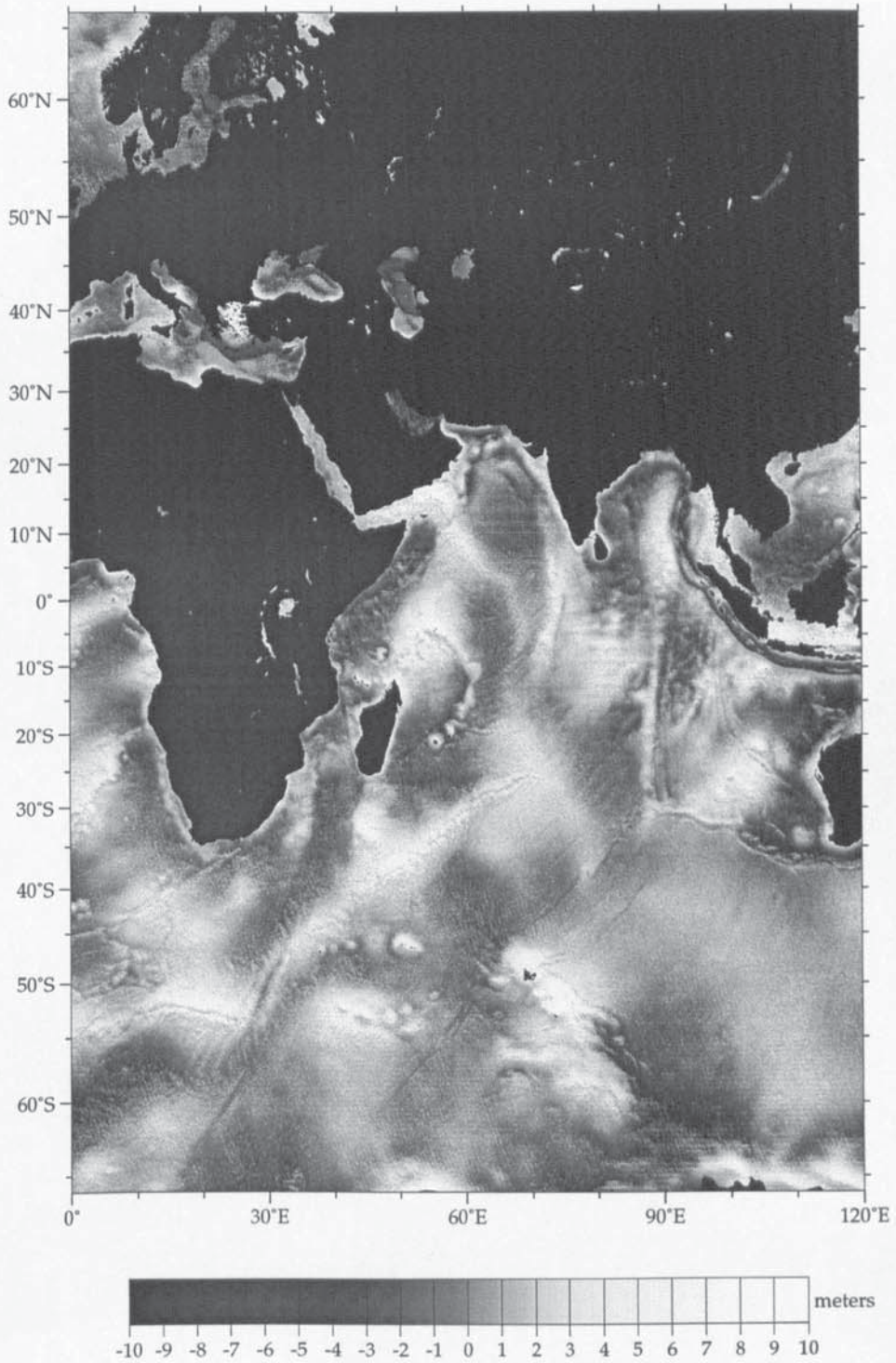

Figure 8.5: Mean sea surface over south eastern Atlantic and Indian oceans with removal of N_{30} and ζ_{20}.

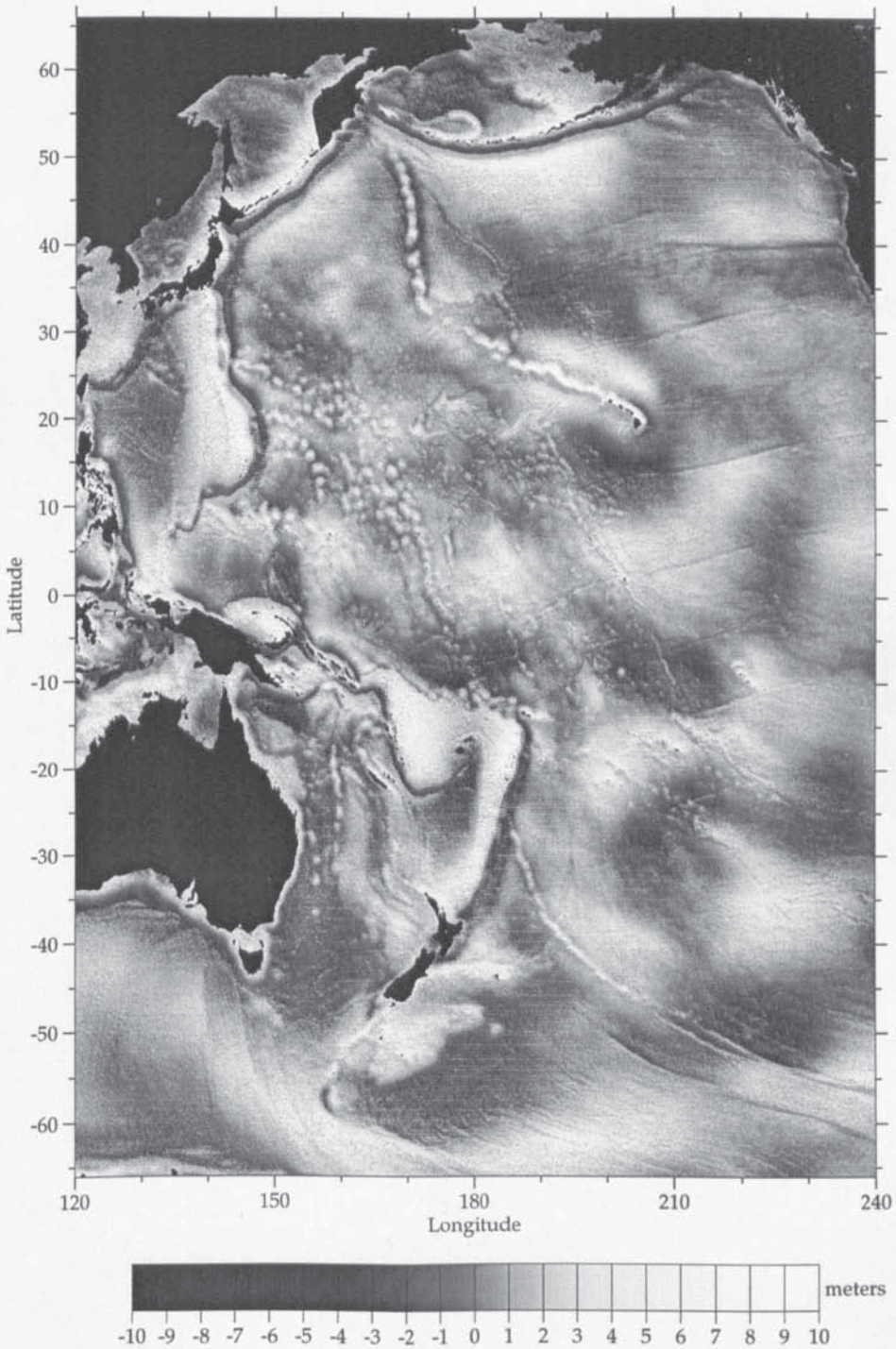

Figure 8.6: Regional short wavelength mean sea surface mainly displaying the Pacific ocean.

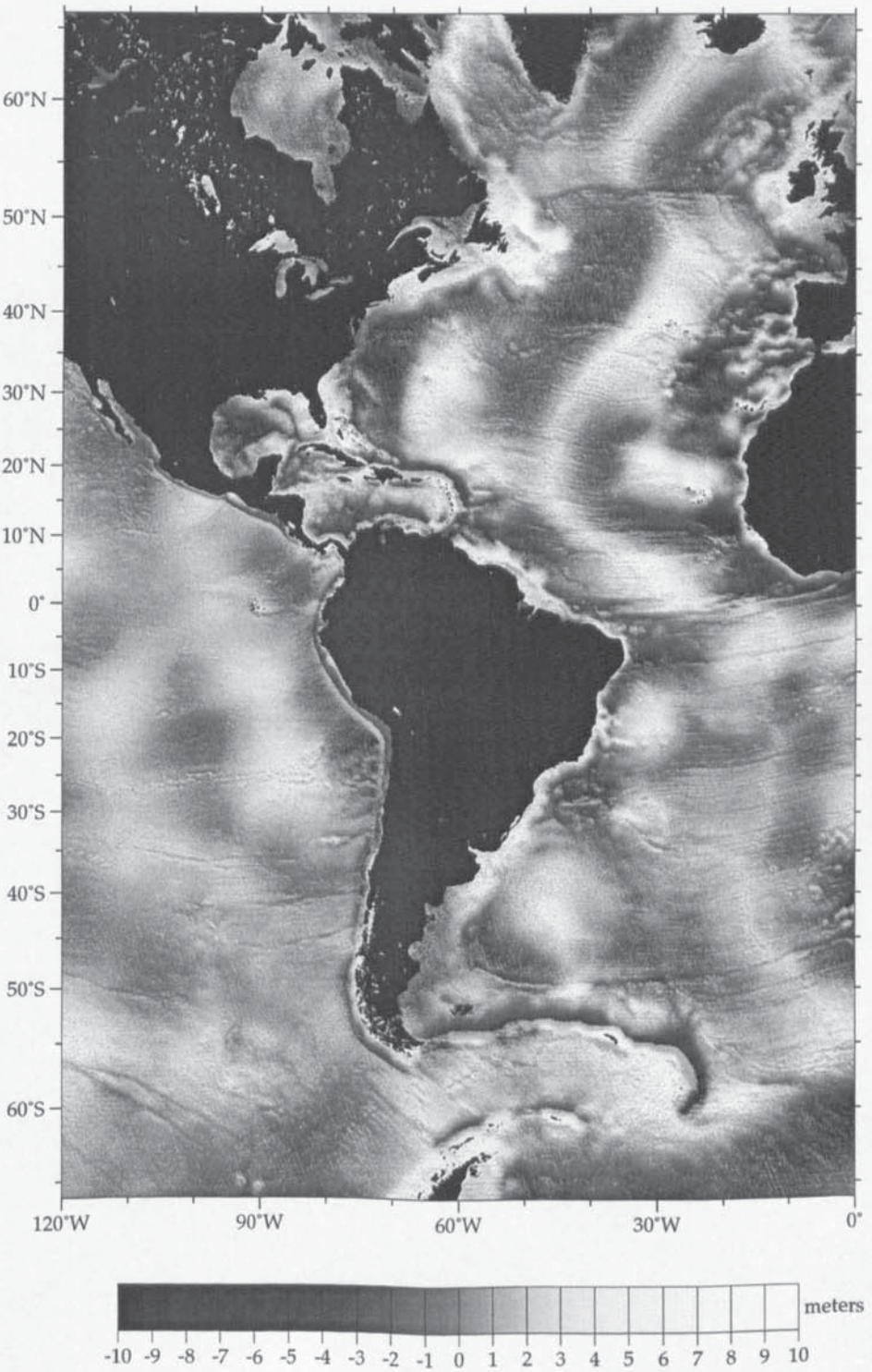

Figure 8.7: Short wavelength regional MSS displaying eastern Pacific and the majority of the Atlantic tectonic structure.

Chapter 9

Conclusions

The main objective of this thesis is the development of a global high resolution mean sea surface model from spaceborne altimetric sea surface heights. Two procedures were developed both of which investigated the use of fast spectral techniques. These were,

1. The optimal interpolation of the mean sea surface within the Fourier domain using ERS-1 geodetic mission data.

2. The integration of the first mean sea surface with one determined from the relatively inaccurate GEOSAT sea surface heights.

Other contemporary methods have in general used variations on spatial least squares techniques utilising combinations of ERS-1 geodetic, multi–disciplinary phase (35–day repeat) and a year of stacked 10–day TOPEX/Poseidon data. The highly accurate TOPEX sea–surface heights were used to validate the models. Therefore objective evaluation of the individual techniques is problematic. It was therefore decided that any methodology developed here would by choice not contain T/P data in order to retain an independent means of validation.

The description of the science commenced with an explanation of the elements of mean sea surface structure (chapter 2), the function of the radar altimeter (chapter 3), and methods of computing error corrections (chapter 4.) The theoretical possibilities were explored in chapter 5 to utilise Fourier domain techniques to (a) improve a mean sea surface model via optimal interpolation and (b) integrate models via Stokes' and Vening–Meinesz' transforms. The spectral interpolation methodology was then demonstrated in chapter 6 with the use of ERS-1 geodetic phase sea–surface heights. Fifteen cycles of TOPEX data were used to evaluate the model. This revealed a model fit between 12.3 and 13.8 cm RMS, an improvement on the un–optimally interpolated MSS that fitted between 15.7 and 16.2 cm

RMS. The model compares favourably with a number of other models that contained a complete years worth of TOPEX/Poseidon data in addition to varying amounts of ERS-1 geodetic multi–phase data. The models presented by *Yi* (1995) (OSU), *Kim* (1993) (CSR) and *Cazenave* et al. (1995) (CNES) have and been shown to fit TOPEX sea surface heights between 9.5 and 10.2 cm RMS (see *Yi*, 1995). On the other hand the same report showed a MSS model not including TOPEX data from DPAF to only fit to 18 cm RMS.

The procedure was developed to integrate this mean sea surface with enhanced GEOSAT geodetic mission sea–surface heights. As described in chapter 7 the technique was conducted in two parts. The first involved further reduction of long wavelength errors despite the improvements within the enhanced data set. These errors were minimised via the computation of sea surface slopes. The *McAdoo* and *Marks* (1992) method was then adopted to compute vertical deflection grids and the global gravity anomaly field. Despite having some fundamental problems, the method is useful as a means of deriving gravity anomalies. Further, the field was validated against a limited number of ship–board profiles and showed a fit of $\sim$4.5 mGal.

The second part of developing an integrated mean sea surface involved converting the gravity anomaly field to a residual MSS within the spectral domain (see chapter 8.) The residual spectral MSS was weighted via high pass filtering at three different frequencies. Three resultant surfaces were then computed via a weighted mean calculation at each frequency. These preliminary results showed that only the inclusion of GEOSAT mean sea surface high frequency components retained the accuracy of the original MSS. However it was shown that the so called *scope* of the MSS was improved in the sense that less TOPEX data points were rejected.

The fundamental contributions described with reference to both geodetic and ocean sciences are therefore;

1. An enhanced cubic B–spline methodology was developed based on that described by *Le Traon* et al. (1995) for the minimisation of ERS-1 radial orbit error with reference to TOPEX/Poseidon.

2. In other methods the use of profile stacking has been utilised. Unfortunately, the stacking approach method can only be applied to repeat track data. Since stacking cannot be used for the 168 day ERS-1 mission other MSS models have shown cross track gradients in regions of high variability requiring further correction. The MSS developed here used sea surface variability removal from each sea surface height. Variability fields were computed from TOPEX/-

Poseidon altimetry and optimally interpolated at 5 day intervals. The result was minor cross–track gradients.

3. The spectral optimal interpolation of a MSS using geodetic phase altimeter from the ERS-1 mission. This surface was then validated against an independent source, i.e., the highly accurate TOPEX sea surface heights.

4. The use of a gridded residual altimetric surface in order to describe data signal error power spectral densities. This bypassed the need for the slow computation of model covariances describing the major error contributors, i.e., radial orbit, geoid, etc.

5. A global gravity anomaly field developed from newly released enhanced GEOSAT geodetic mission using a now standard technique of computation.

6. The development of a methodology for the combination of high resolution MSS models from missions of differing accuracy.

7. The possibility of spectral MSS modelling via direct use of vertical deflection components (see equation 5.64.)

8. All of the above points relied on the use of the newly developed EGM96 gravity field and sea surface topography model. This essentially brings this field up to date.

With respect to studies carried out within this thesis it would be important to carry out further analyses. The following points should be considered for future research in mean sea surface studies:

1. Models will ultimately become more refined as more data becomes available. Hence for a definitive MSS something on the scale of 10 years of long repeat altimetry data is required, i.e., a repeating geodetic mission. Such data would assist a range of sciences. However, no such mission is currently being planned. There are however a number of plans for a much needed gravity mission such as what would have been ARISTOTLES. Such missions as GOCE, GRACE and CHAMP would advance gravity field modelling a great deal.

   Thus it is necessary to make the most out of current and future data. Namely repeat 35 day ERS-1/ERS-2, repeat 10 day TOPEX/Poseidon, and in the future GEOSAT Follow–on, ENVISAT–1 and JASON-1.

2. The estimate of the noise contribution of a global altimetric surface from the data itself is advantageous as it overcomes the need to use covariance models for each major error element. It would be desirable to investigate further how different errors build up an overall error surface. Such analyses may help improve the modelling of some corrections.

3. Integrating altimetric data sets is clearly important in terms of improving models. Since gridding data is computationally time consuming a means of improving a MSS model via the integration of new data is advantageous. The method described in chapter 8 uses two data sets; one from a relatively accurate mission (ERS-1) and the other less precise (GEOSAT). Since the larger error contributions are from the longer wavelengths then only the short wavelengths can really contribute in the MSS modelling. However if an *accurate* geodetic mission is launched in the future then a further study would possibly allow the contribution of all wavelengths to take place.

4. The gravity anomaly field produced here requires further validation. This can be achieved with data from the GEODAS version 3.3 database rather than the use of the on–line version 3.3a.

5. Once again the inclusion of more altimetry is required in gravity anomaly modelling. Here, missions with different inclination angles should help compensate for the failure of the eastern and, in particular, northern deflection of the vertical at the equator and latitudinal extremity respectively (see eq. 7.8.) Additionally shipboard and land based gravity data should be included into the model.

6. In this thesis modelling has used specifically the FFT on a flat Earth. Since there are other transforms available for example, Hartley, Wavelet and Spherical FFT's, then these could be incorporated with reference to MSS modelling on a wide range of spatial scales.

7. It would be useful to develop an optimally interpolated MSS in the spatial domain to both determine the time advantages of the FFT and their surface differences.

Finally it is interesting to note that in the 1960s there was no substantial coverage of global sea–surface height. Now we have reached the age of continuous precise monitoring that will have an unimaginable effect on geodetic, sea–level and ocean–

atmospheric climate studies. In the 25 years of spaceborne radar altimetry missions MSS modelling errors have reduced from tens of meters to just tens of centimetres.

Appendix A

Acronyms and Abbreviations

ACV	Auto–Covariance
ADC	Analogue-to-digital conversion
AGC	Automatic Gain Control
ASG	Aston Space Geodesy
ATSR	Along–Track Scanning Radiometer
ATSR-M	ATSR Microwave Sounder
AVISO	Archiving, Validation and Interpretation of Satellite Oceanographic data
BLA	Beam–limited Altimeter
CERSAT	Centre ERS d'Archivage et de Traitement
CNES	Centre National d'Etudes Spatiales
COG	Centre–of–gravity
COSPAR	Committee on Space Research
CSR	University of Texas Center for Space Research
DEM	Digital Elevation Model
DFT	discrete Fourier transform
DORIS	Doppler Orbitography and Radiopositioning Integrated by Satellite
DOV	Deflection of the Vertical
DMSP	Defence Meterological Satellite
ECMWF	European Centre for Medium–term Weather Forcasting
EGM	Earth Gravity Model
ERS	Earth Remote Sensing
ENVISAT	Enviromental Satellite
EODC	Earth Observation Data Center
ERM	Exact Repeat Mission
EOS	Earth Observing System
ESA	European Space Agency
FFT	fast Fourier transform
FNOC	Fleet Numerical Ocean Model
GDR	Geophysical Data Record
GEM	Goddard Earth Model
GEOSAT	Geodetic Satellite
GFO	GEOSAT Follow-on
GM	Geodetic Mission
GMT	Generic Mapping Tools
GPS	Global Positioning System

GRACE	Gravity Recovery and Climate Experiment
GSFC	Goddard Space Flight Centre
IB	Inverted Barometer
IPCC	International Panel on Climate Change
IRI	International Reference Ionosphere
MGD77	Marine Geophysical Data Exchange Format 1977
MSS	Mean Sea Surface
MWR	Microwave Radiometer
NCEP	National Centers for Environmental Prediction
NERC	Natural Environment Research Council
NIMA	National Imagery and Mapping Agency
NOAA	National Oceanographic and Atmospheric Administration
NODC	National Oceanographic Data Centre
NRA	NASA Radar Altimeter
NSWC	Naval Surface Weapons Center
NVAP	NASA Water Vapour Project
OPR	Off-line Ocean Products
OSU	Ohio State University
PAF	Processing and Archiving Facility
PLA	Pulse-limited Altimeter
POD	Precise orbit determination
PRARE	Precise Range and Range-rate Equipment
PRF	Pulse Repetition Frequency
PSD	Power Spectral Density
QSST	Quasi-stationary Sea Surface Topography
RA	Radar Altimeter
RCS	Radar Cross-Section
RMS	Root Mean Square
SLR	Satellite Laser Ranging
SMLE	Sub-Optimal Maximum Likelihood Estimator
SNR	Signal-to-Noise Ratio
SRA	Space-Bourne Radar Altimeter
SSB	Sea-State bias
SSALT	Solid-State Radar Altimeter
SSH	Sea-Surface Height
SSMI	Special Sensor Microwave Imager
SSV	Sea Surface Variability
SWH	Significant Wave Height
TEC	Total Electron Content
TOGA	Tropical Ocean and Global Ocean program
TOPEX	Topography Experiment
TOVS	TIROS Operational Vertical Sounder
T/P	TOPEX/Poseidon
TP—E	TOPEX/Poseidon—ERS-1
URSI	International Union of Radio Science
USO	Ultra Stable Oscillator
WOCE	World Ocean Circulation Experiment

Appendix B

Related Theory

B.1 Spherical Harmonic Expansions of the Gravity Anomaly Field

Following *Heiskanen* and *Moritz* (1967) the gravity anomaly Δg may be computed from the anomalous potential, T via the use of the spherical approximation

$$\Delta g = -\frac{\partial T}{\partial r} - \frac{2}{r}T \tag{B.1}$$

where, r is the geocentric radial distance. The spherical expansion of the anomalous potential is obtained from the gravitational potential minus the normal ellipsoidal potential (see chapter 2 for definition of parameters), or

$$T(\theta, \lambda, r) = \frac{\mu_e}{r} \sum_{n=2}^{n_{max}} \left(\frac{R_e}{r}\right)^n \sum_{m=0}^{n} [\hat{C}_{nm} \cos m\lambda + \hat{S}_{nm} \sin m\lambda] P_{nm}(\cos\theta). \tag{B.2}$$

where,

μ_e,	The product between gravitational constant and Earth's mass,
R_e,	Earth's mean radius,
P_{nm},	Legendre polynomials,
r, θ, λ,	geocentric radial distance, latitude amd longitude,
$\hat{C}_{nm}, \hat{S}_{nm}$,	Stoke's coefficient's relative to normal gravity,
n, m, n_{max},	degree, order and maximum degree of expansion.

Equation B.2 is rearranged to deal with an expansion commencing at degree $n=0$, or

$$T(r,\theta,\lambda) = \sum_{n=0}^{n_{max}} \left(\frac{R_e}{r}\right)^{n+1} T_n(\theta,\lambda) \tag{B.3}$$

here, $T_n(\theta,\lambda)$ are the Laplace's surface harmonics given by

$$T_n(\theta,\lambda) = \frac{\mu_e}{R_e} \sum_{m=0}^{n} [\hat{C}_{nm} \cos m\lambda + \hat{S}_{nm} \sin m\lambda] P_{nm}(\cos\theta). \tag{B.4}$$

Δg is therefore determined by substituting equation B.3 into equation B.1. Therefore, for to a maximum degree of n_{max}

$$\Delta g = \frac{1}{r} \sum_{n=0}^{n_{max}} (n+1) \left(\frac{R_e}{r}\right)^{n+1} T_n(\theta,\lambda) - \frac{2}{r} \sum_{n=0}^{n_{max}} \left(\frac{R_e}{r}\right)^{n+1} T_n(\theta,\lambda), \tag{B.5}$$

or, rearranging,

$$\Delta g = \frac{1}{r} \sum_{n=0}^{n_{max}} (n-1) \left(\frac{R_e}{r}\right)^{n+1} T_n(\theta,\lambda). \tag{B.6}$$

Expanding T_n, computing Δg on the geoid ($r=R_e$) and noting the nonexistence of Δg at degree $n=1$ we get

$$\Delta g(\theta,\lambda) = \frac{\mu_e}{R_e^2} \sum_{n=2}^{n_{max}} (n-1) \sum_{m=0}^{n} [\hat{C}_{nm} \cos m\lambda + \hat{S}_{nm} \sin m\lambda] P_{nm}(\cos\theta). \tag{B.7}$$

B.2 The Altimetric Radar Equation

In chapter 3 the altimetric radar equation was given in respect to altimeter design. Here the property will be derived from traditional theory described in *Skolnik* (1990) and specifically for the altimeter based on *Elachi* (1988). To begin with we derive the basic radar equation and then develop this to give the Signal–to–Noise Ratio variations over the ocean utilising two different geometries. Additionally the equation for ice surfaces is given to show how high power returns over such surfaces disrupt sea–surface measurements.

For an altimeter at a height, h above a surface the power density per unit area,

P_h measured in Watts (W) is given by

$$P_h = \frac{P_t G L_1}{4\pi h^2} \quad \text{wm}^{-2} \tag{B.8}$$

where,

G, is the antenna gain,
P_t, the transmitted single pulse power, and
L_1, is the one way media path loss.

In Equation (B.8) $4\pi h^2$ represents the isotropic transmission of power constrained by the directional antenna gain G. The signal power, P_{rr} intercepted at the surface and re–radiated is a function of Radar Cross Section, σ (see *Skolnik* (1990) for a description of this parameter) in units of area.

$$P_{rr} = \frac{P_t G \sigma L_1}{4\pi h^2} \qquad \text{Watts.} \tag{B.9}$$

The radar cross section may be expanded to incorporate measureable parameters. These are:

1. Backscatter coefficient, σ^0 computed eventually from return waveform amplitude.

2. Antenna footprint area, A_{ft} on the surface illuminated by microwave energy. This parameter is determined trigonometrically via the angle of antenna illumination and pulse length.

The radar cross–section σ is given by the product

$$\sigma = \sigma^0 A_{ft} \tag{B.10}$$

and therefore P_{rr} is now

$$P_{rr} = \frac{P_t G \sigma^0 A_{ft} L_1}{4\pi h^2} \qquad \text{Watts.} \tag{B.11}$$

The power incident back at the antenna, P_{inc}, i.e., a distance h from the earth surface is

$$P_{inc} = \frac{P_t G \sigma^0 A_{ft} L_1 L_2}{(4\pi h^2)^2} \tag{B.12}$$

here, L_2 represents the return path media loss. The total media path loss may therefore be given by $L_p = L_1 L_2$. The mean power intercepted by the altimeter antenna, P_r (the same antenna is used for transmitting and receiving pulses) with effective area, A_e is thus

$$P_r = \frac{P_t G^2 \sigma^0 A_{ft} A_e L_p}{16\pi^2 h^4}. \tag{B.13}$$

From standard antenna theory the *effective* rather than *physical* area of an antenna is a function of carrier wavelength, λ and gain, G. Here,

$$A_e = \frac{G\lambda^2}{4\pi} \tag{B.14}$$

and therefore

$$P_r = \frac{P_t G^2 \lambda^2 \sigma^0 A_{ft} L_p}{64\pi^3 h^4}. \tag{B.15}$$

Equation (B.14) is a form of the basic radar equation.

The *signal to noise ratio* (SNR) is a measure of received signal quality and is defined by the ratio

$$SNR = \frac{P_r}{P_n}. \tag{B.16}$$

P_n is the noise power of the receiver and is determined using standard communication theory. It is a combination of temperature, T, noise bandwidth, B and noise function of the receiver stage, F and is given by

$$P_n = kTBF \tag{B.17}$$

where, k is Boltzmanns constant (1.38×10^{-23} $\mathrm{WHz^{-1}K^{-1}}$). The standard SNR is unitless though may also be expressed in decibels. For the ith pulse of a radar the SNR is given by

$$\left(\frac{S}{N}\right)_i = \frac{P_r}{P_n} = \frac{P_t G^2 \sigma \lambda^2 L_p}{64\pi^3 h^4 kTBF} \tag{B.18}$$

For the Pulse-limited Altimeter, the ocean surface (or a semi-diffuse surface) illuminated is $A_{ft} = \pi hc\tau$, with c being the speed of light in a vacuum and τ, the

compressed pulse width. Hence,

$$\left(\frac{S}{N}\right)_{pla} = \frac{P_t G^2 \sigma^0 \lambda^2 c\tau L_p}{64\pi^2 h^3 kTBF} \tag{B.19}$$

For Beam–limited Altimeter operation the area illuminated is

$$A_{ft} = A_{blf} = \frac{\pi h^2 \lambda^2}{4d^2} \tag{B.20}$$

where, d is the antenna diameter and thus, the SNR is given by

$$\left(\frac{S}{N}\right)_{bla} = \frac{P_t G \sigma^0 \lambda^2 L_p}{256 h^2 P_n} \tag{B.21}$$

Finally, for completeness, illumination over ice–sheets gives rise to the quasi–specular radar equation. Here pulse incident at the ice surface are not scattered but reflected hence more power is incident back at the antenna. Analytically, it may be shown (see *Elachi*, 1988, for example) that a pulse travels a distance $2h$, backscatter is not incorporated for reasons just mentioned. However the effect of the first Fresnel zone, this is given by R_n and would typically be equivalent to -20 dB's. This value is specified for first–year ice and would degrade as the ice gets older. The resultant radar equation reduces to

$$\left(\frac{S}{N}\right)_{qs} = \frac{P_t G^2 \lambda^2 R_n L_p}{64\pi^2 h^2 P_n}. \tag{B.22}$$

Deriving a relationship over land is far more complex as land elevation, cover (i.e., vegetation, sandy and rocky cover all effect backscatter coefficient differently), etcetera and are hard to model. Also the altimeter is prone to *loss–of–track* over non–uniform topography.

Appendix C

Software for Mean Sea Surface and Gravity Anomaly Generation

C.1 Introduction

In this appendix a description of the software developed for global model mean sea surface (MSS), integrated MSS and gravity anomaly field generation is presented. Although, the software itself has been fully commented and is self explanatory it is deemed useful to describe the general functioning of the package. Additionally it is necessary to describe how to build the system of programmes with particular respect to the fact that a library has been developed to store a host of subroutines used by the package.

The programming language used for the software is FORTRAN–77 for the main reason of compatibility with other software written by the Aston Space Geodesy group. It should be noted, however, that although the majority of the programmes have been designed to optimise system performance, some in particular would benefit a great deal if they were to have access to such features like dynamic memory allocation and structuring, for example, available from the 'C' programming language. Such programmes that would most benefit from such features are identified.

To begin with a description how the software may be built is given followed by the role of the various libraries and then a description of each functional programme.

C.2 Building the Package

Before the package may be built it should be noted that none of the software may be compiled without access to the NAG library (Numerical Algorithms Group.)

The package is stored in a *Gnu* zipped (gzipped) tape archived (tar) file namely 'MSS.tgz'. The source code may be extracted and this will create the directory 'MSS' and a number of sub-directories containing the relevant code for the major stages of model development. The *Makefile*, found in the main 'MSS' directory, should be edited to reflect the local directory structure for software installation. In the first instance the two libraries (these are described in the next section) should first be compiled and installed by

```
make libs <ret>
make libs_install <ret>.
```

The entire package may be compiled and installed by

```
make all install <ret>
```

C.3 Library Description

There are three libraries required for use with software designed to develop global mean sea surfaces and gravity anomaly fields. These are

1. **libMSS.a** The mean sea surface library consists of the following subroutines

arr_add	Add two arrays of equal size
arr_add_const	Add constant to an array
arr_aver	Compute array mean
arr_copy	Copy an array
arr_scale	Scale an array
arr_sub	Subtract two arrays of equal size
cal2mjd	Converts calendar date to modified Julian date (MJD)
cartgeod	Cartesian to geodetic coordinates
csrtide	Computation of CSR ocean tides
dchols	Choleski matrix inversion
geodcart	Geodetic to cartesian coordinates
get_grav	Compute a geoid value from bi-linear interpolation
int_bil	Bi-linear interpolation
int_lag	Lagrange interpolation
int_lin	Linear interpolation
inv_bar	Standard Inverted Barometer computation
mjd2cal	Converts MJD to calendar character string (MJD)
open_da	Open condensed data record altimetry file
open_file	Open a file
opfor	Output preset formatted grid
opunfor	Output unformatted grid
pole_tide	Computation of the Pole tide
strme	Merge two character strings.

title	Display programme title details
utc2mjd	Universal time to MJD
utime	Universal time to local time
vector_add	Add two vectors
vector_mod	Vector modulus
vector_nor	Normalise a vector
vector_pro	Vector product
vector_sca	Scalar vector product
vector_sub	Subtract two vectors
weight	Gaussian distance weighting for grid point computation

2. **libnag.a** The components of the NAG library used are as follows:

C06FUF	Double precision 2–D FFT
C06GCF	Computation of gridded complex conjugate
E02BAF	Compute B–Spline using least squares fit
E02BBF	Compute spline value from B–Spline representation
X05AAF	Compute date and place result in character string
X05ABF	Used in conjunction with *X05AAF*
X05BAF	Compute CPU time.

3. **libFFT.a** The separate subroutines used for FFT determination are available from the Lincoln Laboratory, Massachusetts Institute of Technology. Here they have been gathered into a library. The subroutines are used mainly in the production of the gravity anomaly field and subsequent MSS integration procedures.

fourt	Main Singleton Fourier transform subroutine.
asmrv	Reverse indexes for non–symmetrical data.
symrv	Reverse indexes for symmetrical data.
factr	Find prime factors of an integer n.
fixrl	Convert doubled–up transform to true transform.
goert	Phase shifted FFT by Goertzel algorithm.
smfac	Arrange prime factors of n.
cool	Cooley–Tukey FFT method.

C.4 Mean Sea Surface Modelling Software

The procedure for developing the spectrally optimally interpolated MSS is shown in Figure 6.1. The model can be constructed by following the order of sub–sections.

C.4.1 Radial Orbit Error Minimisation

Radial orbit minimisation is provided for orbits computed at Aston university and Delft University of Technology. Three programmes exist.

resid_pre_proc.f: is used to pre–process dual–crossover residuals by removing any bias between T–E (TOPEX–ERS-1) and P–E (POSEIDON–ERS-1). A weak threshold option may be applied to remove highly incorrect residuals. The residuals are then split into T–E and P–E sets where a further bias is removed and statistics computed. The residuals are re–combined and finally sorted with respect to ERS-1 ephemeris.

resid_spline_fit.f: Fits a cubic B–Spline across an entire time–series of residual differences using the latitudinal weighting and iterative rejection method as described in chapter 6.

resid_alt_corr.f: Is an additional programme that will output the orbit error corrections at each altimeter data point. This serves as a diagnostic tool and in actuality a subroutine would be used to compute orbit corrections.

C.4.2 Gridding Software

alt_grid.f: Due to the large amount of data involved (17 million data points in the case of ERS-1) and the large size of grids it was necessary to optimise the gridding procedure described in chapter 6. This is achieved by splitting the gridding up into a number (this is a parameter variable) of segments, gridding each segment individually, and writing that segment to store. The unfortunate side to this is the need to read the altimetry the same number of times as there are segments. However, system resource requirements are significantly reduced when this approached as opposed to simply gridding over the globe in one exercise.

Additional sea height correction for radial orbit error is undertaken and filtering is performed to data and sea–surface variability is computed and removed. Sea–surface height gridding is achieved by binning data into 0.075° bins, corresponding to the maximum equatorial cross–track spacing for the ERS-1 geodetic phase, i.e., 4822 equator crossings. Each bin has a grid value calculated by the use of Gaussian distance weighting. Options exist to output data masks for shallow ocean and for regions of no data.

C.4.3 Residual MSS and Data Gap Fill

alt_fill.f: Two roles are performed in this programme. The first requires the generation of a residual surface to eventually develop the power spectral density of the noise resident in the first guess altimetric MSS. This is achieved by the removal of the EGM96 generated geoid and sea surface topography. Additional removal of some bad coastline data is achieved by a dual thresholding and Laplacian edge detection. A difference in geocenter is prominent in the resultant surface and do a four parameter fit is applied via the Least Squares method to correct for this effect.

Secondly all gridded regions void of data are filled with the EGM96 geoid plus sea surface topography model in order to reduce the effect Gibb's phenomenon at boundaries during the Fourier transforming stage.

C.4.4 Auto–Covariance Analysis

acvegm96.f: The global auto-covariance function describing the initial MSS estimate, $C_{h_0 h_0}$, was developed as detailed in section 6.4.1. EGM96 geoid error degree variances are calculated from potential error standard deviations, extrapolated to degree $n = 2400$ and the global ACV is constructed via equation 6.21 for all spherical angles over the globe. Options also exist to compute the power spectral density.
acvegm96_1d.f: A one dimensional version of the above is constructed for diagnostic use.

C.4.5 Fourier Optimal Interpolation

opt_int.f: This involves removing a long wavelength component of the signal and computing FFT's of the relevant parameters described in section 6.4. The spectral optimal estimator, A_{sl} is constructed from altimetric and model PSD's and applied to the spectral augmented altimetry. After adding back the original geoid and SST and optional high/low–pass filtering has taken place the resultant enhanced surface is transformed back to the spatial domain.

C.5 Mean Sea Surface Integration

Integration of data sets is described in chapters 7 and 8. The procedure allows the additional generation of the global gravity anomaly field.

C.5.1 GEOSAT Sea–Surface Height Correction

Software was written to correct and enhance the early releases of GEOSAT geodetic mission data and store corrected data in the condensed format described earlier. With the release of the enhanced GEOSAT data in 1997 (*Cheney*, 1997b) this software was upgraded.

gst_read.f both corrects and performs initial editing of the GEOSAT GDR's storing the results in a condensed format.

C.5.2 Slope Gridding

alt_grid_slope.f: This is essentially a version of *alt_grid.f* that additionally computes along–track vertical deflections, low–pass Gaussian filters the profiles to reduce high frequency noise, performs a threshold test to remove erroneous deflections and finally grids the data into ascending and descending slopes.

C.5.3 Deflection of the Vertical Generation

dov.f: The globally gridded ascending/descending vertical deflections are converted to eastern and northern DOV components using theory described in chapter 7.

C.5.4 DOV to Gravity Anomaly or MSS

conv_dov.f: Two options are available here, where either a gravity anomaly field or mean sea surface may be computed. Conventional vertical deflection components are converted to the spectral domain, combined using the inverse Vening–Meinsz transform to form a spectral gravity anomaly. The resultant grid may be filtered and converted to a spatial gravity anomaly as described in chapter 7. Alternatively the spectral gravity anomaly may be converted via the forward Stokes' transform to a residual MSS. An option exists to re–establish the EGM96 geoid to degree 360 and the 20 by 20 sea surface topography.

C.5.5 MSS Data Set Integration

mss_int.f: Two residual MSS models are converted to the spectral domain (unless they have already been transformed.) Options are available to either fix the two models and compute an average in the spectral domain. Alternatively, one model may be fixed whilst the other has a weighting computed via high–pass filtering the spectral signal (see chapter 8). The resultant signal is determined combining to

two signals via a weighted average, converted to the spatial domain where geoid and sea surface topography models are added back to give the integrated surface.

C.6 Analysis Software

analysis.f: A range of analysis software was written to validate both versions of MSS against TOPEX ERS-1 and GEOSAT sea surface heights.
ship_comp.f: Here gravity anomaly profiles are compared against single ship–board profiles. The profiles are taken from the GEODAS database and are stored in the MGD77 (Marine Geophysical Data Exchange Format 1977) format. After retrieving the gravity anomaly profile a comparison is made at each point via the bi–linear interpolation of the satellite produced gravity anomaly field. A bias is removed with respect to the global gravity field and an RMS value produced alongside output files for ship, interpolated satellite profiles and their differences.

C.7 Regional Gravity Anomaly Construction

Regional gravity anomaly fields may be produced for either GEOSAT or ERS-1 in addition to global gravity anomaly determination described above. The purpose here allows very fast gravity anomaly determination.
dov_reg.f: Produces grids of ascending/descending deflections and northern/eastern deflections of the vertical.
grav_anom_reg.f: Gravity anomalies are produced from the deflections of the vertical.

Appendix D

Regional Gravity Anomaly Field Images

Twelve regional gravity anomaly images are displayed in Figures D.2 and D.13. The gravity anomaly field determination proceedure is described in chapter 7 and the images are formed from Fig. 7.12. The twelve regions are displayed below in Figure D.1.

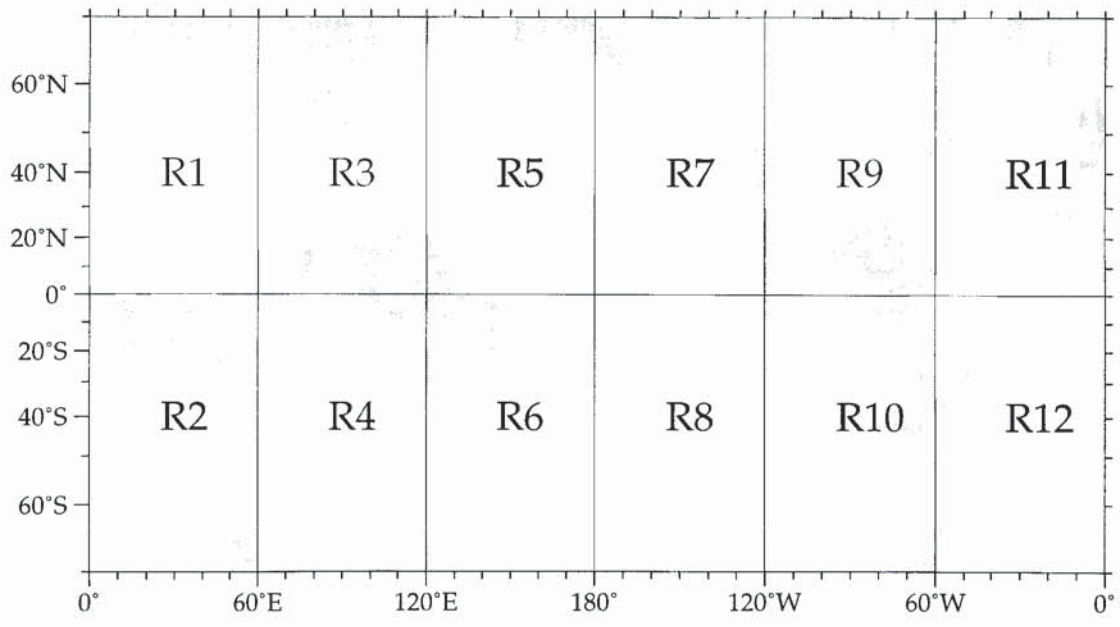

Figure D.1: Gravity anomaly image regions 1 to 12 (R1–R12).

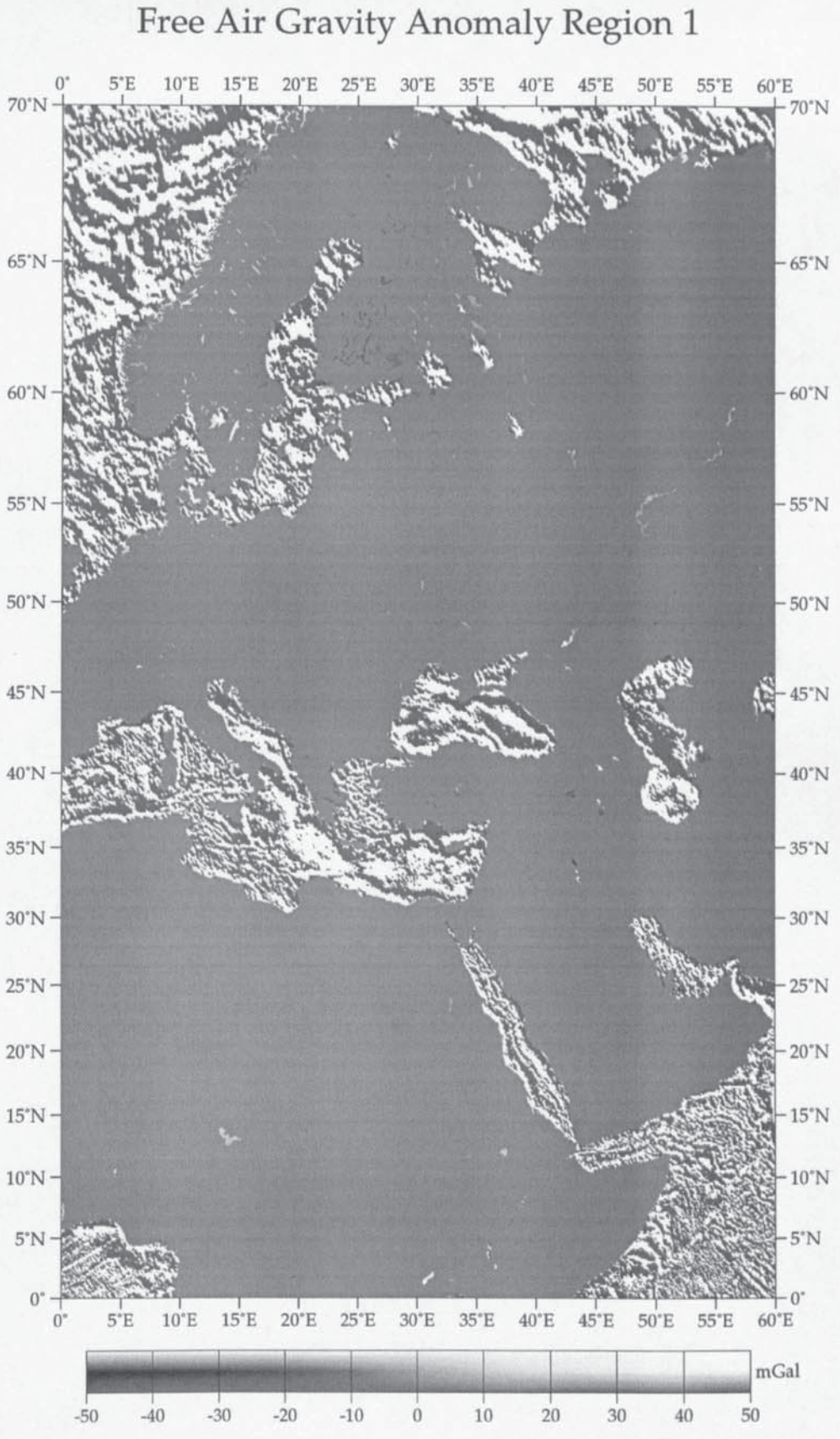

Figure D.2: Gravity anomaly for region 1.

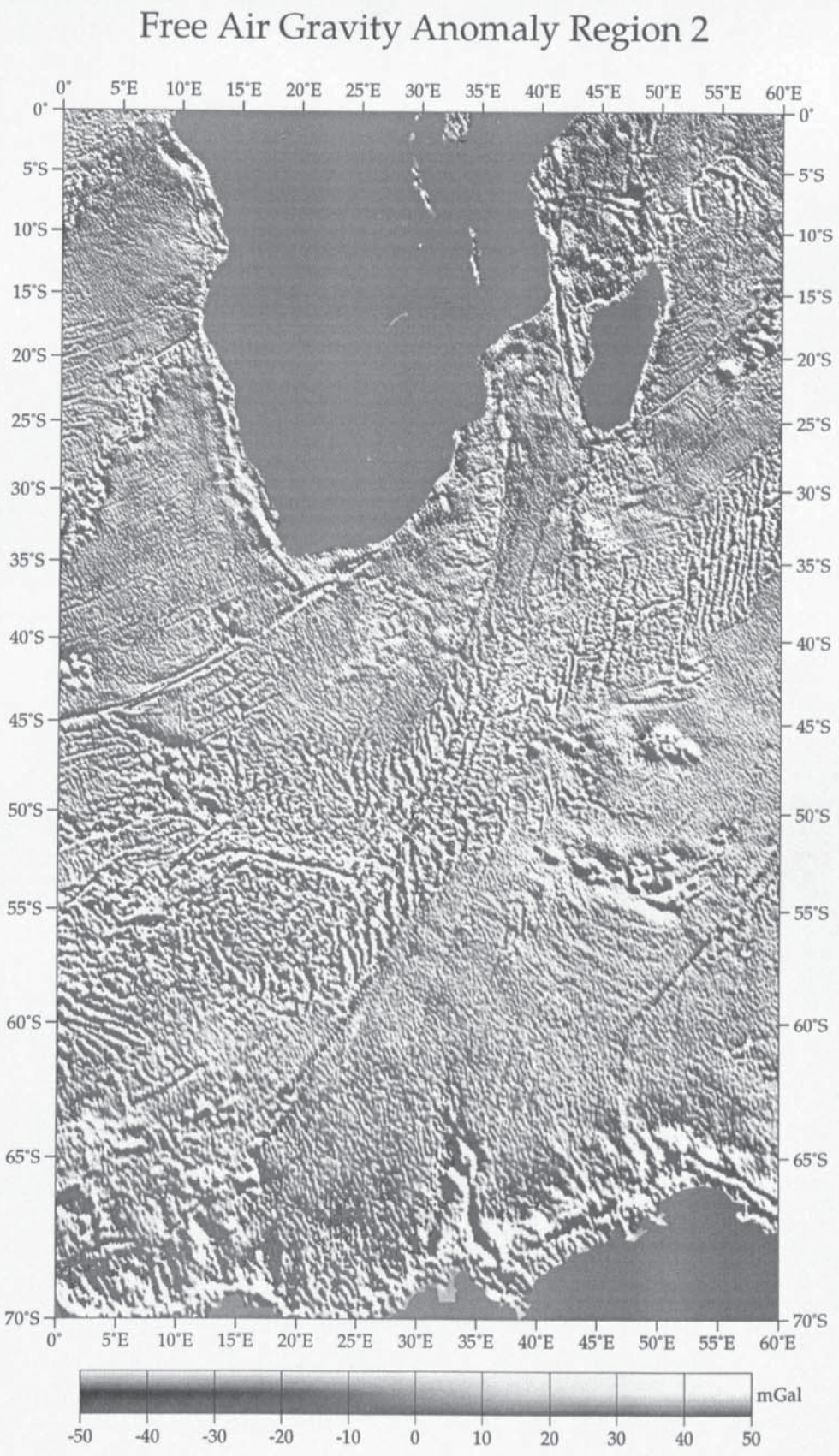

Figure D.3: Gravity anomaly for region 2.

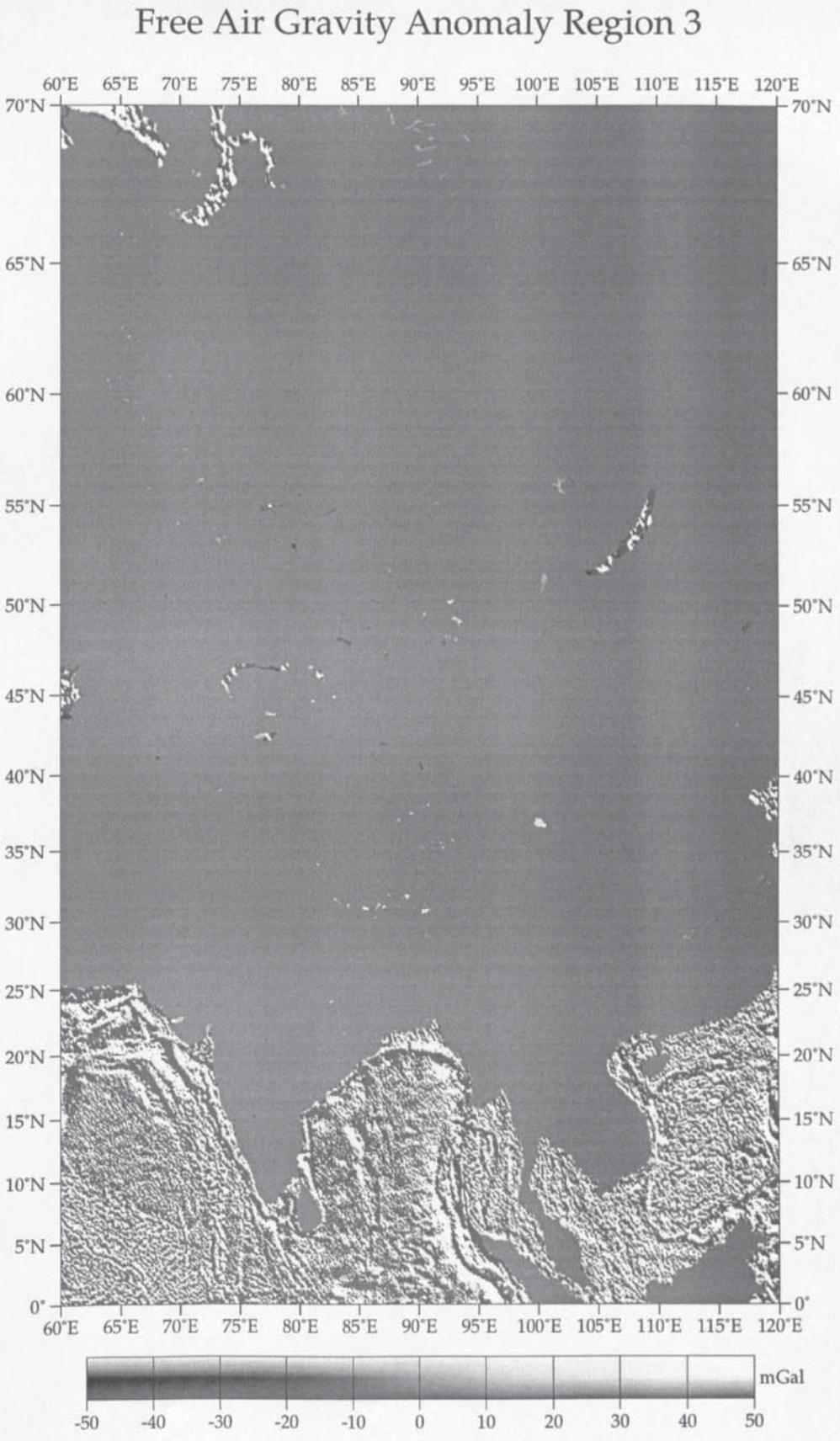

Figure D.4: Gravity anomaly for region 3.

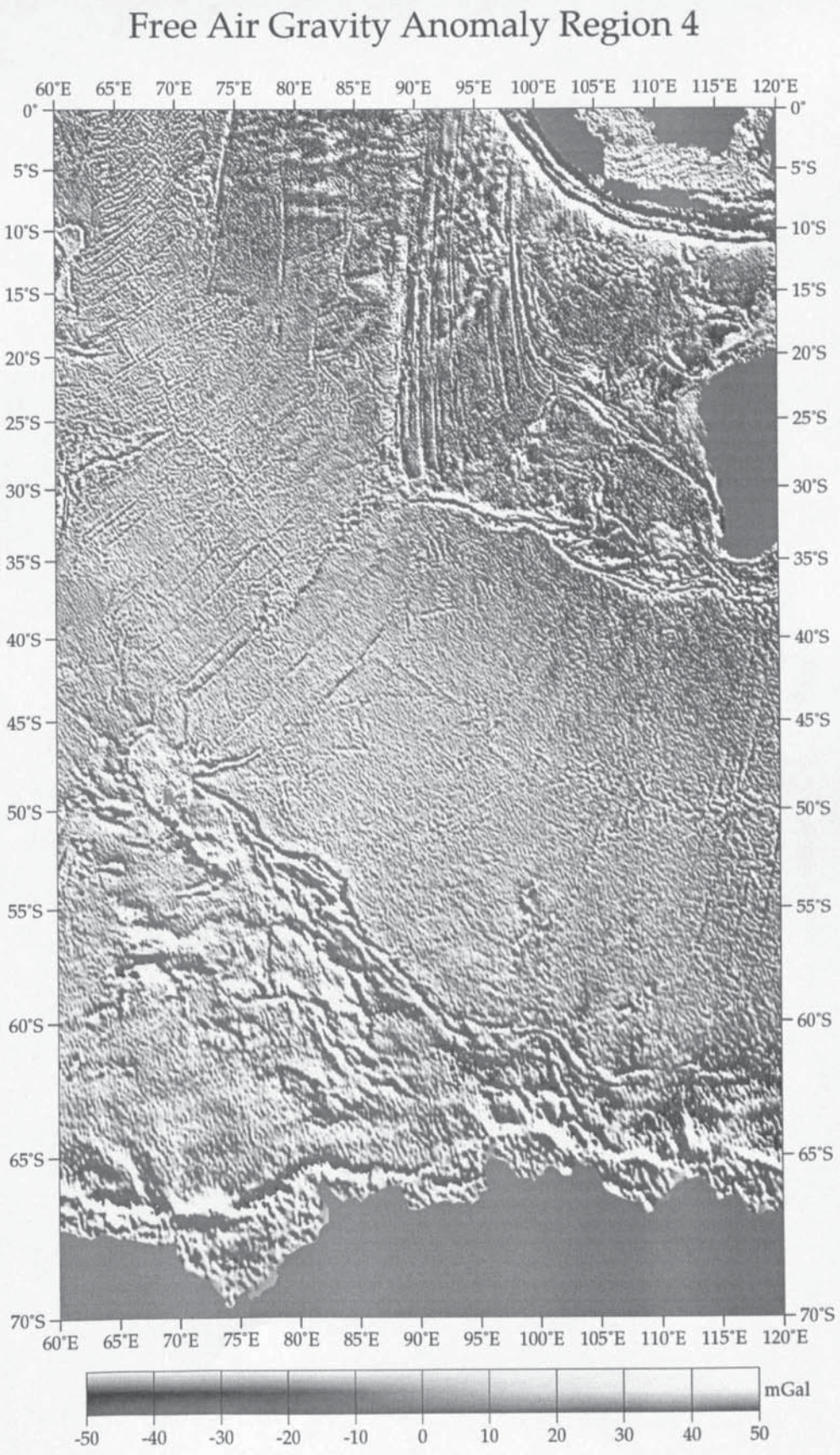

Figure D.5: Gravity anomaly for region 4.

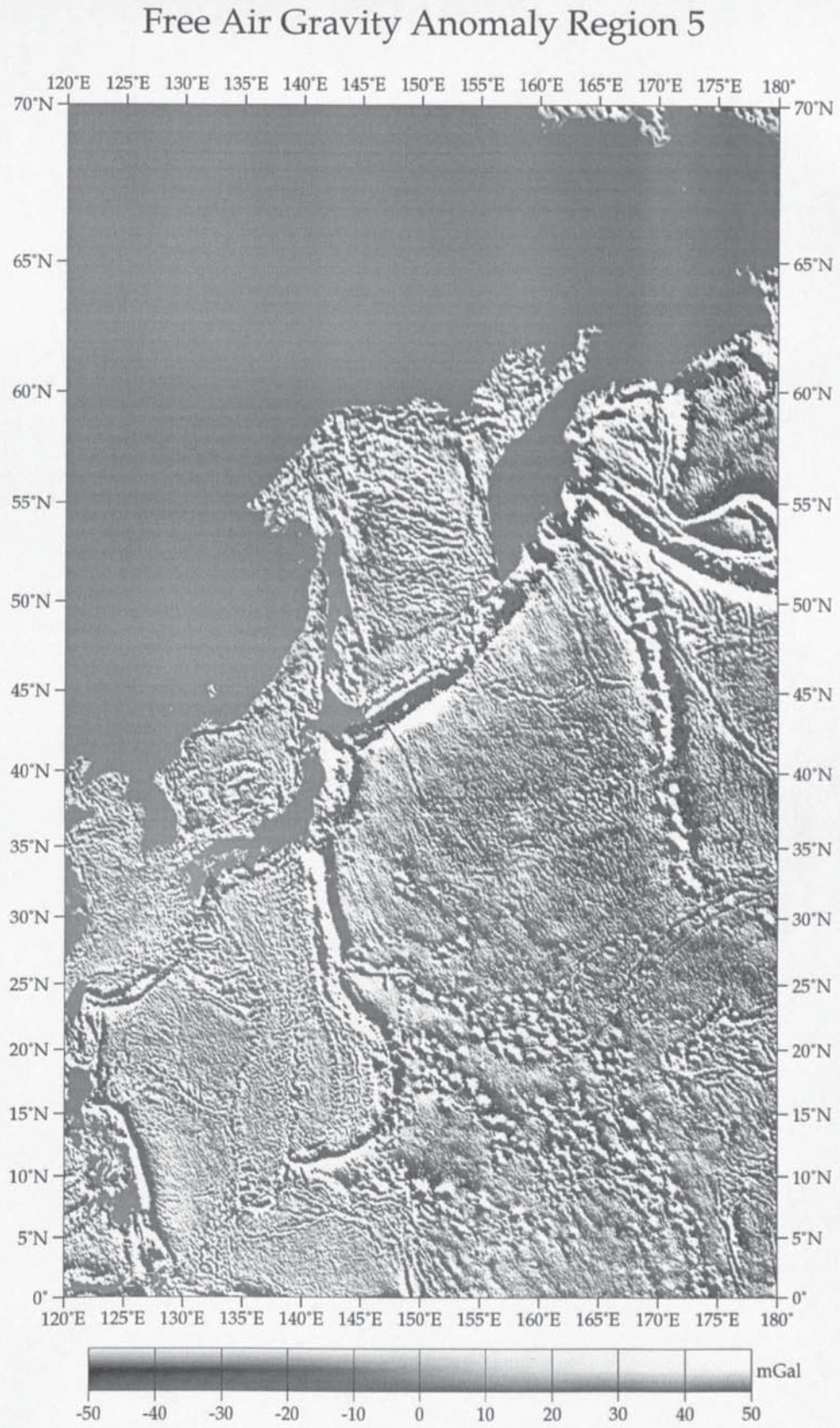

Figure D.6: Gravity anomaly for region 5.

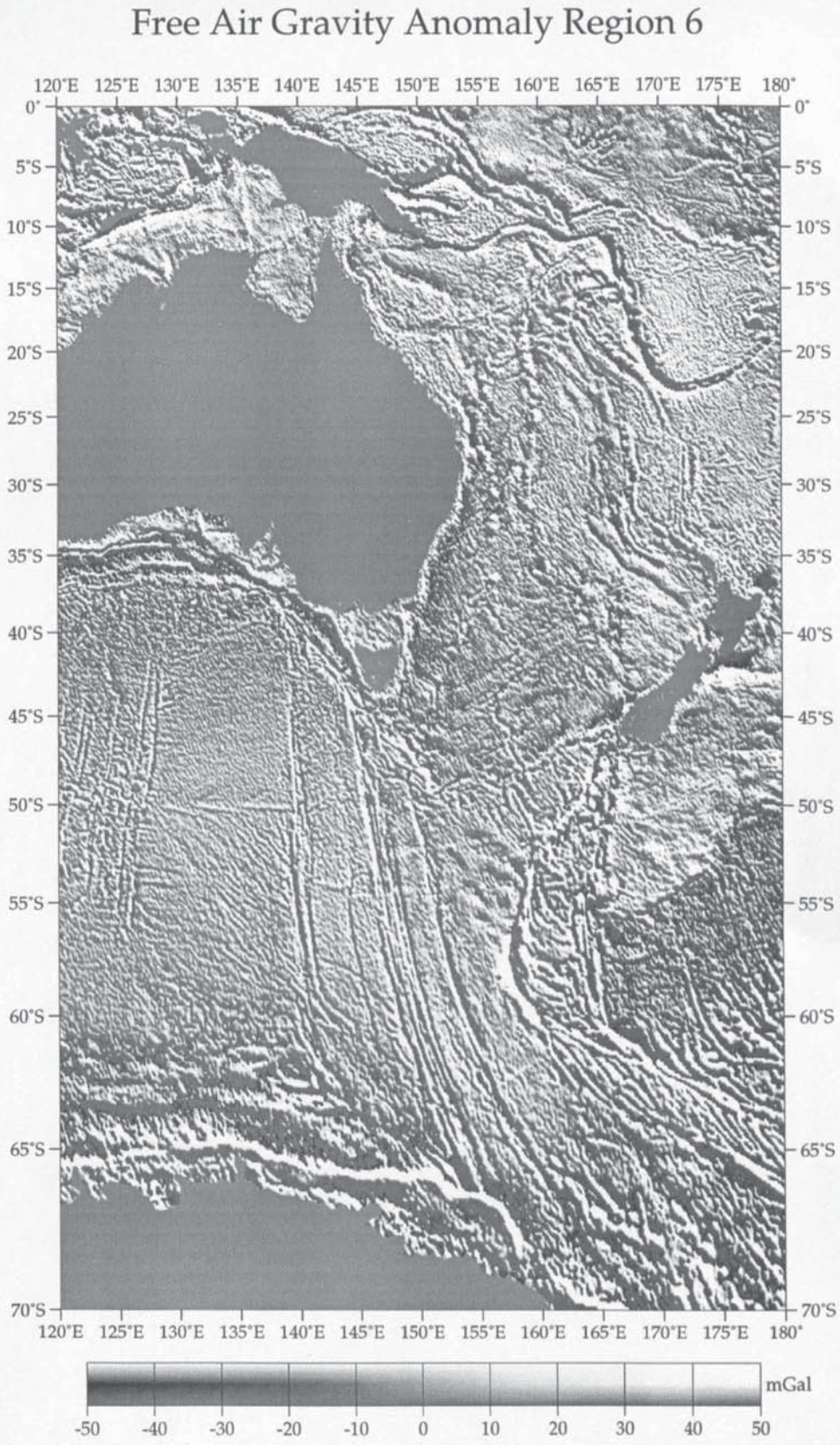

Figure D.7: Gravity anomaly for region 6.

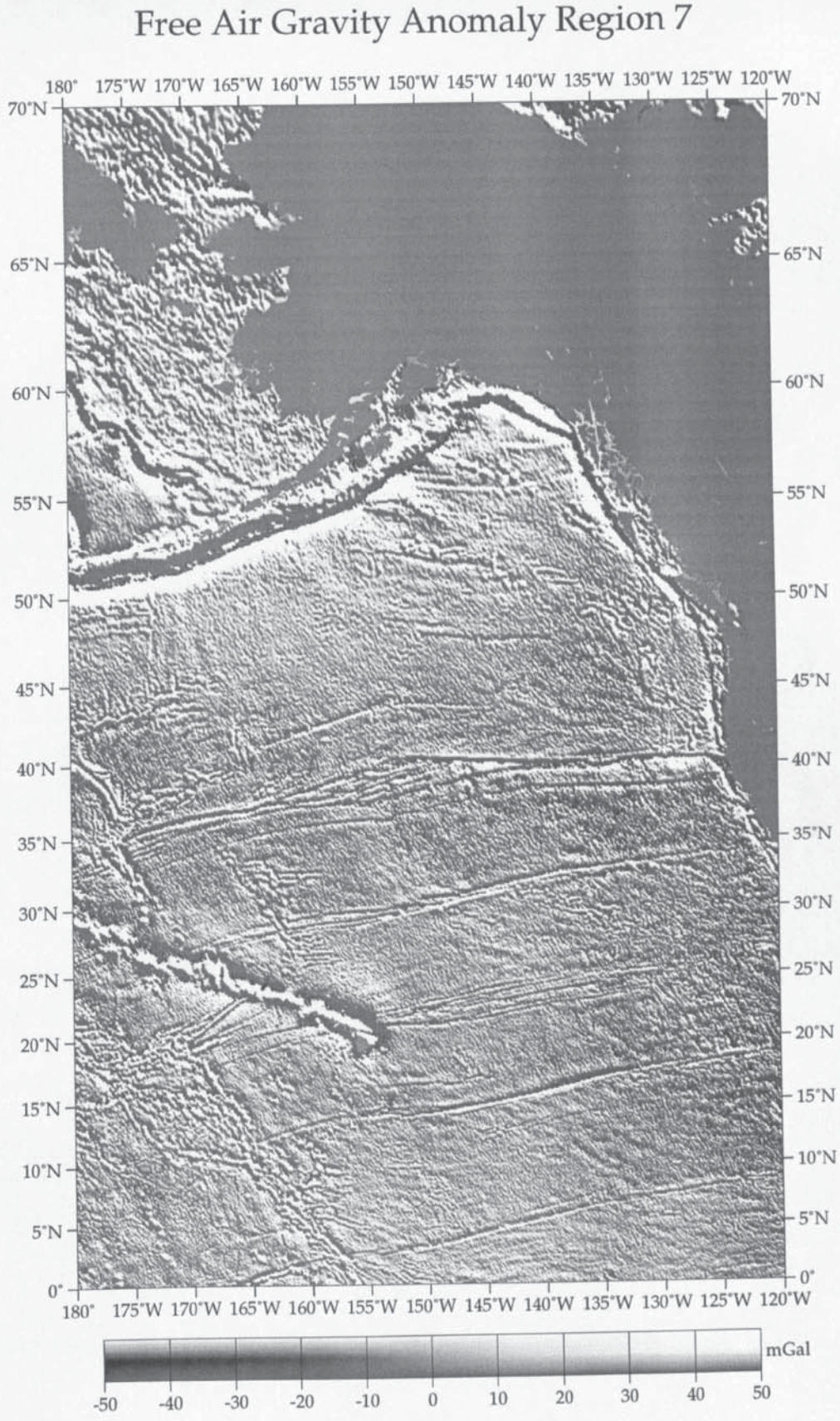

Figure D.8: Gravity anomaly for region 7.

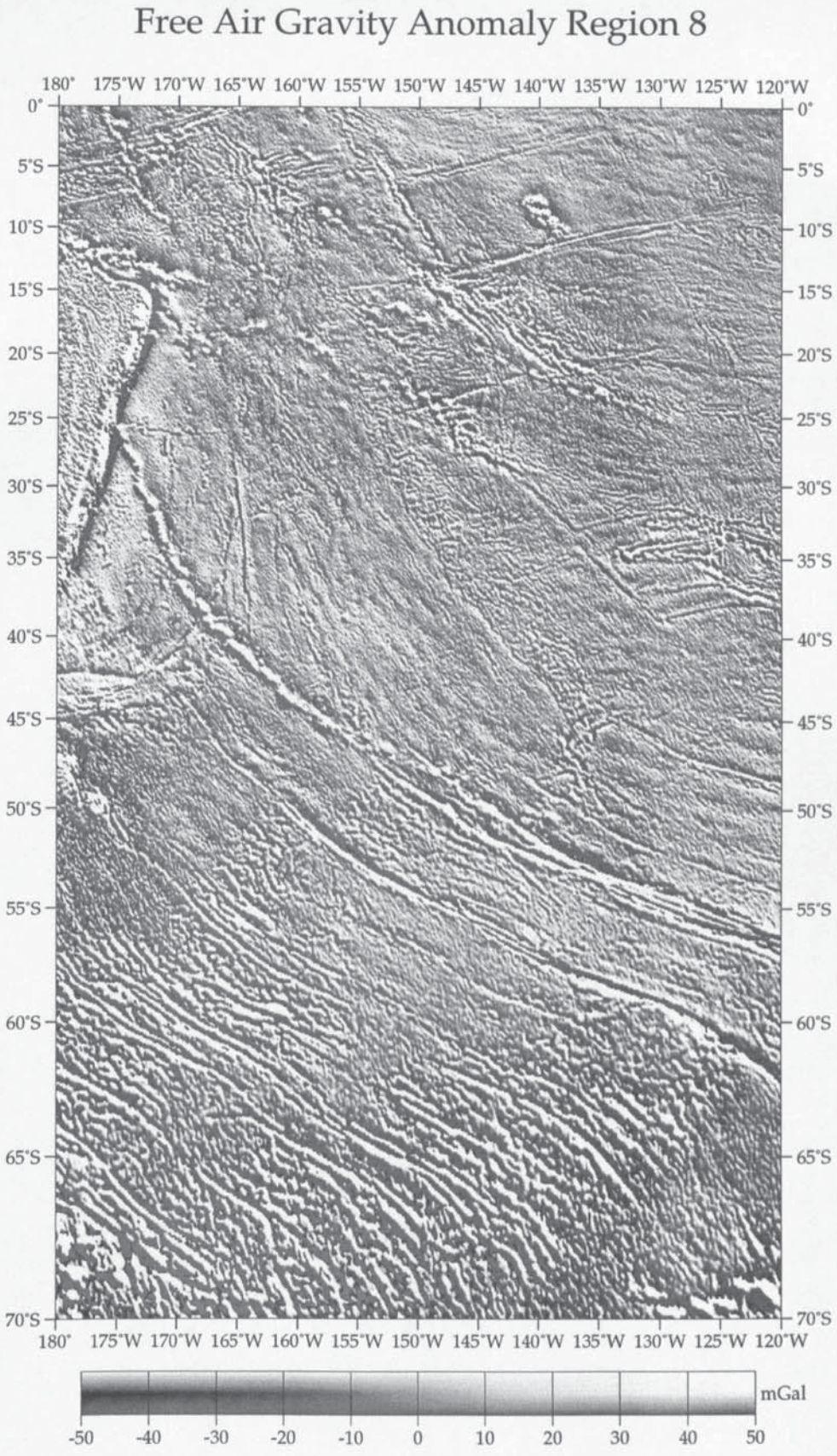

Figure D.9: Gravity anomaly for region 8.

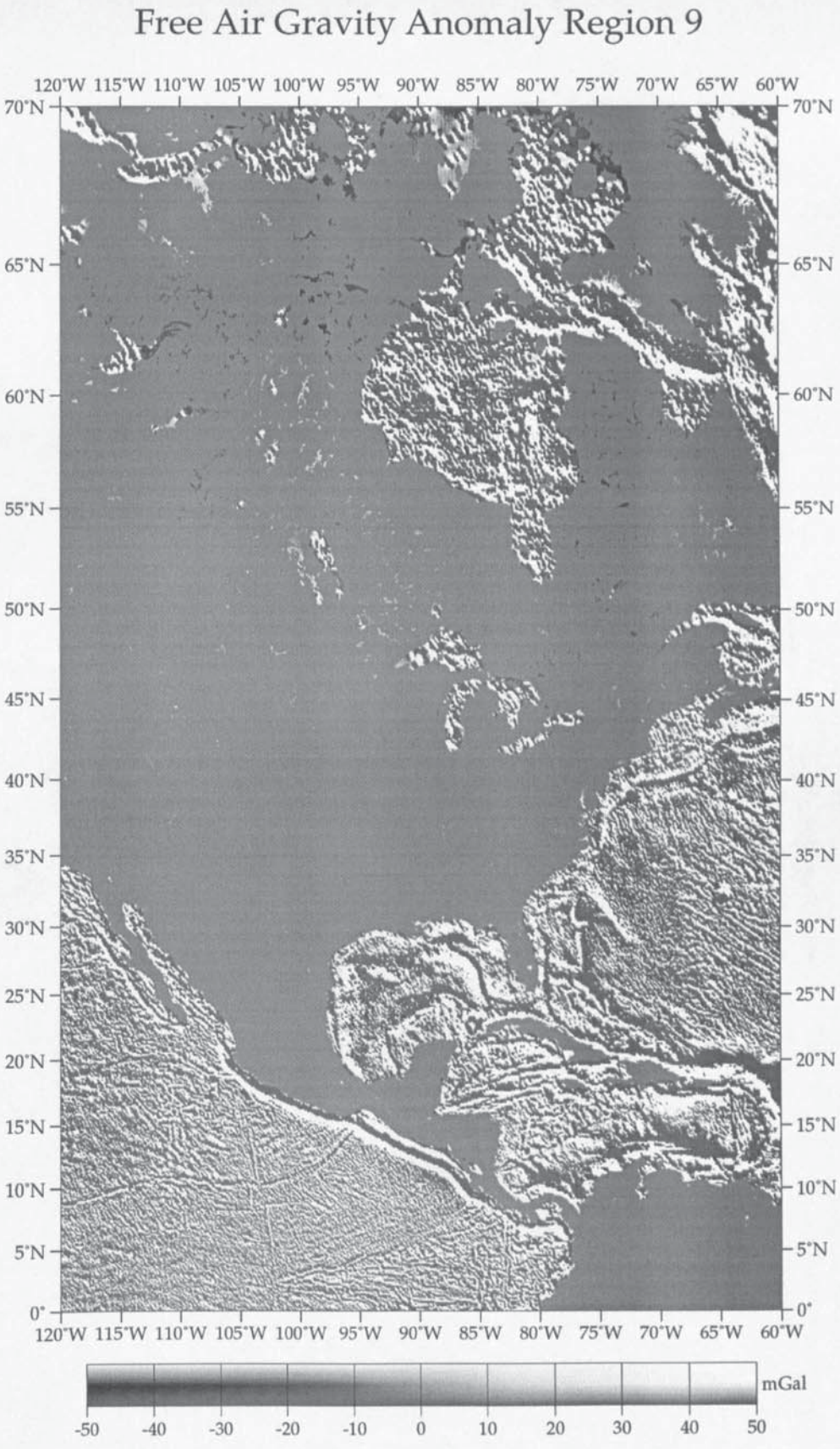

Figure D.10: Gravity anomaly for region 9.

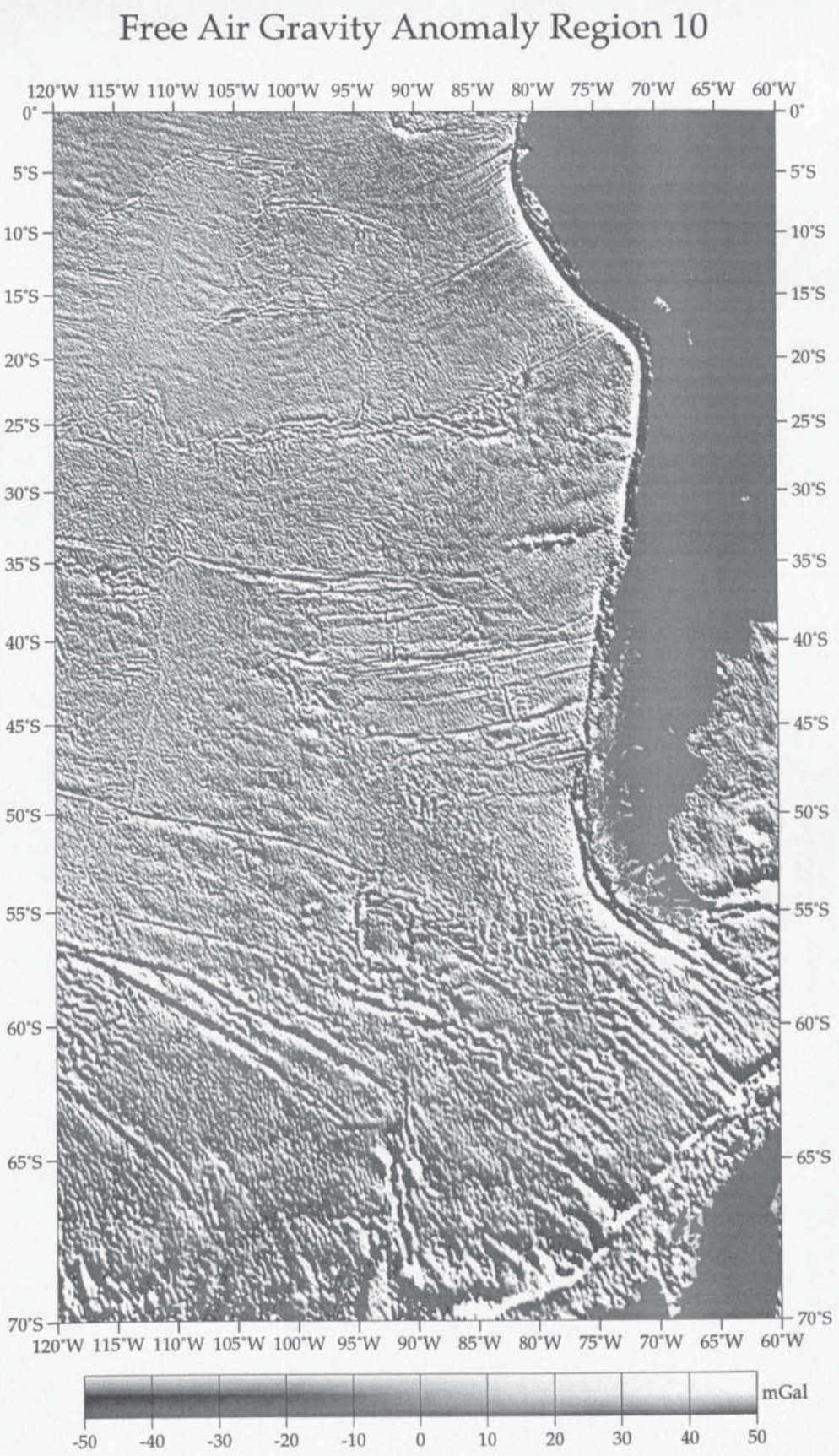

Figure D.11: Gravity anomaly for region 10.

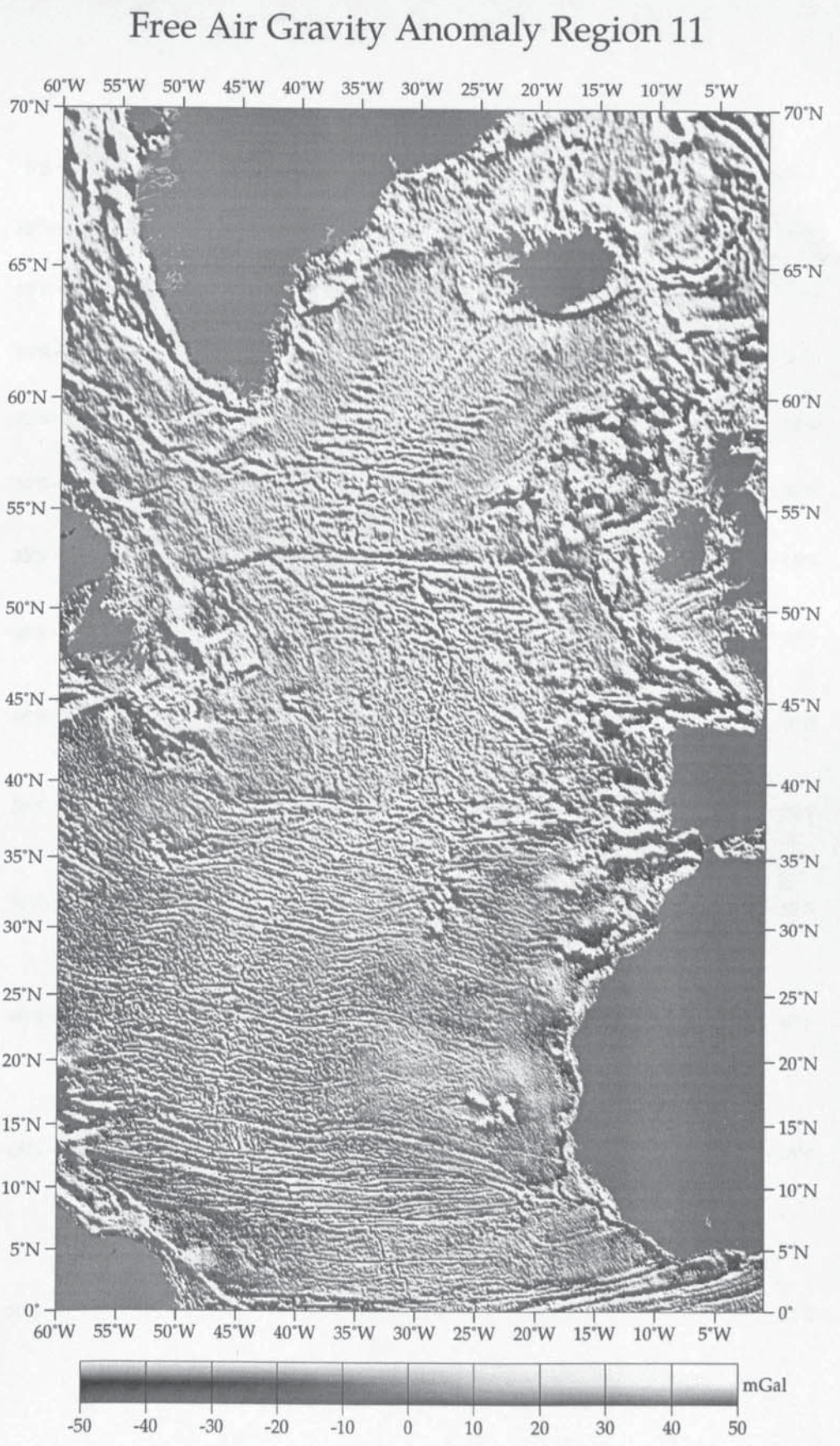

Figure D.12: Gravity anomaly for region 11.

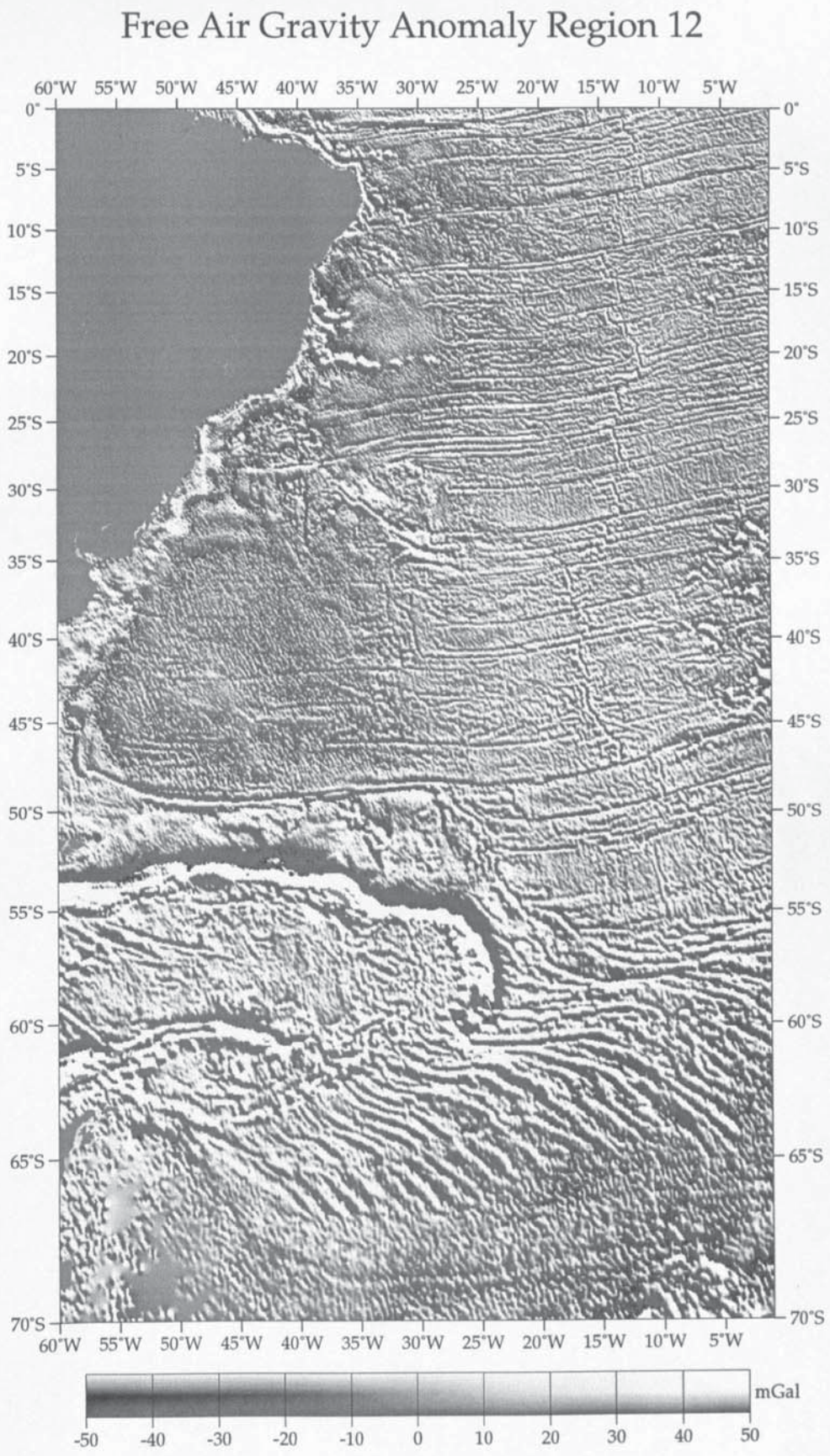

Figure D.13: Gravity anomaly for region 12.

References

Andersen, O. B. and *Knudsen, P.*, 1998: Global marine gravity field from the ERS-1 & GEOSAT geodetic mission altimetry. *Journal of Geophysical Research*, **C4**(103):8129–8137.

Anderson, O. B. and *Knudsen, P.*, 1995: Global altimetric gravity map from the ERS-1 geodetic mission (cycle 1). *Earth Observ. Quart.*, **47**:1–5.

Asrar, G. and *Greenstone, R.*, 1995: *MTPE EOS reference handbook.* NASA Goddard Space Flight Center, Greenbelt, MD 20771.

AVISO, 1996: *Archiving, validation and interpretation of satellite oceanography, AVISO handbook for merged TOPEX/Poseidon products. AVI-NT-02-101-CN.* Toulouse, France, third edn.

Bean, B. R. and *Dutton, E. J.*, 1966: Radio Meterology. *National Bureau of Standards Monograph*, **92**.

Bent, R. B., Llewellyn, S. K., Nesterczuk, G. and *Schmid, P. E.*, 1975: The development of a highly-successful world-wide empirical ionospheric model and its use in certain aspects of space communications and world-wide total electron content investigations. In *Proc. Symp. Effect of the ionosphere on Space Systems and Communications*. Naval Research Laboratory, Arlington VA, pp. 23–38.

Bilitza, D., Koblinsky, C., Beckley, B., Zia, S. and *Williamson, R.*, 1995: Using IRI for the computation of ionospheric corrections for altimeter data analysis. *Advances in Space Research*, **15**(2):113–119.

Blanc, F., Houry, S., Mazzega, P. and *Minster, J. F.*, 1990: High resolution, high accuracy altimeter derived mean sea surface in the Norwegian sea. *Marine Geodesy*, **14**:57–76.

Bracewell, R., 1978: *The Fourier transform and its applications.* McGraw-Hill Book Company, New York, second edn.

Brown, G. S., 1977: The average impulse response of a rough surface and its applications. *IEEE Trans. Antennas and Prop.*, **AP-25**(1):67–74.

Carnochan, S., 1997: *Altimeter and orbit corrections for the ERS satellites through the analysis of single and dual satellite crossovers.* Ph.D thesis, University of Aston in Birmingham.

Cartwright, D. E. and *Ray, R. D.*, 1991: Oceanic tides from GEOSAT altimetry. *Journal of Geophysical Research*, **95**:3069.

Cazenave, A., 1994: The geoid and oceanic lithosphere. In *Geoid and its geophysical interpretations*, edited by P. Vaníček and N. T. Christou, CRC Press, Boca Raton, Florida, chap. 13, pp. 255–283. First edn.

Cazenave, A., Parsons, B. and *Calcagno, P.*, 1995: Geoid lineations of 1000 km wavelength over the Central Pacific. *Geophys. J. Int.*, **22**(2):97–100.

Cazenave, A., Schaeffa, P., Berge, M., Brossier, C., Dominh, K. and *Gennero, M. C.*, 1996: High-Resolution mean sea surface computed with altimeter data of ERS-1 (geodetic mission) and TOPEX/Poseidon. *Geophys. J. Int.*, **125**:696–704.

Chelton, D. B., Walsh, E. J. and *MacArthur, J. L.*, 1989: Pulse compression and adaptive height tracking in satellite altimetry. *J. Atmos. Oceanic Technol.*, **6**:407–438.

Cheney, R. E., 1997a: Personal Communication.

Cheney, R. E., 1997b: *The GEOSAT altimeter JGM3 GDR's on CDROM.* Technical manual, NODC laboratory, NOAA, Silver Spring, Maryland 20910.

Cheney, R. E., 1997c: *The GEOSAT altimeter online handbook.* online manual, NODC laboratory, NOAA, Silver Spring, Maryland 20910. (available on–line at 'http://www.nodc.noaa.gov/NODC-cdrom.html#geosatj3').

Cheney, R. E., Doyle, N. S., Douglas, B. C., Agreen, R. W., Miller, L., Timmerman, E. L. and *McAdoo, D. C.*, 1991: *The Complete GEOSAT Altimeter GDR handbook.* Technical Manual NOS NGS 7, Geodetic Research and Development Laboratory, National Geodetic Survey, NOAA, Rockville, MD.

Cooley, J. W. and *Tukey, J. W.*, 1967: An algorithm for the machine calculation of complex Fourier series. *Math. Comput.*, **90**(19):297–301.

Cudlip, W., Mantripp, D. P., Wrench, C. L., Griffiths, H. D., Sheehan, D. V., Lester, M. and *Leigh, R. P.*, 1994: Corrections for Altimeter low–level processing at the Earth Observation Data Centre. *Int J. Remote Sensing*, **15**(4):889–914.

Cullen, R., Moore, P. and *Reynolds, M.*, 1997: Global altimetric mean sea surface derived from the geodetic phase of the ESA ERS-1 mission utilising a spectral least squares collocation technique. In *Proceedings of the Third ERS-1 Symposium: ESA SP-414*, edited by T. D. Guyenne and D. Danesy. ESA, ESTEC Publications Division, Noordwijk The Netherlands, vol. 3, pp. 1553–1557. (Also available via online at 'http://florence97.ers-symposium.org/' and CDROM).

Davis, C. H., 1992: Satellite radar altimetry. *IEEE Trans. Micro. Theory and Tech.*, **49**:1070–1076.

Eanes, R. J. and *Bettadpur, S. V.*, 1995: *The CSR3.0 global ocean tide model.* Tech. Rep. CSR–TM–95–06, Centre for Space Research, University of Texas at Austin, Texas, USA.

Elachi, C., 1988: *Spaceborne radar remote sensing: Applications and techniques.* IEEE Press, New York.

ESA, 1997: *ENVISAT-1 mission & system summary.* Technical report, ESA.

Eymard, L., Cornec, A. L. and *Tabary, L.*, 1994: The ERS-1 Microwave Radiometer. *Int J. Remote Sensing*, **15**(4):845–857.

Finkelstein, J., 1997: GFOmission design. available online at 'http://gfo.bmpcoe.org/Gfo/Mission/missiond.htm'.

Foufoula-Giorgiou, E. and *Kumar, P.*, 1994: *Wavelets in Geophysics.* Academic Press, New York, USA.

Fowler, C. M. R., 1990: *The solid Earth - An introduction to global geophysics.* Cambridge University Press, Cambridge, UK, first edn.

Gaspar, P., Ogor, F. and *Hamdaoui, M.*, 1996: *Analysis and estimation of the GEOSAT sea state bias.* Report 96–3056–K1196, Hughes/STX, Greenbelt, MD, USA.

Gaspar, P., Ogor, F., Le Traon, P. Y. and *Zanife, O. Z.*, 1994: Estimating the sea state bias of the TOPEX and Poseidon altimeters from crossover differences. *Journal of Geophysical Research*, **99**:24981–24994.

Gill, A. E. and *Niiler, P. P.*, 1973: The theory of the seasonal variability in the ocean. *Deep Sea Res.*, **20**:141–177.

Glazmann, R. E., Greysukh, A. and *Zlotnicki, V.*, 1994: Evaluating models of sea state bias in satellite altimetry. *Journal of Geophysical Research*, **99**(C6):12581–12591.

Grafarend, E. W., 1994: What is a geoid? In *Geoid and its geophysical interpretations*, edited by P. Vaníček and N. T. Christou, CRC Press, Boca Raton, Florida, chap. 1, pp. 3–32. First edn.

Griffifths, H. D., 1994: Personal Communication.

Griffiths, H. D., 1988: Synthetic aperture processing for full-deramp radar altimeters. *Electronic Letters*, **24**(7):371–373.

Haxby, W. F., Karner, G. D., Brecque, J. L. L. and *Weissel, J. K.*, 1983: Digital images of combined oceanic and continental data sets and their use in tectonic studies. *EOS Trans. Am. Geophys. Un.*, **64**:995–1004.

Hayes, J. G., 1974: Numerical methods for curve and surface fitting. *J. Inst. Maths Applics.*, **10**:144–152.

Hayling, K. L., 1994: The geoid and geophysical prospecting. In *Geoid and its geophysical interpretations*, edited by P. Vaníček and N. T. Christou, CRC Press, Boca Raton, Florida, chap. 15, pp. 299–319. First edn.

Heiskanen, W. A. and *Moritz, H.*, 1967: *Physical geodesy.* W. H. Freeman and Co., San Fransisco, California, USA. 364 pp.

Houghton, J. T., 1991: *The physics of atmospheres.* Cambridge University Press, Cambridge, U.K., second ed. edn.

Hwang, C. and *Parsons, B.*, 1995: Gravity anomalies derived form SEASAT, GEOSAT, ERS-1 and TOPEX/Poseidon altimetry and ship gravity: a case study over the Reykjanes Ridge. *Geophys. J. Int.*, **122**:551–568.

Hwang, C. and *Parsons, B.*, 1996: An optimal procedure for deriving marine gravity from multi–satellite altimetry. *Geophys. J. Int.*, **125**:705–718.

Jolly, G., 1995: *Satellite borne radar altimetry, empirical orbit refinement and ocean signal recovery techniques.* Ph.D thesis, University of Aston in Birmingham.

Jolly, G. W. and *Moore, P.*, 1996: Analysis of global ERS-1 altimetry by optimal Fourier transform interpolation. *Marine Geodesy*, **19**:331–357.

Kalnay, E., 1996: The NCEP/NCAR 40–year re–analysis project. *Bull. American Mathematical Society*, **77**(3):437–471.

Kaula, W., 1970: *Satellite altimetry for the future.* Tech. rep., NASA.

Kaula, W. M., 1966: *Theory of satellite geodesy.* Blaisdell Publishing Co., Waltham, Massachusetts. 124 pp.

Kim, M. C., 1993: *Determination of high resolution mean sea surface and marine gravity field using satellite altimetry.* Ph.D thesis, University of Texas at Austin.

Kim, M. C., Shum, C. K. and *Tapley, B. D.*, 1994: An altimetric mean sea surface and its spectral analysis. In *Proceedings of the second ERS-1 symposium: space at the service of our environment, ESA SP-361*. ESA.

Kingsley, S. and *Quegan, S.*, 1992: *Understanding radar systems.* McGraw-Hill Book Company, London, UK, first edn. pp 375.

Klobuchar, J. A., 1987: Ionospheric time-delay algorithm for single-frequency GPS users. *IEEE Trans. Aerosp. Elect. Syst.*, **AES-23**:325–331.

Lam, C. W. and *Moore, P.*, 1995: A study of sea surface variability in the southern oceans using ERS-1 altimetry. In *RSS* 95 – *Remote sensing in action. Proceedings of the* 21*st annual conference of the Remote Sensing Society.*, edited by P. J. Curran and C. Robertson. University of Southampton, pp. 78–85.

Lawrence, R. S., 1964: A survey of ionospheric effects upon Earth space radio. *Proc. IEEE.*, **52**(1):4–27.

Laxon, S., 1994: Sea ice altimeter processing scheme at the EODC. *Int J. Remote Sensing*, **15**(4):915–924.

Laxon, S. W. and *McAdoo, D.*, 1994: Arctic ocean gravity field derived from ERS-1 satellite altimetry. *Science*, **256**:621–624.

Le Provost, C., Genco, M. L., Lyard, F., Vincent, P. and *Canceil, P.*, 1994: Spectroscopy of the world ocean tides from a finite element hydrodynamic model. *Journal of Geophysical Research*, **99**:24777–24797.

Le Traon, P., Gaspar, P., Bouyssel, F. and *Makhmaraa, H.*, 1995: Use of TOPEX/Poseidon data to enhance ERS-1 data. *J. Atmos. Oceanic Technol.*, **12**:161–170.

Le Traon, P.-Y. and *Ogor, F.*, 1998: ERS-1 orbit improvement using TOPEX/-Poseidon: The 2 cm. Challenge. *Journal of Geophysical Research*, **103**(C4):8045–8057.

Lemoine, F. G., Smith, D. E., Kunz, L., Smith, R., Pavlis, E. C., Pavlis, N. K., Klosko, S. M., Chinn, D. S., Torrence, M. H., Williamson, R. G., Cox, C. M., Rachlin, K. E., Yang, Y. M., Kenyon, S. C., Salman, R., Trimmer, R., Rapp, R. H. and *Nerem, R. S.*, 1996: The Development of the NASA GSFC and NIMA Joint Geopotential Model. In *Proceedings for the International Symposium on Gravity, Geoid, and Marine Geodesy, (GRANGEOMAR 1996), Tokyo, Sept 30 - Oct 5, 1996*. Springer Verlag.

Levitt, D. A. and *Sandwell, D. T.*, 1995: Lithospheric bending at subduction zones based on depth soundings and satellite gravity. *Journal of Geophysical Research*, **100**(B1):379–400.

Lillibridge, J., 1997: Personal Communication.

Marsh, J., 1990: The GEM-T2 gravitational model. *Journal of Geophysical Research*, **95**:22043–22072.

Marth, P. C., Jensen, J. R., Kilgus, C. C., Perschy, J. A., MacArthur, J. L., Hancock, D. W., Hayne, G. S., Purdy, C. L., Rossi, L. C. and *Koblinsky, C. J.*, 1993: Prelaunch performance of the NASA altimeter for the TOPEX/Poseidon project. *IEEE Trans. Geosci. Remote Sens.*, **31**(2):315–332.

Mattok, C., ed., 1991: *The Solid-Earth Mission ARISTOTLES ESA SP-329*, Noordwijk, The Netherlands. ESA, ESTEC.

Mazzega, P. and *Houry, S.*, 1989: An experiment to invert SEASAT altimetry for Mediterranean and Black Sea mean surfaces. *Geophys. J.*, **96**:259–272.

McAdoo, D. and *Laxon, S. W.*, 1997: Antarctic tectonics: constraints from a new ERS-1 satellite marine gravity field. *Science*, **276**(5312):556–561.

McAdoo, D. C., 1990: Gravity field of the southeast central Pacific from Geosat exact repeat mission data. *Journal of Geophysical Research*, **95**:3041–3047.

McAdoo, D. C. and *Marks, K. M.*, 1992: Gravity fields of the southern ocean from GEOSAT data. *Journal of Geophysical Research*, **97**(B3):3247–3260.

McGoogan, J. T., 1975: Satellite Altimetry Applications. *IEEE Trans. Micro. Theory and Tech.*, **MTT–23**(12):970–978.

McGoogan, J. T., Miller, L. S., Brown, G. S. and *Hayne, G. S.*, 1974: The S-193 radar altimeter experiment. *Proc. IEEE*, **62**:793–803.

Monaldo, F., 1993: TOPEX ionospheric height correction precision estimated from prelaunch test results. *IEEE Trans. Geosci. Remote Sens.*, **31**(2):371–375.

Moore, R. K. and *Williams, C. S.*, 1957: Radar terrain return at near–vertical incidence. *Proc. IRE*, **45**:228–238.

Moritz, H., 1980: *Advanced Physical Geodesy*. H Wichmann, Heidelberg, Germany. 500 pp.

Nash, R. A. and *Jordan, S. K.*, 1978: Statistical geodesy - An engineering perspective. *Proc. IEEE*, **66**(5):532–550.

Nerem, R. S., 1995: Global mean sea level variations from TOPEX/Poseidon altimeter data. *Science*, **268**:708–710.

Nerem, R. S., 1997: Global mean sea level change: Correction. *Science*, **275**:1053.

Nerem, R. S., Tapley, B. D. and *Shum, C. K.*, 1990: Determination of the ocean circulation using GEOSAT altimetry. *Journal of Geophysical Research*, **95**(C5):3163–3179.

Parke, M. E., Born, G., Leben, R., McLaughlin, C. and *Tierney, C.*, 1998: Altimeter sampling characteristics using a single satellite. *Journal of Geophysical Research*, **103**(C5):10513–10526.

Parke, M. E., Stewart, R. H., Farless, D. L. and *Cartwright, D. E.*, 1987: On the choice of orbits for an altimetric satellite to study ocean circulation and tides. *Journal of Geophysical Research*, **92**(C11):11693–11707.

Pond, S. and *Pickard, G. L.*, 1983: *Introductory dynamical oceanography*. Butterworth–Heinemann Limited, Oxford, U.K., second ed. edn.

Ponte, R. M., Salstein, D. A. and *Rosen, R. D.*, 1991: Sea level response to pressure forcing via barotropic numerical model. *J. Phys. Ocean.*, **21**:1043–1057.

Rapp, R., 1994: Global geoid determination. In *Geoid and its geophysical interpretations*, edited by P. Vaníček and N. T. Christou, CRC Press, Boca Raton, Florida, chap. 3, pp. 57–76. First edn.

Rapp, R., Wang, Y. M. and *Pavlis, N. K.*, 1991: *The Ohio State 1991 geopotential and sea surface topography harmonic coefficient models*. Report 410, Ohio State Univ., Dept. of Geod. Sci. and Surv., Columbus, USA.

Rapp, R. H., 1991: The Earth's Gravity Field from Satellite. In *The Solid–Earth Mission ARISTOTLES, SP–329*, edited by C. Mattok. pp. 29–32.

Rapp, R. H., 1993: Global undulation accuracy. *IEEE Trans. Geosci. Remote Sens.*, **31**(2):365–370.

Rapp, R. H., 1997: Mean sea surface used for the GEOSAT JGM-3 GDRs. GEOSAT online Handbook at 'http://www.nodc.noaa.gov/NODC-cdrom'.

Rapp, R. H. and *Nerem, R. S.*, 1995: Geoid undulation and mean sea surface recommendations. Paper presented at the TOPEX/Poseidon Science Working Team Meeting, Jet Propulsion Laboratory.

Rapp, R. H. and *Pavlis, N. K.*, 1990: The development and analysis of geopotential coefficient models to spherical harmonic degree 360. *Journal of Geophysical Research*, **95**:21885–21911.

Rush, C. M., 1986: Ionospheric radio propagation models and predictions - A mini review. *IEEE Trans. Antennas and Prop.*, **AP-34**(9):1163–1170.

Sandwell, D. T., 1984: A detailed view of the south Pacific geoid from satellite altimetry. *Journal of Geophysical Research*, **89**(B2):1089–1104.

Sandwell, D. T., 1992: Antarctic marine gravity field from high-density satellite altimetry. *Geophys. J. Int.*, **109**:437–448.

Sandwell, D. T. and *McAdoo, D. C.*, 1990: High-accuracy, high resolution gravity profiles from 2 years of Geosat exact repeat mission. *Journal of Geophysical Research*, **95**:3049–3060.

Schreiner, W. S., Markin, R. E. and *Born, G. H.*, 1997: Correction of single frequency altimeter measurements for ionosphere delay. *IEEE Trans. Geosci. Remote Sens.*, **35**(2):271–277.

Schwarz, K. P., Sideris, M. P. and *Forsberg, R.*, 1990: The use of FFT techniques in physical geodesy. *Geophys. J. Int.*, **100**:485–514.

Sideris, M. G. and *Tziavos, I. N.*, 1988: FFT evaluation and applications of gravity–field convolution integrals with mean and point data. *Bulletin Géodesique*, **62**:521–540.

Singleton, R. C., 1967: A method for computing the fast Fourier transform with auxiliary memory and limited high speed storage. *IEEE. Trans. on Audio and Electro.*, **AU–15**(2).

Skolnik, I. M., 1990: *The Radar Handbook*. McGraw-Hill Book Company, New York, second edn.

Small, C. and *Sandwell, D. T.*, 1992: A comparison of satellite and shipboard gravity measurements in the gulf of Mexico. *Geophysics*, **57**(7):885–893.

Stokes, G. G., 1849: On the variation of gravity on the surface of the Earth. *Trans. Cambridge Philosp. Soc.*, **8**:672–695.

Tai, C. K., 1988: Geosat crossover analysis in the tropical Pacfic, 1. Constrained sinusoidal crossover adjustment. *Journal of Geophysical Research*, **93**(10):10621–10629.

Tapley, B. D., Watkins, M. M., Ries, J. C., Davis, G. W., Eanes, R. J., Poole, S. R., Rim, H. J., Schutz, B. E., Shum, C. K., Nerem, R. S., Lerch, F. J., Marshall, J. A., Klosko, S. M., Pavlis, N. K., and *Williamson, R. G.*, 1996: The Joint Gravity Model 3. *Journal of Geophysical Research*, **101**(B12):28029–28049.

Todhunter, I. and *Leathem, J. G.*, 1901: *Spherical Trigonometry*. MacMillan and Company Limited, London, first edn.

Tokmakian, R. T., Challenor, P. G., Guymer, T. H. and *Srokosz, M. A.*, 1994: The U.K. EODC ERS-1 altimeter oceans processing scheme. *Int J. Remote Sensing*, **15**(4):939–962.

Vass, P. and *Battrick, B.*, 1992: *The ERS-1 system*. Report SP-1146, ESA, ESTEC, Noordwijk, The Netherlands.

Vassiliou, A. A. and *Schwarz, K. P.*, 1987: Study of the high–frequency spectrum of the anomalous gravity potential. *Journal of Geophysical Research*, **92**(B1):609–617.

Wahr, J. W., 1985: Deformation of the Earth induced by polar motion. *Journal of Geophysical Research*, **90**:9363–9368.

Wessel, P. and *Smith, W. H. F.*, 1991: Free software helps map and display data. *EOS Trans. AGU*, **72**(441):445–446.

Wessel, P. and *Smith, W. H. F.*, 1996: New version of the Generic Mapping Tools released. *EOS Trans. AGU*, **76**(329).

Williamson, R. G. and *Nerem, R. S.*, 1994: Improved orbit computations for the GEOSAT mission benefits for oceanographic and geodynamic studies. *EOS Trans.*, **75**(44).

Wunsch, C., 1972: Bermuda sea level in relation to tides, weather, and baroclinic fluctuations. *Rev. Geophys.*, **10**:1–49.

Wunsch, C. and *Stammer, D.*, 1995: The global frequency–wavenumber spectrum of oceanic variability estimated from TOPEX/Poseidon altimetric measurements. *Journal of Geophysical Research*, **100**(C12):24895–24910.

Wunsch, C. and *Zlotnicki, V.*, 1984: The accuracy of altimetric surfaces. *Geophys. J. Royal Astron. Soc.*, **78**:795–808.

Yi, Y., 1995: *Determination of gridded mean sea surface from TOPEX, ERS-1 and GEOSAT altimetry data*. Report 434, Ohio State Univ., Dept. of Geod. Sci. and Surv., Columbus, USA.

Zlotnicki, V., 1994: The geoid From satellite altimetry. In *Geoid and its geophysical interpretations*, edited by P. Vaníček and N. T. Christou, CRC Press, Boca Raton, Florida, chap. 5, pp. 95–110. First edn.